Porosity-Permeability Analysis on Pore Scale Simulation of Colloid Attachment

Master's Thesis

Name: Rens Marnette

Student Number: 4092589

Supervisor: Amir Raoof

Co-Supervisor: Ruud Schotting, Mandana Samari, Saeed Jafari

Keywords: Lattice Boltzmann Method, colloids, constricted pore, DLVO, porosity-permeability, Kozeny-Carman, attachment

Abstract

The results from a developed model in Utrecht University are used to investigate the effect of particle attachment on pore hydraulic conductivity. The model was developed to simulate particle attachment on a micro-scale to the pore surface of a constricted pore. Fluid mechanics were modeled using the lattice Boltzmann method of fluid simulations, and particles were simulated as smooth body forces acting as an external force within the Lattice Boltzmann equation using the smoothed profile method. DLVO forces were simulated between particles, and between particles and the pore surface. A sensitivity analysis has been performed regarding four different variables influential to DLVO and hydrodynamic interactions that govern particle attachment. The variables analyzed include: particle radius, zeta potential, ionic strength and flow velocity.

The resulting data of the model has been applied to investigate potential porosity-permeability relations at the micro-scale using attached particles as a proxy for porosity. The resulting profiles have been fitted using a generalized Kozeny-Carman and power law relation. Furthermore, coefficient analysis of said equations has been performed to investigate trends between changes in variables and coefficients. Although the fitted equations provide an adequate fit to the modeled system, further research are recommended to provide conclusive results on the coefficient analysis.

Contents

Introduction

Motivation

Colloid transport and deposition has been a widely researched subject, because it is important in many industrial and environmental applications, ranging from waste water filtration to paints and coatings [1,2,3]. For applications like waste water filtration, high particle retention is preferred. For other applications particle deposition may be undesirable [4].

The way colloids are deposited to solid surfaces is determined through the interaction between hydrodynamic and colloidal interaction forces [5]. The colloidal interaction forces are described by what is known as DLVO theory. Hydrodynamic forces are often modeled through the use of the Navier-Stokes equations.

The practical use of colloid transport and retention are most often on a field scale. However, the interactions that allow attachment and detachment on solid surfaces to occur in porous media are active at much smaller scales. That is why it is vital to have a thorough understanding in the processes that happen on a micro scale, which in turn might be translated to effects on a much larger scale.

The model presented in this study may be used for various different kinds of results that arise from particle attachment in pore spaces. For example the rate of coagulations, or changes in surface coverage. This study will focus on porosity-permeability relations. Permeability is one of the main variables describing fluid flow in groundwater applications, and is highly sensitive to changes in scale [6].

The main question in this study is, if on such a small scale, porosity may be used to predict permeability through the use of known relations, similar to the way this can be done on larger scales. Other questions will include if there is any correlation in the changes in porosity-permeability profiles and changes in model variables.

Overview

In this study a model will be presented that simulates particle attachment on a single pore scale. The method of fluid simulation is the Lattice Boltzmann Method. This way of modeling groundwater flow is based on the probability of particle populations streaming to equilibrium conditions, and will be covered in the first Section of this work.

Section 2 will go over the way particles are simulated within the model. Particle simulation is done through the Smooth Profile Method, which overlays a ,density field over an existing fluid flow field. This in combination with the Lattice Boltzmann Method allows for particles to experience the hydrodynamic force of the fluid, but the fluid will be also be affected by the particles suspended in it.

DLVO theory and how it describes the colloid and surface interactions is laid out in Section 3. It describes the theory and how this has been implemented in the model presented in this study.

The focus in this study is on porosity-permeability relations, which is why Section 4 gives a description of porosity-permeability in groundwater and porous media, as well some information about relevant relations.

The next section will give a description on how the previously presented equations and interactions are assimilated into the model. Furthermore, optimization through parallel computing is discussed, and all the conditions required for the model setup are given.

The last few sections will include the results, a discussion of set results, and a concluding summary of the study.

The Lattice Boltzmann Method

The model presented in this study is based on a way of simulating fluid flow called the Lattice Boltzmann Method (LBM). This part will go into more detail on the origins of this method and how it can be used to simulate fluid mechanics, as well as the different boundary conditions necessary to simulate proper flow with the LBM.

Kinetic Theory and the Boltzmann Equation

The science on which the LBM is based is called kinetic theory. Originally kinetic theory was designed to simulate fluids (mostly dilute gasses) at a mesoscopic scale. This mesoscopic scale being the scale between microscopic and macroscopic. Where macroscopic corresponds to a scale in which the fluid is considered a continuum, as is the case with the traditional Navier-Stokes Equations (NSE). And where the microscopic scale is considered the scale of tracking individual particles or molecules [7 p.12].

On this mesoscopic scale, not the individual particles are followed, but the distribution of a large number of particles. It is based on the idea that gas molecules constantly collide with each other. At any point in time the collective collisions of molecules or particles will determine an average direction and velocity that the collective particles will travel in.

This is one of the key concepts of kinetic theory and is represented by the distribution function $f(\boldsymbol{x}, \boldsymbol{\xi}, t)$. It represents the density of particles as well as their velocity components at a given time t and point $\boldsymbol{x}$. It has the units of $\frac{kg\, s^3}{m^6}$ as it represents a certain mass of particles (kg) in space ($\frac{1}{m^3}$), given their velocities ($\frac{1}{(ms^{-1})^3}$) [7 p.16].Given enough time, a gas will revert back to a uniform distribution, which in terms of the distribution function is denoted as equilibrium distribution $f^{eq}(\boldsymbol{x}, \boldsymbol{\xi}, t)$.

To use the distribution function its evolution in time has to be evaluated. Because the distribution function is dependent on $\boldsymbol{x}, \boldsymbol{\xi}$ and t, the total rate of change is determined by:

$$\frac{df}{dt} = \left(\frac{\partial f}{\partial t}\right)\frac{dt}{dt} + \left(\frac{\partial f}{\partial \boldsymbol{x}}\right)\frac{d\boldsymbol{x}}{dt} + \left(\frac{\partial f}{\partial \boldsymbol{\xi}}\right)\frac{d\boldsymbol{\xi}}{dt} \qquad 1$$

This can be simplified to:

$$\frac{df}{dt} = \frac{\partial f}{\partial t} + \boldsymbol{\xi}\frac{\partial f}{\partial \boldsymbol{x}} + \frac{\boldsymbol{F}}{\rho}\frac{\partial f}{\partial \boldsymbol{\xi}} \qquad 2$$

As $\frac{dt}{dt} = 1$, $\frac{d\boldsymbol{x}}{dt} = \boldsymbol{\xi}$ and $\frac{d\boldsymbol{\xi}}{dt} = \frac{\boldsymbol{F}}{\rho}$. The last being body force coming from Newton's second law, which has the units $\frac{N}{\rho}$ [7 p.21]. The total rate of change between a given time interval is called the collision operator [7 p.21, 8 p15]. This brings the distribution function to:

$$\frac{\partial f}{\partial t} + \boldsymbol{\xi}\frac{\partial f}{\partial \boldsymbol{x}} + \frac{\boldsymbol{F}}{\rho}\frac{\partial f}{\partial \boldsymbol{\xi}} = \Omega(f) \qquad 3$$

Where $\Omega(f)$ is the collision operator, which will have to be some function dependent on f. The first two terms can be seen as an advection term, which determines the direction and velocity of the particles, and the second term is represent forces that act on this velocity. The collision operator represents a source term. This source term embodies the local redistribution of f because of collisions [7 p.21]. The equation as given in equation 3 is called the Boltzmann Equation.

The next step in kinetic theory is to find the collision operator and solve equation 3. The original collision operator solved by Boltzmann himself is a complicated double integral that solves for all possible outcomes of all possible forces acting on two colliding particles. However, when using the LBM an approximation is used as a collision operator.

This approximation is called the BGK collision operator, and takes the form of:

$$\Omega(f) = -\frac{1}{\tau}(f - f^{eq}) \qquad 4$$

In this collision operator the distribution function is relaxed to its equilibrium state trough the relaxation time τ, which determines the speed of the relaxation to equilibrium.

The Lattice Boltzmann Equation

To implement equation 3 numerically it has to be discretized, which is done in the following way. Consider the Boltzmann equation without external forces, with the BGK collision operator:

$$\frac{\partial f}{\partial t} + \boldsymbol{\xi} \cdot \nabla f = -\frac{1}{\tau}(f - f^{eq}) \quad 5$$

This is the equation that needs to be solved in order to simulate fluid flow. The equation is discretized in a way that particle population can only flow in certain directions, which gives the following discretized equation:

$$f_i(\boldsymbol{x} + \boldsymbol{c_i}\Delta t, t + \Delta t) = f_i(\boldsymbol{x}, t) + \frac{\Delta t}{\tau}\left(f_i^{eq} - f_i\right) \quad 6$$

Here $\boldsymbol{x}$ are points on a chosen square lattice, $\boldsymbol{c_i}$ are discrete velocities, with specific directions depending on the chosen lattice grid, and f_i is defined only on the points of $\boldsymbol{x}$ and between time steps Δt.

The unknown in this equation is the computation of the equilibrium distribution f_i^{eq}. This is given by:

$$f_i^{eq}(\boldsymbol{x}, t) = \omega_i \rho \left(1 + \frac{\boldsymbol{u} \cdot \boldsymbol{c_i}}{c_s^2} + \frac{(\boldsymbol{u} \cdot \boldsymbol{c_i})^2}{2c_s^4} - \frac{\boldsymbol{u} \cdot \boldsymbol{u}}{2c_s^2}\right) \quad 7$$

Here ω_i is a collection of weights associated with the different velocity directions. The weight associated with each direction depends on the lattice grid that is chosen, which will be discussed soon. ρ is the density of the fluid at the lattice, $\boldsymbol{u}$ is the fluid velocity at the node, where $\boldsymbol{u} = \begin{pmatrix} u \\ v \end{pmatrix}$ for 2-dimensional flow, and c_s is the speed of sound which is related to c through $c_s^2 = \frac{c^2}{3}$. From equation 6, it is possible to obtain the Navier-Stokes equation for incompressible flow by using the Chapman-Enskog expansion. From this derivation follows that the shear viscosity ν is related to the relaxation time τ and the speed of sound c_s through $\nu = c_s^2\left(\tau - \frac{\Delta t}{0.5}\right)$ [7 p.65, 9]. Equation 7 is selected in such a way that this derivation to the Navier-Stokes equation is possible.

It is necessary to determine the lattice spacing and the time step. The most commonly used unit for this is the lattice unit, an artificial unit such that $\Delta x = 1$ and $\Delta t = 1$. The streaming speed c is determined through $c = \frac{\Delta x}{\Delta t}$. Because the lattice units are 1, the streaming speed will be 1

as well, which in turn implies that $c_s^2 = \frac{1}{3}$ [9]. An in-depth look and discussion on the derivation of the Navier-Stokes equation from equation 6 can be found at [10, 11].

To be able to solve the equations, a square lattice grid with a set of velocity directions must be chosen. The discrete velocity directions $\boldsymbol{c_i}$ combined with the associated weights ω_i are called velocity sets. There are several different velocity sets available to solve equations 6 and 7, but the one this study uses is called the $D2Q9$. Where the D represents the spatial dimensions and Q the number of velocities. In this case there are 9 different velocities. The directions are exemplified in Figure 1, where:

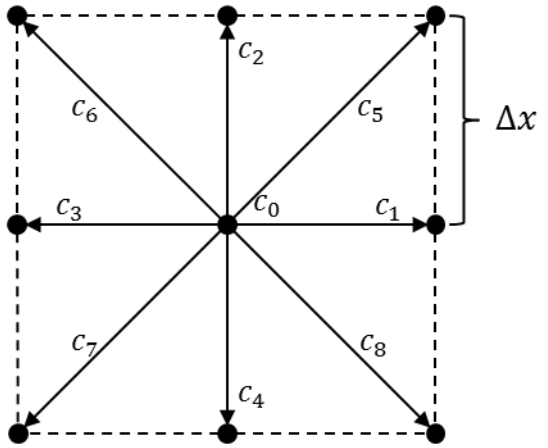

$$c_i = \begin{cases} (0,0) & i = 0 \\ (1,0),(0,1),(-1,0),(0,-1) & i = 1,2,3,4 \\ (1,1),(-1,1),(-1,-1),(1,-1) & i = 5,6,7,8 \end{cases}$$

$$\omega_i = \begin{cases} 4/9 & i = 0 \\ 1/9 & i = 1,2,3,4 \\ 1/36 & i = 5,6,7,8 \end{cases}$$

Figure 1. The direction from which particles can stream from node to node for the D2Q9 model.

To determine the equilibrium distribution f_i^{eq}, macroscopic variables like density ρ and velocity field $\boldsymbol{u}$ are required. Using the D2Q9 model, macroscopic variables can be obtained through weighted moments of f_i. Density and velocity are related in the following way to the distribution function [7 p.63]:

$$\rho(\boldsymbol{x},t) = \sum_{i=0}^{8} f_i(\boldsymbol{x},t) \qquad 8$$

$$\rho(\boldsymbol{x},t)\boldsymbol{u}(\boldsymbol{x},t) = \sum_{i=0}^{8} \boldsymbol{c_i} f_i(\boldsymbol{x},t) \qquad 9$$

Solving one time step is done in two main parts, known as the LBGK scheme: collision and streaming. The collision step calculates the distribution function after the particle populations

have collided, based on the relaxation time τ and the equilibrium distribution f_i^{eq}, which is determined through equation 7. First the macroscopic variables $\boldsymbol{u}$ and ρ are required to calculate the equilibrium distribution function f_i^{eq}. This can be done using the aforementioned equations 8 and 9, using the distribution function f_i. The collision function would be implemented as follows:

$$f_i^*(\boldsymbol{x}, t) = f_i(\boldsymbol{x}, t) + \frac{\Delta t}{\tau}\left(f_i^{eq} - f_i\right) \quad 10$$

Where $f_i^*(\boldsymbol{x}, t)$ is the distribution function after collisions [book 1 p.66 4].

Following collision is the streaming step, where particle populations move – or stream – to their neighboring cells according to their directions:

$$f_i(\boldsymbol{x} + \boldsymbol{c_i}\Delta t, t + \Delta t) = f_i^*(\boldsymbol{x}, t) \quad 11$$

Once the streaming process is completed, one full time step is finalized. Next the new macroscopic variables can be obtained and the process can be repeated [7 p.66 4].

Boundary Conditions

To setup a flow simulation boundary conditions are required. The LBM has its own set of boundary conditions that have to implemented a certain way, such that the distribution function at the boundary nodes properly represent the macroscopic fluid properties of that boundary condition.

There are many ways to simulate different boundary conditions with the LBM. This study however, utilizes four different boundary conditions: half way bounce-back boundary conditions, bounce-back boundary conditions for curved surfaces, constant pressure boundary condition, and a constant velocity boundary condition

When modelling a pore space, a no-slip boundary condition can be applied to the top and bottom walls of the pore. A no-slip boundary conditions states that adhesion forces of the fluid particles against the solid particles is larger than the cohesion forces of the fluid particles. This

force imbalance cause the fluid velocity to become practically zero at the fluid-solid interface [12].

To achieve a no-slip condition with the LBM, a bounce-back scheme can be used. The basis of a bounce-back scheme is that during the streaming process, when particle populations hit a rigid wall, they are reflected back to where they came from. This means that their average momentum will be zero (Figure 2). For this study a halfway bounce-back scheme is used. This implies that during the streaming process, the particle population is bounced back to its original starting point (Figure 3). From Figure 3 it becomes clear that the physical wall that separates the fluid nodes from the solid nodes, is located somewhere in the middle between the nodes [book 1 p.176 4].

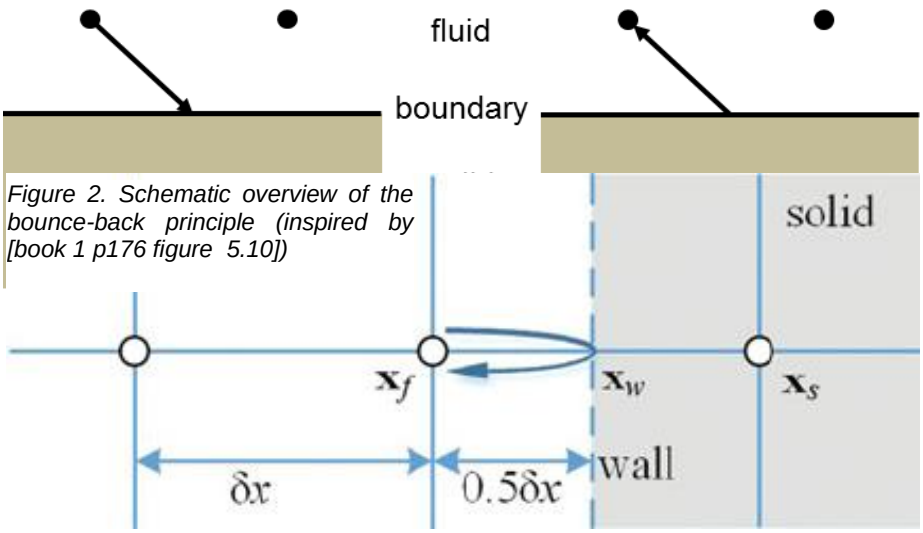

Figure 2. Schematic overview of the bounce-back principle (inspired by [book 1 p176 figure 5.10])

Figure 3. Schematic overview of the halfway bounce-back scheme.

Bounce-back boundary conditions are some of the easiest boundary conditions to implement within the LBM. To implement the halfway bounce-back scheme, the standard streaming step for the fluid nodes is replaced with a different function specifically for all boundary nodes:

$$f_i(\boldsymbol{x}, t + \Delta t) = f_i^*(\boldsymbol{x}, t) \qquad 12$$

The streaming step for the fluid solid interface depicted in Figure 3, going from node x_f to x_s, would look like:

$$f_3(x_f, t+\Delta t) = f_1^*(x_f, t)$$
$$f_7(x_f, t+\Delta t) = f_5^*(x_f, t) \quad 13$$
$$f_6(x_f, t+\Delta t) = f_8^*(x_f, t)$$

Curved boundary conditions are necessary when the geometry of the model domain is more complex. The bounce-back scheme proposed previously works well in geometries where the boundary wall is consistently halfway between the fluid and solid nodes. In the case of curved geometries, the physical boundary will not always lie halfway Figure 4.

A solution to this problem is a special bounce-back scheme as proposed by [13]. The first step is to determine the location of the wall between the fluid and the solid node through:

$$q = \frac{|AC|}{|AB|} \quad 14$$

Where q is the location of the wall between the fluid and solid node, and $|AC|$ and $|AB|$ are the distance between the fluid node and the wall, and the fluid node and the solid node respectively. Then, depending on the value of q, with linear interpolation, the values of the off-grid distributions functions are determined, and pushed back to the nearest fluid node:

$$f_{-i}(\boldsymbol{x_f}, t+\Delta t) = 2q f_i^*(\boldsymbol{x_f}, t) + (1-2q) f_i^*(\boldsymbol{x_f} - \boldsymbol{c_i}, t), \qquad q < \frac{1}{2} \quad 15$$

$$f_{-i}(\boldsymbol{x_f}, t+\Delta t) = \frac{1}{2q} f_i^*(\boldsymbol{x_f}, t) + \frac{2q-1}{2q} f_{-i}(\boldsymbol{x_f}, t), \qquad q \geq \frac{1}{2} \quad 16$$

Where f_{-i} means the distribution function at the reversed velocity of i. The values of f_i^* on the right hand side of equations 15 and 16 are taken after collision and before streaming. The values on the left hand side will be used after streaming. Relating Figure 4 to equations 15 and 16, $\boldsymbol{x_f}$ becomes the fluid node A and $\boldsymbol{x_f} - \boldsymbol{c_i}$ becomes the fluid node E.

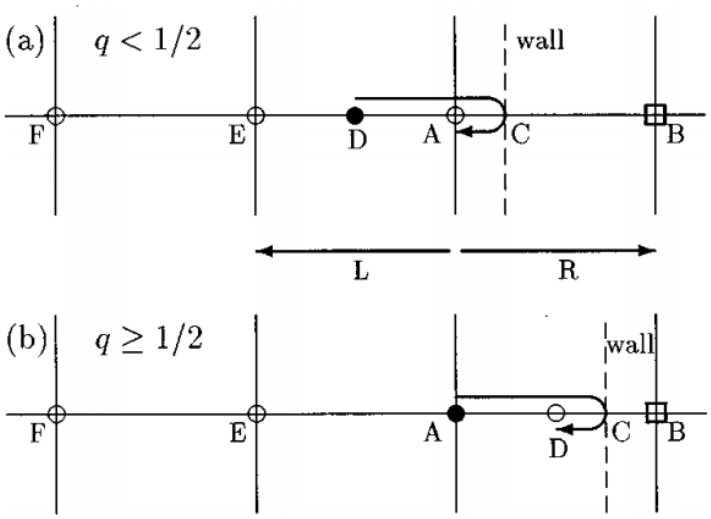

Figure 4. Schematic overview of bounce-back of curved surfaces (from [Boudhazie])

Moving on from wall boundary conditions to inlet/outlet boundary conditions. The first detailed here is the constant velocity boundary condition. To set up a constant velocity boundary condition, a method called the non-equilibrium bounce-back is used [7 p.196, 14] Using this method, given the velocity at the boundary nodes (the inlet boundary nodes in this example), the density ρ can be extrapolated using the known distribution functions:

$$\rho = \frac{1}{1-u_{in}}(f_0 + f_2 + f_4 + 2(f_3 + f_6 + f_7)) \quad 17$$

And the missing distribution functions are determined through:

$$f_1 = f_3 + \frac{2}{3}\rho u_{in} \quad 18$$

$$f_5 = f_7 - \frac{1}{2}(f_2 - f_4) + \frac{1}{6}\rho u_{in} + \frac{1}{2}\rho v_{in} \quad 19$$

$$f_8 = f_6 + \frac{1}{2}(f_2 - f_4) + \frac{1}{6}\rho u_{in} - \frac{1}{2}\rho v_{in} \quad 20$$

With this method, the incoming velocities can be specified and used to extrapolate the corresponding incoming distribution functions [8 p.77, 14].

The same way density can be extrapolated from velocity, so can velocity be extrapolated from density. To apply a constant pressure (density) boundary conditions, the following equations can be used for nodes at the outlet boundary:

$$u = -1 + \frac{f_o + f_2 + f_4 + 2(f_1 + f_5 + f_8)}{\rho_{out}} \quad (21)$$

$$f_3 = f_1 - \frac{2}{3}\rho_{out}u \quad (22)$$

$$f_7 = f_5 + \frac{1}{2}(f_2 - f_4) - \frac{1}{6}\rho_{out}u \quad (23)$$

$$f_6 = f_8 - \frac{1}{2}(f_2 - f_4) - \frac{1}{6}\rho_{out}u \quad (24)$$

Particle Simulation

There are several ways to simulate particles with the LBM. The most direct way is to impose moving bounce-back boundary conditions on the simulated particles, which can be done in several different ways [15, 16]. The particle interface is then represented by the linked boundary nodes. However, using this method the particle will not move smoothly in space, as a square lattice inherently cannot simulate a circular particle correctly. This can be partly solved by locally increasing mesh resolution like done in [17]. For systems with more particles this method becomes more and more computationally heavy.

Smoothed-Profile Method

Another way of simulating particle populations is used in this study. This method is called the smoothed-profile method (SPM) it treats the particles as smooth body forces within the Navier-Stokes equation instead of imposing boundary conditions on each particles [9, 18]. This way a single set of fluid dynamic equations needs to be solved, and the forces acting on the fluid and the fluid on the particles is determined through a smoothed layer over the model domain which represents the boundaries between fluid motion an particle motion [9].

This smoothed profile is represented by the density field:

$$\phi(\boldsymbol{x}, t) = \sum_{i=1}^{N_p} \phi_i(\boldsymbol{x}, t) \qquad 25$$

Where $\phi_i(\boldsymbol{x}, t) \in [0,1]$ is the density profile of the ith particle up to N_p number of particles [9]. This implies that where there is only fluid, $\phi(\boldsymbol{x}, t) = 0$, and where there is a particle $\phi(\boldsymbol{x}, t) = 1$. Previously a sharp discontinuous interface between the fluid and the solid particle was used. In numerical sciences, discontinuous profiles often give rise to numerical inaccuracies. That is why the SPM proposes that between the fluid and particle density profile, there is a smooth continuous profile connecting the two (Figure 5).

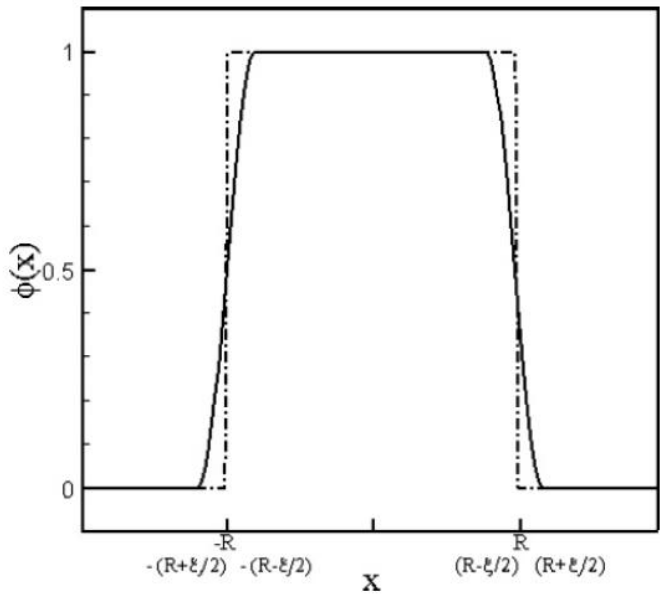

Figure 5. Overview of smoothed profile (solid line), from [saeed jafari & yamamoto].

The function by which the density profile $\phi(\boldsymbol{x}, t)$ transitions from 0 to 1 is arbitrary [19], but one way, used in this study, verified by [9], and exemplified in Figure 5 provides it the following way:

$$\phi_i(\boldsymbol{x}) = s(R - |\boldsymbol{x} - \boldsymbol{R_i}|),$$

$$s(\boldsymbol{x}) = \begin{cases} 0, & \boldsymbol{x} < -\xi/2 \\ \frac{1}{2}\sin\left(\frac{\pi \boldsymbol{x}}{\xi} + 1\right), & |\boldsymbol{x}| < \xi/2 \\ 1, & \boldsymbol{x} > \xi/2 \end{cases} \qquad 26$$

Using equation 26, the density profile of a particle $\phi_i(\boldsymbol{x})$ is determined by the distance between the particle center $\boldsymbol{R_i}$ and a given point $\boldsymbol{x}$ on the lattice grid, and the radius of the particle R. The profile then transitions over the region thickness ξ from 0 to 1 and back. Equation 26 is valid for 1 particle. The total density field of all particles is given by:

$$\phi(\boldsymbol{x}, t) = \sum_{i=1}^{N_p} s(R - |\boldsymbol{x} - \boldsymbol{R_i}|) \qquad 27$$

The velocity of the particles in the SPM is determined by the position $\boldsymbol{R_i}$, the translational velocity $\boldsymbol{V_i}$ and the angular velocity $\boldsymbol{\Omega_i}$ of the particles, where again i is the number of particles up to N_p. The velocity field is given by:

$$\phi(\boldsymbol{x},t)\boldsymbol{u}_P(\boldsymbol{x},t)=\sum_{i=1}^{N_p} s(R-|\boldsymbol{x}-\boldsymbol{R_i}|)\times\Big(\boldsymbol{V_i}(t)+\boldsymbol{\Omega_i}(t)\times\big(\boldsymbol{x}-\boldsymbol{R_i}(t)\big)\Big) \quad 28$$

The particle velocity field is required to determine the forces acting between the fluid and the solid interface. The force that the fluid acts on the solid particles $\boldsymbol{\phi f_p}$ is given by:

$$\int_t^{t+\Delta t}\phi(\boldsymbol{x},t)\boldsymbol{f_P}(\boldsymbol{x},t)ds=\phi(\boldsymbol{x},t)\big(\boldsymbol{u_P}(\boldsymbol{x},t)-\boldsymbol{u}(\boldsymbol{x},t)\big) \quad 29$$

Where $\boldsymbol{u}(\boldsymbol{x},t)$ and $\boldsymbol{u}_p(\boldsymbol{x},t)$ are the fluid velocity and particle velocity at point $\boldsymbol{x}$ and time t respectively. The force that the solid particles act on the fluid nodes is accordingly:

$$\boldsymbol{f_H}(\boldsymbol{x},t)=-\int_t^{t+\Delta t}\phi(\boldsymbol{x},t)\boldsymbol{f_P}(\boldsymbol{x},t)ds \quad 30$$

Recall the lattice Boltzmann equation for fluid flow simulation in the previous part of this study. The hydrodynamic force can be added as an additional force term in the collision function:

$$f_i^*(\boldsymbol{x},t)=f_i(\boldsymbol{x},t)+\frac{\Delta t}{\tau}\big(f_i^{eq}-f_i\big)+\left[\frac{\omega_\alpha \Delta t}{c_s^2}(\boldsymbol{f_H}(\boldsymbol{x},t)\cdot\boldsymbol{c_i})\right] \quad 31$$

This will update the flow field to include the effect that the particles have on the fluid flow. The next step is to update the particle positions. This is done by making use of the conservation of momentum law to find the force $\boldsymbol{F}_i^H$ and torque $\boldsymbol{N}_i^H$ applied by the fluid:

$$\int_t^{t+\Delta t}\boldsymbol{F}_i^H\,ds=\int_{\forall_P}\rho\phi_i(\boldsymbol{x},t)\big(\boldsymbol{u}(\boldsymbol{x},t)-\boldsymbol{u_P}(\boldsymbol{x},t)\big)\,d\forall_P \quad 32$$

$$\int_t^{t+\Delta t}\boldsymbol{N}_i^H\,ds=\int_{\forall_P}\big(\boldsymbol{x}-\boldsymbol{R_i}(t)\big)\times\rho\phi_i(\boldsymbol{x},t)\times\big(\boldsymbol{u}(\boldsymbol{x},t)-\boldsymbol{u_P}(\boldsymbol{x},t)\big)\,d\forall_P \quad 33$$

Where the particles are integrated over the volume integral $d\forall_P$. With updated force and torque the new translational and angular velocities of the particles can be determined through:

$$\boldsymbol{V}_i(t+\Delta t)=\boldsymbol{V}_i(t)+M_P^{-1}\int_t^{t+\Delta t}\big(\boldsymbol{F}_i^H+\boldsymbol{F}_i^{ext}\big)\,ds \quad 34$$

$$\boldsymbol{\Omega_i}(t+\Delta t)=\boldsymbol{\Omega_i}(t)+\boldsymbol{I}_P^{-1}\int_t^{t+\Delta t}\big(\boldsymbol{N}_i^H+\boldsymbol{N}_i^{ext}\big)\,ds \quad 35$$

Where $\boldsymbol{F}_i^H$ is the hydrodynamic force on the ith particle, and $\boldsymbol{F}_i^{ext}$ and $\boldsymbol{N}_i^{ext}$ are the external force and torque on the ith particle respectively. Here M_P and $\boldsymbol{I}_P$ are the mass of the particle

and the moment of inertia of the particle respectively. The position of the particle is updated through the translational velocity of the particle through:

$$\boldsymbol{R}_i(t+\Delta t) = \boldsymbol{R}_i(t) + \int_t^{t+\Delta t} \boldsymbol{V}_i \, ds \qquad 36$$

The new density field can now be calculated by means of the updated positions, translational and angular velocities.

Buoyance forces are considered when particles have a different density than the fluid. This force term can be added as an external force term in equation 34. The buoyancy force or gravity force can be implemented using the following equation:

$$\boldsymbol{F}_i^G = \rho_i V_i g \left(1 - \frac{\rho}{\rho_i}\right) \qquad 37$$

Where ρ_i and V_i are the particle density and volume respectively, and ρ is the fluid density.

DLVO Theory

The main aim of this study is to determine the effect of DLVO forces on the deposition of particles, and in particular the influence of different DLVO variables on deposition rates. This chapter will cover DLVO theory and the equations used in the model.

DLVO theory is the mathematical description of the attractive and/or repulsive forces particles experiences when interacting with other particles or surfaces in a liquid medium. DLVO stands for Derjaguin-Landau-Verwey-Overbeek, the names of the scientists that pioneered this theory. It combines two different forces governing the attraction or repulsion of particles:

$$\phi_{DLVO}(h) = \phi_{EDL}(h) + \phi_{VDW}(h) \quad 38$$

Where $\phi_{EDL}(h)$ is the electric double layer energy, $\phi_{VDW}(h)$ is the Van der Waals energy, and h is the separation distance. The separation distance defines the distance between the two interacting entities. However, to simulate the DLVO interactions in the model, not the energy but the force is necessary. The DLVO force can simply be computed by taking the derivative of equation 38 with respect to the separation distance h [20]:

$$\boldsymbol{F}_{DLVO}(h) = -\frac{d\phi_{DLVO}}{dh} \quad 39$$

Electric Double Layer

The electric double layer is key in the concept of charged solid surfaces in liquids. Water is the most important liquid for the electric double layer, because of its high dielectric constant, and its prevalence in environmental problems. Charged surfaces suspended in water create an electric field, which in turn attracts counter ions dissolved in the medium. This layer, which combines the surface charge and the counter ions, is called the electric double layer (EDL) [21].

Several different EDL models have been proposed. The Helmholtz model proposed that the counter ions would directly bind to the surface charge. This means that the double layer would only be one molecule thick. This managed to capture some of the observed features of charged surfaces in suspension, but failed to capture the easily measurable capacitance of the EDL.

The next model describes the layer of counter ions as a diffuse layer, which takes into account the movement of ions in the medium. This is how the EDL is usually described and works for most common applications, and is called the Gouy-Chapman model [21]. A schematic overview of the two models is given in Figure 6.

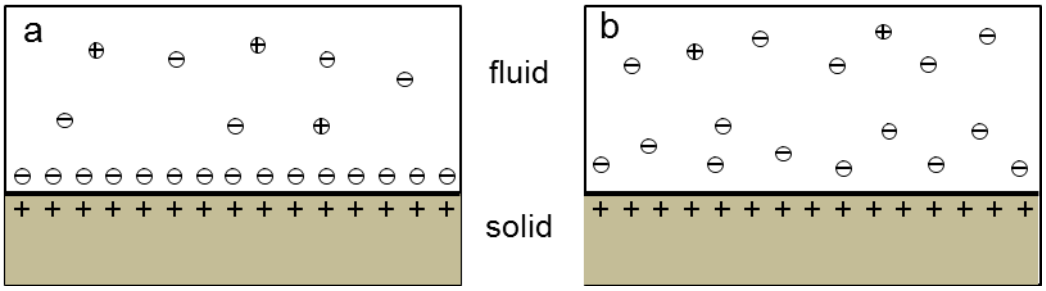

Figure 6. a) Schematic representation of Helmholtz EDL model. b) Schematic overview of Gouy-Chapman EDL model.

The models in Figure 6 are based on the EDL of a flat surface[reference in book]. In the model of this study, particle simulation is of key importance, which are considered spherical. As the particles will have a charge of their own, they will also have a ELD when suspended in water. Debye and Hückel calculated the ELD properties for spherical surfaces .

In this study two different ϕ_{EDL} need to be computed. One for particle-particle interaction (ϕ_{P-P}^{EDL}) , and one for particle-wall (ϕ_{P-W}^{EDL}) interaction, given by [20, 22]:

$$\Phi_{EDL}^{P-W} = 2\pi\epsilon_o\epsilon_r R\zeta_W\zeta_P\left(\ln\left[\frac{1+e^{-\kappa h}}{1-e^{-\kappa h}}\right]+\frac{\zeta_W^2+\zeta_P^2}{2\zeta_W\zeta_P}\cdot\ln[1-e^{-2\kappa h}]\right) \quad 40$$

And

$$\Phi_{EDL}^{P-P} = 64\pi\epsilon_0\epsilon_r R_{eff}\left(\frac{K_BT}{Ze}\right)^2\cdot\tanh\left(\frac{Ze\zeta_i}{4KT}\right)\cdot\tanh\left(\frac{Ze\zeta_j}{4KT}\right)\cdot e^{-\kappa h} \quad 41$$

The equivalent forces for the respective interaction energies are obtained using equation 39 and look like:

$$\boldsymbol{F}_{P-W}^{EDL} = 4\pi\epsilon_0\epsilon_r\kappa R\zeta_W\zeta_P\left(\frac{e^{-\kappa h}}{1-e^{-2\kappa h}}-\frac{(\zeta_W+\zeta_P)^2}{2\zeta_W\zeta_P}\cdot\frac{e^{-2\kappa h}}{1-e^{-2\kappa h}}\right) \quad 42$$

And

$$\mathbf{F}_{P-P}^{EDL} = -64\pi\epsilon_0\epsilon_r\kappa R_{eff}\left(\frac{K_BT}{Ze}\right)^2\cdot\tanh\left(\frac{Ze\zeta_i}{4KT}\right)\cdot\tanh\left(\frac{Ze\zeta_j}{4KT}\right)\cdot e^{-\kappa h} \quad 43$$

Equations 40 and 41 give the interaction energy, and equations 42 and 43 give the force of the EDL particle-particle and particle-wall interactions respectively. Here ϵ_r and ϵ_0 are the relative permittivity and dielectric permittivity in a vacuum respectively, ζ_W and ζ_P are the zeta potential of the wall and particle respectively when considering particle-wall interaction, ζ_i and ζ_j are the zeta potentials of different particles when considering particle-particle interaction, R is the radius of the particle, R_{eff} is the effective radius between two particles i and j, given by: $\frac{R_i R_j}{R_i + R_j}$, Z is the valence of the particle, e is the charge of an electron, T is the absolute temperature, K_B is the Boltzmann constant, and κ is the inverse Debye length. The inverse of the Debye length κ is given by:

$$\kappa = \left(\frac{\epsilon_0 \epsilon_r K_B T}{2000 * e^2 N_A I}\right)^{-\left(\frac{1}{2}\right)} \quad 44$$

Here N_A is Avogadro's number and I is the ionic strength. These equations determine the influence the EDL will have on the particles.

Van der Waals Force

The other term used to determine the total interaction energy Φ_{DLVO} between a particle and a particle, or a particle and the surface, is called the Van der Waals energy Φ_{VDW}, or Van der Waals force $\boldsymbol{F}_{VDW}$. This is the usually attractive force between atoms or molecules because of the attraction of polar and non-polar parts of the atom or molecule in question.

The Van der Waals forces are explained by quantum mechanics. Quantum mechanics suggest that electrons in an atom are constantly moving. This implies that there is a probability that an excess of electrons is present in one part of the atom, or a shortage at another part . This creates a positive and negative pole on each side of the atom. When atoms get close enough to each other, these poles will attract each other [23]

For Van der Waals forces we once again consider two scenarios. The particle-particle interaction, and the particle-wall interaction. The Van der Waals force between two particles is determined through the following equation [24, 25]:

$$\boldsymbol{F}_{P-P}^{VdW} = \frac{32Ha}{3} \cdot D_{ij} \cdot \frac{R_i^3 R_j^3}{\left(\left(\left(D_{ij} + R_i\right)^2 - R_j^2\right)\left(\left(D_{ij} - R_i\right)^2 - R_j^2\right)\right)^2} \quad 45$$

Here Ha is the Hamaker constant, D_{ij} is the center to center distance between the two particles, and R_i and R_j are the radii of the two interacting particles. When the separation distance becomes much smaller than the radius of the particles, equation 45 can be simplified to [25]:

$$\boldsymbol{F}_{P-P}^{VdW} = \frac{HaR_{eff}}{6h^2} \quad 46$$

Van der Waal force interactions between particles and surfaces will start acting when a particle becomes significantly close enough to the surface, and is given similarly to equation 46 as:

$$\boldsymbol{F}_{P-W}^{VdW} = \frac{HaR_i}{6h^2} \quad 47$$

Where R_i is the radius of the particle interacting with the surface. The Hamaker constant is a constant which is dependent on the bulk properties of the two interacting entities, either the two particles or the particle and the wall, as well as the medium they are suspended in.

Due to the electrodynamic nature of Van der Waals forces, a magnetic retardation term has to be implemented [26]. This factor is a correction term on the total Van der Waals force, which implies that equations 45-47 obtain an additional factor given by:

$$f_m = \frac{\lambda(\lambda + 22.24h)}{(\lambda + 11.12h)^2} \quad 48$$

Where λ is the characteristic wavelength. This wavelength is usually taken to be 100nm.

The force equations are taken from the cited sources. The forces are calculated through equation 39 similarly to the EDL forces. The energy equations Φ_{P-P}^{VdW} and Φ_{P-W}^{VdW} are given by:

$$\Phi_{P-P}^{VdW} = \frac{HaR_{eff}}{6h} \quad 49$$

And

$$\Phi_{P-W}^{VdW} = \frac{HaR_i}{6h} \quad 50$$

The magnetic retardation factor can be implemented as:

$$f_m = \frac{1}{1 + \frac{11.12h}{\lambda}} \quad (51)$$

Interaction Energy Profiles

The DLVO energy interactions between particles and surfaces are key in determining if a particle is deposited on a surface, or if particles will stick together. To determine the effect of the DLVO energies on the potential deposition of particles, so called interaction energy profiles can be constructed. These energy interaction profiles plot the interaction energy against the separation distance.

There are several possible profile types, depending on the magnitude of attraction or repulsion by the EDL and Van der Waals forces. In the present study, the Van der Waals force is always attractive. The EDL force however, can be attractive or repulsive, depending on the zeta potentials of the particles and surface. The double layer force is attractive if the particles and surfaces are oppositely charged [27]. When a particle approaches a surface in this environment, there are only attractive DLVO forces present, which allow the particles to favorably deposit (Figure 7 a).

When a situation is presented where the EDL forces are repulsive, the regime of depositions becomes more complex. The interaction between attractive Van der Waals forces and repulsive EDL forces can produce different deposition regimes. The most common situation is one where there is a deep primary minimum and a high energy barrier. This implies that a particle that wants to attach or settle on a given surface, has to overcome a repulsive energy barrier through hydrodynamic or other forces to be able to fall into the attractive part of the DLVO regime. The reverse this is true if the particle wants to detach from the given surface.

Other scenarios include a secondary minimum. This occurs under certain physicochemical conditions. Particles may be retained at a small distance from the surface when they cannot overcome the energy barrier to reach the primary minimum, and will instead be retained at a secondary minimum, given that attractive energy of the minimum is large enough. Figure 7 b, c, and d give several scenarios with different combination of energy barriers and secondary minima.

The shape of the energy profile is determined through the interaction energy given in equation 38, which in turn depend on the definitions of the Van der Waals energy and EDL energy.

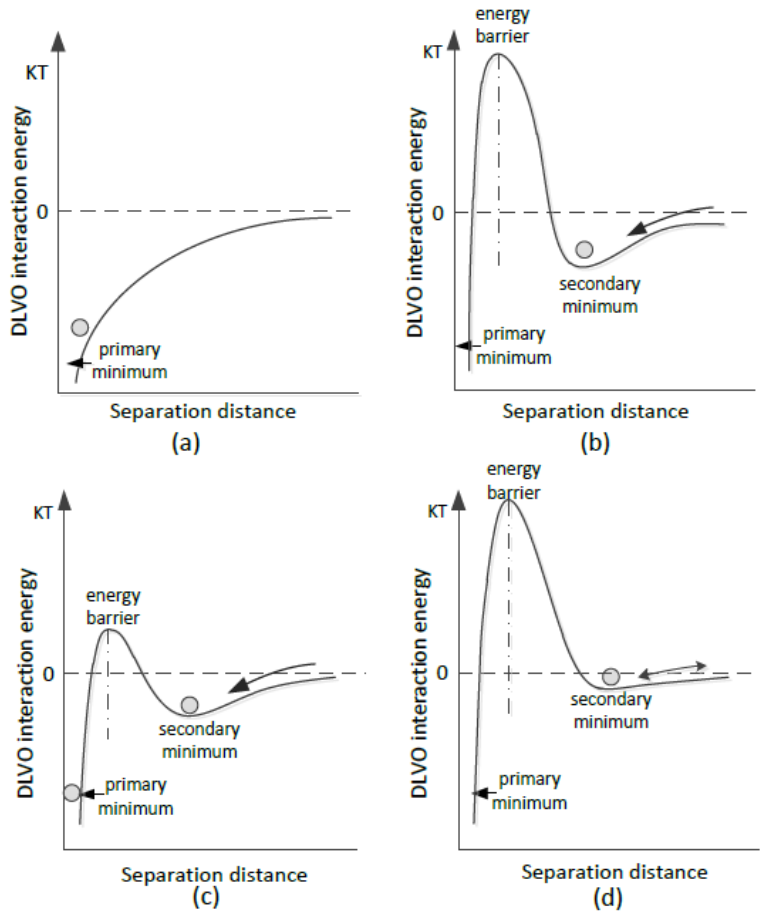

Figure 7. a) Attractive DLVO regime with only a primary minimum, b) DLVO regime with a secondary minimum and high energy barrier, c) DLVO regime with a deep secondary minimum and low energy barrier, d) DLVO regime with a low secondary minimum and high energy barrier. From: [27]

Porosity-Permeability Relation

The model presented in this study may be used to provide a wide spectrum of data usable for research. This study will focus in particular on the possibility of porosity-permeability relations which may arise in the system. This section will cover how porosity-permeability will be approached in this study.

Permeability is a parameter used when defining flows through porous media. It indicates the ability of a fluid to flow through a medium, or more specifically, the resistance a medium provides to a fluid flowing through it, as permeability is a property of the medium, not the fluid. It is used as a constant in Darcy's law in the following way:

$$\boldsymbol{u} = \frac{K}{\mu}\left(\frac{\Delta P}{L} - \rho \boldsymbol{g}\right) \tag{52}$$

Where K is the permeability, $\Delta P/L$ is the pressure gradient and $\boldsymbol{g}$ is the gravitational acceleration. Porosity is defined as the fraction of void space occupied by a fluid within a bulk volume. This can be shown most simply as:

$$\phi = \frac{void\ volume}{bulk\ volume} \tag{53}$$

Upscaling

Both permeability and porosity are variables that are inescapably linked to upscaling. When modeling groundwater flow, the interaction of the pore interface with the fluid on the smallest scale influences pore geometry or morphology, and influences fluid flow at a larger scale. To model larger scale groundwater flow however, all these processes cannot be modeled at their own scale, and simplifications have to be made to give averages over larger scales.

A difference in scale can be exemplified in Figure 8. Here the REV is defined as the representative elementary volume. The REV is the smallest volume where a property does not change when the dimensions are incremented gradually (bear 1988).

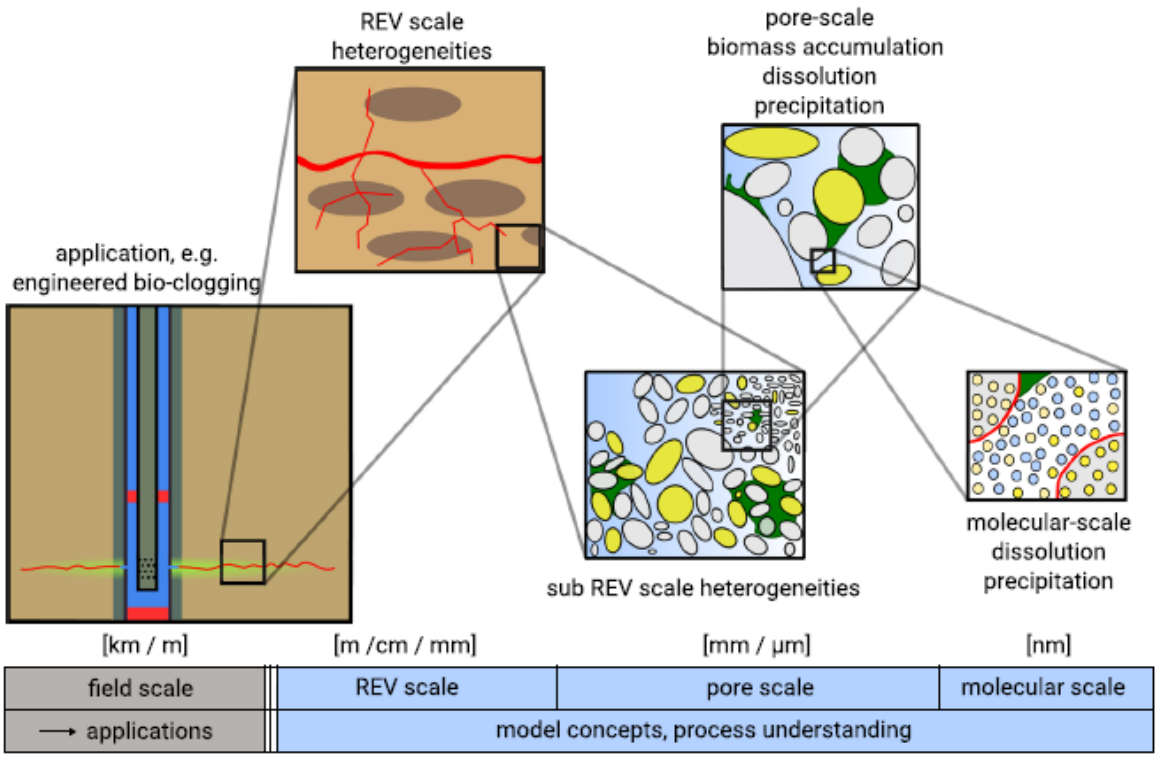

Figure 8. Different scales of porous media. From: [6].

From Figure 8 it becomes clear that porosity cannot always be accounted for the same way on different scales. On a large scales, average porosity is usually used, with heterogeneities in average porosity. On pore network scale, void fraction can clearly be estimated, however, it becomes clear that pore structure and morphology altering processes have a more profound effect on the pore network structure, which are not even visible on a larger scale. This is why these processes have to be estimated through upscaling.

Permeability as used in equation 52 can be obtained on larger scales, by upscaling the viscous effects of the Navier-Stokes equation on the pore scale [6]. Given permeability is a necessary variable for many practical applications, but not simple to obtain, many methods have been attempted to quantify or estimate permeability using more easily measured properties.

Kozeny-Carman

The original equation by Kozeny (1927) and modified by Carman (1937) describes a way to calculate pressure for a given flow velocity u and porous medium length L. This is given by:

$$\frac{\Delta P}{L} = \frac{180\mu}{\Phi_s^2 D_p^2} \frac{(1-\phi)^2}{\phi^3} u \qquad 54$$

Where Φ_s is the sphericity, D_p is the characteristic particle diameter and ϕ is the porosity. Using equation 52 this can be rewritten to provide an equation for permeability:

$$K_{KC} = \frac{\Phi_s^2 D_p^2}{180} \frac{\phi^3}{(1-\phi)^2} \qquad 55$$

This can also be rewritten to use more relevant parameters to naturally occurring porous media like:

$$K_{KC} = \frac{\phi^3}{\tau(1-\phi)^2 S^2} \qquad 56$$

Where τ is tortuosity and S is the specific surface area [28].

For the present study however, we are considering smaller than usual scale of one constricted pore. The porosity of the system is still defined as in equation 53, however, the bulk volume fraction is derived from the amount of particles that attach to the pore walls. To identify if there are permeability-porosity relations present in systems on this scale, a generalized version of the Kozeny-Carman equation is suggested, using the dimensionless permeability K/K_0:

$$\frac{K}{K_0} = a \frac{\phi^b}{(1-\phi)^c} \qquad 57$$

This general equation will first of all try to fit the porosity- permeability data obtained from the simulations, and secondly will try to identify if any of the coefficients relate to changes in specific parameters on this smaller scale.

Model Description

The equations governing the major processes of fluid flow and DLVO interactions have been discussed in the previous section. This section will go through how these equations are integrated into an all including model, as well as optimizing the model to increase efficiency by multithreading the model using the parallel computing tool OpenMP.

Subroutines

The model consists of 10 different subroutines which all encompass a different aspect of the model domain. This section will cover the different subroutines and how they implement the different equations outlined in the previous section of the study. The model consist of 10 subroutines, of which 8 are inside the main loop of the model Figure 9.

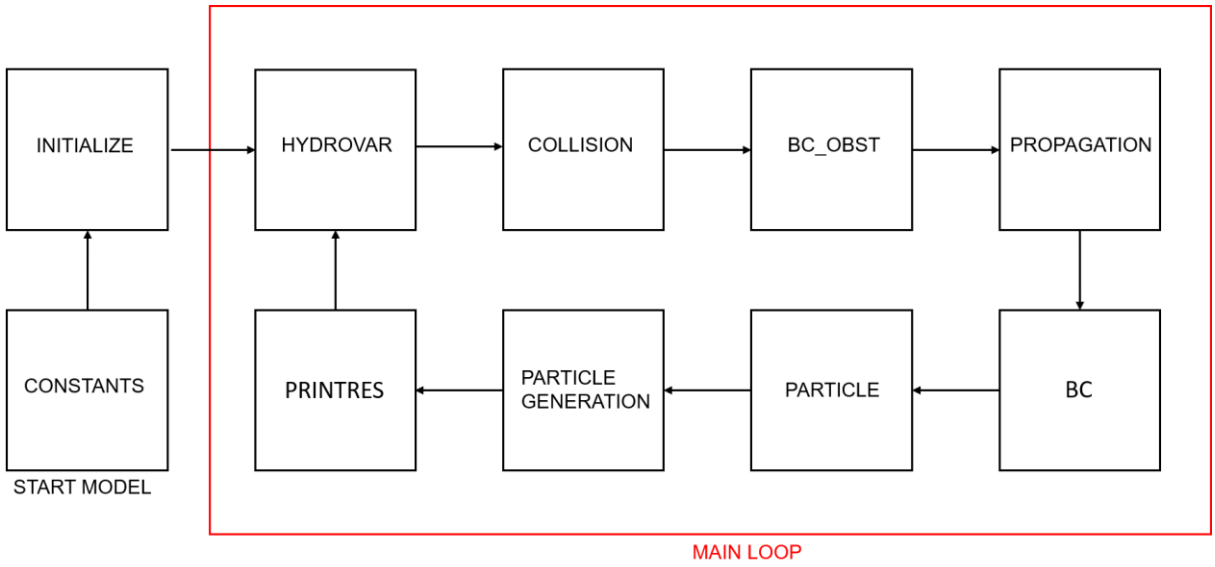

Figure 9. Model overview of different the different subroutines.

The first two subroutines are to initialize the model (Figure 9). A constants subroutine is used and linked to all other subroutines, and functions as a separate block of code of constants that are needed in other computations ranging from geometric constants to the Boltzmann constant. The second subroutine finalizes the initialization through the setup of a initial condition for the model. 3 different initial scenarios may be selected to suit the type of

simulation required. The first is a simulation from a zero velocity flow field, where the model will build a flow field according to the given geometry and particles present. The second needs existing data files for flow fields and particle properties such as particle positions , acceleration, velocity and torque, and uses these files to simulate an already set up situation. The last option is to only give data files of flow fields and particle positions. The model then applies the fluid velocity at the particles location to the particles.

Independent of whichever initialization scenario is selected, the model will continue into the main loop of the program. This loop will span the total time-steps of the model, and each loop covers one time-step.

As discussed in the first section of this study, the LBM has a particular order of operations, and this is translated into the subsequent subroutines. The first subroutine covers the computation of the macroscopic hydrodynamic variables, as well as the density field ϕ. This is then used to determine the total velocity field and body force. The variables computed are then used in the collision step of the LBM, which is its own separate subroutine. Here the collision term is calculated using the equation 7 and 10.

Before the streaming step is implemented, the boundary condition of the curved boundary has to be set up. The model reads a data file, created by a separate script that calculates equation 14 for all boundary nodes, to determine the appropriate bounce back scheme according to equations 15-16. After this the particles densities are streamed to their proper locations through the streaming process in the next subroutine.

After the streaming process is complete the model applies a further set of boundary conditions, which include a boundary condition for the inlet and outlet boundary; a combination of velocity and pressure boundary conditions at either the inlet and outlet boundary.

These 5 subroutines conclude the fluid dynamical component of the model. The next subroutine is the computationally heaviest and most intricate subroutine of the model. This subroutine governs the computations of particle interactions. It first calculates the hydrodynamic force and torque on particles according to equations 34 and 35. Then the DLVO forces are calculated between the particles and the bottom wall, particles and the top wall, and

particles and particles according to the appropriate DLVO equations for these interactions. At the end of the subroutine the particle positions are updated according to the forces acting on them.

The second to last subroutine consists of particle generation. The model can be allowed to generate particles on a timed basis, it can also ensure that there are always a set number of particles in the system, by generating a new particle if one particle is deposited, or it can generate a combination of both. To generate a particle the model checks if there is room for a particle to be generated at given initial locations. If there are obstacles, either curved boundaries or another particle, the model will try and find the next potential location.

The last subroutine is a print routine, which saves all the necessary data to data files. The flow fields u and v, density ρ, and density field ϕ are saved using proper format to be instantly read and processed using Paraview.

Parallel Computing

The previous section outlines the way the model is run for each time iteration. To improve the model, parallelization can be applied. Parallelizing is done to increase the speed of a sequential model on multicore processors, by instead of using only one thread which uses one core of the processor, different threads can be created that run the model simultaneously on multiple processor cores.

Depending on the amount of logical processor cores that is being used, the speed of the model can be significantly increased. Apart from the number of processing cores, the increase in efficiency depends on the percentage of parallelized code as well. Given a percentage of parallelized code, and the number of possible threads that can be generated, the theoretical increase in model efficiency can be determined through Amdahl's Law [29]:

$$I = \frac{1}{F + \frac{1 - F}{N}} \qquad 58$$

Where F is the fraction of code that remains serial, N is the number of threads that the processor can create, and I is the theoretical factor in increased speed.

Theoretical speed increase however is almost never accomplished for larger models or codes, because not every block of code can be parallelized. To efficiently parallelize a given code, parts of the code have to be found that can either be run independently from each other, or can be done simultaneously without affecting results of the other threads that run parallel to each other.

Intel Fortran for Visual Studios supports OpenMP 4.0 for FORTRAN, and provides several different work-sharing directives. These directives divide up a workspace into several chunks, which are then executed by different threads. The work-sharing directives used in the study's model are the *do* and *sections* directives. The *do* directive is the most often used directive. This directive specifies that the iterations of the next do loop are executed in parallel. The *sections* directive is used to assign one thread to specified blocks of code. The *sections* directive is used on blocks of code that can run independently from one another.

There are several synchronization directives available as well. These directives synchronize all threads to properly save variables and data so that none will be overwritten. Of importance in this study are the *barrier* and *critical* directives. The *barrier* directive synchronizes all threads, and is an implied directive after every work-sharing directive. The *critical* directive defines a region which can only be executed by one thread at a time. This directive helps to prevent race conditions and the overwriting of data and variables.

Within the work-sharing directives different clauses can be attached. The most important clauses are the designation of private and shared variables. By assigning variables as private, OpenMP creates a separate variable for the specific thread. This is essential when calculating different loop-specific variables. The shared clause indicates that these variables are to be used by all executing threads. These include constants and variables not changing within a given loop and *do* directive.

Another important clause is the schedule clause. This determines the way iterations within a *do* construct are executed. There are three different kind of schedules: static, dynamic, and guided. For a static schedule, each thread is assigned a chunk of iterations depending on the

chunk size, and when they are all executed, are assigned the next chunk of iterations. The dynamic schedule assigns a chunk of iterations to each thread, but when one thread completes a chunk of iterations, it requests the next chunk of iterations. The guided schedule starts off with large chunks, but decreases its chunk size when more chunks are being completed. Any of the schedules will work, but some will work more effectively with different kind of codes. For a code where iterations take approximately the same amount of work, static scheduling would work most efficiently. For codes where different iterations take different amounts of time, dynamic scheduling works better. Guided scheduling is a trade-off between the static and dynamic scheduling schemes. The way the model's *do* directives are setup up, allow for similar computation times over the shared workspaces. Therefore static scheduling has been applied to most of the *do* directives within the model.

The last important clause, exclusive to the *do* construct, is the collapse clause. This clause collapses two or more nested do loops into one large iteration space, which is then executed through the specified schedule clause.

The model uses the LBM to simulate fluid flow. The relative ease of parallelization with the LBM is one of the reasons it is becoming more popular [30]. The LBM calculates fluid flow at each node or grid point independently. This implies that macroscopic fluid flow variables can be determined for each node without needing information from other nodes. This is important when working with multiple threads, because it eliminates dependencies which can create race conditions and improper synchronization of shared variables.

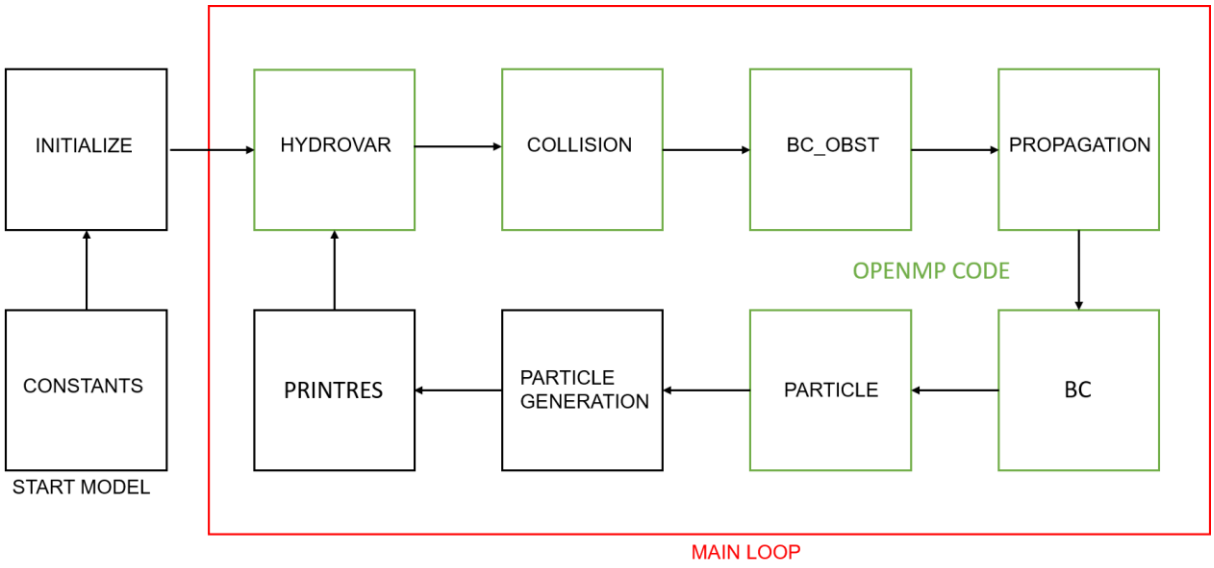

Figure 10. Overview of the different subroutines, with parallelized subroutines highlighted in green

Figure 6 shows in green the parallelized subroutines of the model. There is no need to parallelize the first two subroutines, as they are no part of the main loop, and only consist of a neglible fraction of computation time. For subroutines involving the computation of the fluid flow, and in patricular the subroutines not regarding boundary conditions, the *do* directive is the work-sharing directive of choice. Because these subroutines consists of two nested do-loops which cover the x and y range of possible fluid nodes, the collapse clause is used to pool all nodes into one large iteration space.

As the whole iteration space consists of roughly 40000 nodes, the chunk sizes used in the static scheduling clause can be taken as large chunks. A large chunk size does not necessarily improve the speed of the model, but saves on memory use. Instead of each thread needing a copy of each private variable for 1 iteration (default chunk size), they now only need a copy every 500 iterations. Within the first main subroutine are several *critical* directives to prevent any possible race conditions as well.

For the boundary condition subroutines simple *do* directives are implemented as well. However because the number of boundary nodes is significantly lower than the total fluid nodes, the chunk size has to be adjusted. If chunk size is significantly larger than the total amount of iterations required, some threads will remain unused and will lower model efficiency.

For the particle subroutine the *do* directive encompasses the main loop of all the particles. As there are a different number of particles in the system at any time, the default chunk size of 1 is assigned to this directive. Again, to prevent race conditions and dependencies, several *critical* directives are added in this subroutine.

The particle generation subroutine is a relatively light subroutine with a large amount of potential race condition scenarios. For this reason this subroutine is left unparalleled, for it to be effectively parallelized, a large part of this subroutine would fall in a *critical* directive, which forces the model to use only one thread. The print subroutine is not parallelized as well. The print subroutine has a relatively low impact on the model runtime, because it is not necessary to print the results each time step, but only on intervals.

Model Setup

This section will go over the variables and constants used in the model to provide the data that has been used in this study. To determine the effect of various conditions on the attachment rate of particles, and subsequently changes in porosity and permeability, a sensitivity analysis was performed using four different variables: particle radius R, zeta potential ζ_W and ζ_P, ionic strength I and horizontal flow velocity u. Besides variables the model requires a significant amount of constants and constant variables.

Table 1 shows all constants and variables used in the model.

Table 1 Overview of all parameters necessary for model setup.

DIMENSIONS: **FLUID DYNAMICS:**

$\boldsymbol{L}$	$200\ (\mu m)$	$\boldsymbol{\nu}$	$1 * 10^{-6}\ (m^2/s)$
$\boldsymbol{H}$	$50\ (\mu m)$	$\boldsymbol{\rho_w}$	$1000\ (kg/m^3)$
$\boldsymbol{H/H^*}$	$0.4\ (-)$	$\boldsymbol{\rho_p}$	$1055\ (kg/m^3)$
$\boldsymbol{R_1}$	$5\ (\mu m)$	$\boldsymbol{u_1}$	$10\ (m/day)$
$\boldsymbol{R_2}$	$2.5\ (\mu m)$	$\boldsymbol{u_2}$	$5\ (m/day)$
$\boldsymbol{R_3}$	$1.5\ (\mu m)$	$\boldsymbol{u_3}$	$1\ (m/day)$

DLVO:

$\boldsymbol{\epsilon_r}$	$80.2\ (-)$	$\boldsymbol{I_1}$	$0.3\ (M)$
$\boldsymbol{\epsilon_0}$	$8.85419 * 10^{-12}\ (F/m)$	$\boldsymbol{I_2}$	$0.05\ (M)$
$\boldsymbol{K_B}$	$1.38 * 10^{-23}\ (m^2kg/s^2T)$	$\boldsymbol{I_3}$	$0.001\ (M)$
$\boldsymbol{e}$	$1.6 * 10^{-19}\ (coulombs)$	$\boldsymbol{\zeta_{P1}}$	$-0.06\ (V)$
$\boldsymbol{N_A}$	$6.02 * 10^{23}$	$\boldsymbol{\zeta_{P2}}$	$-0.04566\ (V)$
$\boldsymbol{T}$	$293\ (K)$	$\boldsymbol{\zeta_{P3}}$	$-0.0175\ (V)$
$\boldsymbol{Z}$	1	$\boldsymbol{\zeta_W}$	$-\zeta_P$
$\boldsymbol{Ha}$	$0.4 * 10^{-20}\ (J)$		

In order to appropriately apply the chosen variables to the model, the variables have to be converted to units usable for the LBM. In order to do this variables inside the LB model have to be related to real physical variables. This is done through dimensionless equations like the ratio H/H^* or the Reynolds number:

$$Re = \frac{Lu}{\nu} \qquad 59$$

Where L is the characteristic length (i.e. pore diameter), u is flow velocity and ν is viscosity. From Chapter 1 it is determined that the lattice time step and lattice spacing (Δt and Δx respectively) are 1. This implies that converting domain length is done through $Domain\ length/Domain\ length_{LB}$. To find other variables, several approaches can be used.

The real physical units for ν an u and L are known, which implies that the Reynolds number is known as well. As the conversion for length units is known, to determine the other units, only u or ν has to be determined, as the Reynolds number should be equivalent in both real and LB units. From chapter 1 it is known that in the LB regime ν is related to the relaxation frequency τ through (when $\Delta t = 1$ and $\Delta x = 1$):

$$\nu = \frac{1}{3}(\tau + 0.5) \qquad 60$$

Now the first option is to choose u_{LB} and obtain ν_{LB} from equation 59 and τ from equation 60, The second option is to choose ν_{LB} and similarly find u_{LB} from equations 59 and τ from equation 60. The last option is to choose τ and subsequently find ν_{LB} from equation 60 and then u_{LB} from equation 59. The conversion rates can then simply be found relating the LB and physical variables to each other.

Because the time step Δt is 1, it is important to obtain a conversion factor for the time. This can be done by relating different conversion factors to each other. For example the conversion factor for time can be determined through the relation of u_{LB} and u, or their subsequent conversion factor c_u, and the conversion factor c_h.

$$c_u = \frac{c_h}{c_t}, \qquad c_t = \frac{c_h}{c_u}$$

The time conversion factor is of significant importance not only to determine the physical time that has passed within the model domain, but also to guarantee that particles cannot jump over the interaction energy barrier. If the time step is too large, the distance a particle may travel within one time step can exceed the range in separation distance in which the interaction energies may be active, and thus may get falsely attached to the pore surface.

The dimensions of the model domain are chosen such that particles have sufficient opportunity to attach, while also guaranteeing the influence of the pore constriction. H/H^* provides the ratio between the largest and smallest pore diameter. Viscosity and density ν and ρ_w are chosen such that they approximately represent the viscosity and density of water at 20° C. The density of the particles is chosen such that they are still affected by a density difference

between the water and the particle, but not dominated by it. DLVO constants are used for temperatures of 20°C or 293 K. The Hamaker constant is chosen such that it may roughly represent particles suspended in water [31, 32, 33].

The different variables used in the sensitivity analysis are chosen in such a way that combinations of different variables will create different types of attachment regimes, and consequently provide different porosity-permeability relations. The charges of ζ_P and ζ_W are chosen opposite to create an attractive DLVO regime. A repulsive regime is not considered in this study.

Using the physical value of ν, and the set dimensions of the model domain, the rest of the LB units are obtained such that when running the model with no particles, a steady state flow field may be established, and the time step is small enough to allow proper particle-particle and wall-particle interactions.

To obtain permeability from model data, the model saves the pressure gradient as well as the mean velocity. This allows for the use of Darcy's Law:

$$u = \frac{K}{\mu}\frac{\Delta P}{\Delta x} \tag{61}$$

Where K is permeability, u is flow velocity, μ is viscosity and $\frac{\Delta \mathrm{P}}{\Delta \mathrm{x}}$ is the pressure gradient. Simply rewrite to solve for K:

$$K = u\frac{\mu \Delta x}{\Delta P} \tag{62}$$

Using data obtained from the model implies that when calculating permeability this way, the permeability will be in LB units. This can either be converted into physical units, or, as has been done in this study, convert to the regularly used dimensionless permeability K/K_0, which needs no conversion from LB to physical units. K_0 here is taken to be the initial permeability.

Porosity is determined similarly to equation 53, using the void volume and bulk volume. However, for each time data is saved in the model, the porosity is defined as:

$$\phi = \frac{(PA - P_A * \pi R^2)}{PA} \tag{63}$$

Where PA is the area of the pore, P_A equals the number of attached particles that contribute to the solid phase of the system, and R is the radius of the particles. Particles are considered attached particles when they are attached to the pore wall, or are attached to the pore wall through other particles.

Results

This section will cover the data obtained by the model which is used in this study. The sensitivity analysis runs simulations of 4 different variables over a range of 3 values, which results in 81 different runs.

Although only positive-negative DLVO regimes are considered in this study, positive-positive regimes have been simulated. For that reason, the 81 runs are saved as all even numbers from 2-162. Table 2 gives an overview of the numbered runs corresponding to their proper parameter combinations, and will serve as a key, which may be referenced when discussing individual simulations.

Table 2 Overview of the different parameter combinations with their corresponding simulation number. Here the different values of $\boldsymbol{\zeta, I, U}$ and $\boldsymbol{R}$ were shown during the model setup section (Table 1).

	$\boldsymbol{\zeta_1 I_1}$	$\boldsymbol{\zeta_2 I_1}$	$\boldsymbol{\zeta_3 I_1}$	$\boldsymbol{\zeta_1 I_2}$	$\boldsymbol{\zeta_2 I_2}$	$\boldsymbol{\zeta_3 I_2}$	$\boldsymbol{\zeta_1 I_3}$	$\boldsymbol{\zeta_2 I_3}$	$\boldsymbol{\zeta_3 I_3}$
$\boldsymbol{U_1 R_1}$	2	8	14	20	26	32	38	44	50
$\boldsymbol{U_2 R_1}$	4	10	16	22	28	34	40	46	52
$\boldsymbol{U_3 R_1}$	6	12	18	24	30	36	42	48	54
$\boldsymbol{U_1 R_2}$	56	62	68	74	80	86	92	98	104
$\boldsymbol{U_2 R_2}$	58	64	70	76	82	88	94	100	106
$\boldsymbol{U_3 R_2}$	60	66	72	78	84	90	96	102	108
$\boldsymbol{U_1 R_3}$	110	116	122	128	134	140	146	152	158
$\boldsymbol{U_2 R_3}$	112	118	124	130	136	142	148	154	160
$\boldsymbol{U_3 R_3}$	114	120	126	132	138	144	150	156	162

To prevent this section from becoming cluttered, and to keep it clear and concise, three runs have been selected to represent how the data has been collected and processed to provide the corresponding results necessary for porosity-permeability analysis.

The three runs that are selected are runs that use the all the average parameters (Table 2: 28,82,136), but have different particle radii. For each simulation, every time the write subroutine (see Section Subroutines) saves data, a snapshot of the system was saved. These snapshots can be edited together to provide a video of the system. This provides a great visualization of the way particles are attached to the pore wall, and gives insight to the processes that may lead to any anomalies in the data, and will be referenced if needed. From the bulk data saved by the model, the porosity and permeability is read by a MATLAB script and processed further from there.

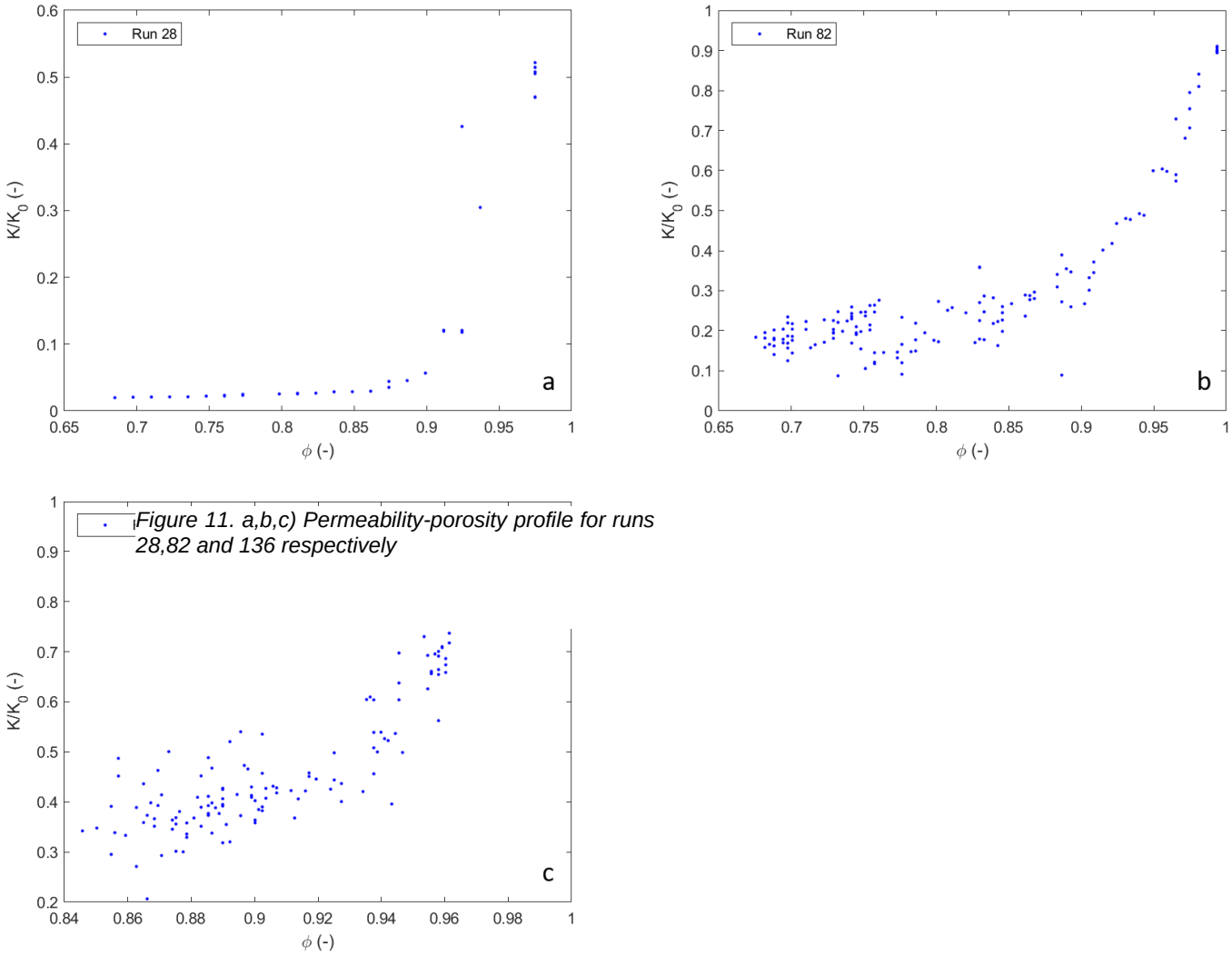

Figure 11. a,b,c) Permeability-porosity profile for runs 28,82 and 136 respectively

Figure 11 shows three different permeability-porosity profiles. In all cases as more particles attach to the pore surface, the permeability decreases. The distribution of the data points are significantly different from each other. Their differences can be well justified by having a visual representation as well.

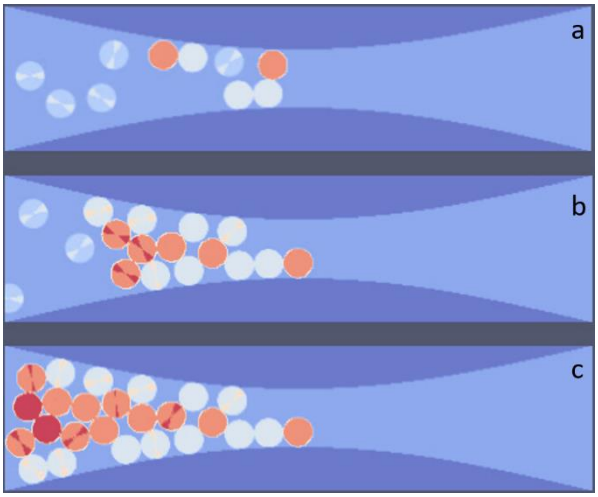

Figure 13. a) Snapshot at t=5600000 (2.24s). b) Snapshot at t=9000000 (3.6s). c) Snapshot at t=15600000 (6.24s). Snapshots are from run 28.

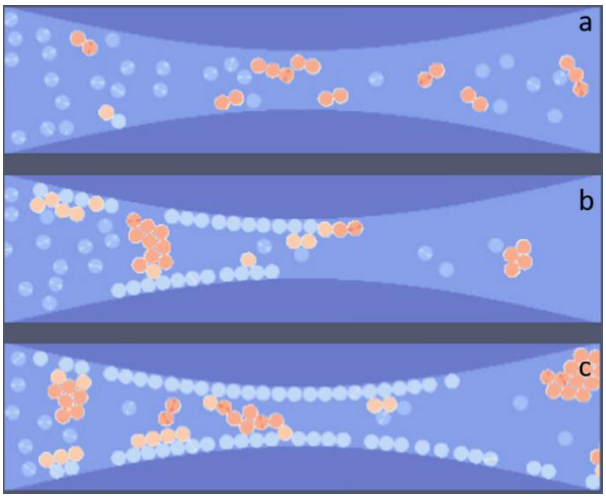

Figure 12. a) Snapshot at t=6800000 (2.72s). b) Snapshot at t=16000000 (6.4s). c) Snapshot at t=35600000 (14.24s). Snapshots are from run 82.

Comparing the video snapshots of run 28 and 82 (Figure 13 and Figure 12), and comparing Figure 11 a) and b), it shows how visual data can contribute to the understanding of the differences in permeability-porosity data distribution. During simulation 28 the pore throat gets clogged quickly in part because of the large particles. After it becomes clear that the hydrodynamic forces acting on the clogged area are not sufficient to break the blockage, the simulation is terminated. This firstly results in comparatively significantly less data points, and secondly in the permeability of simulation 28 dropping to effectively zero rapidly. More in depth discussion between differences in permeability-porosity distributions will follow in the upcoming Section. All permeability-porosity distributions may be found in the included Appendix A.

Discussion

This section of the report will elaborate on the obtained results. Firstly, differences and/or trends between the porosity-permeability results of the sensitivity analysis will be explored briefly. Secondly, the equation given by equation 57 will be applied to the porosity-permeability data. Thirdly, potential trends between equation coefficients and model variables will be considered. And lastly, improvements and further research will be reviewed.

Sensitivity Analysis

Because porosity is directly related to the attachment of particles, it is of vital importance to discuss the differences in particle attachment. This model considers an attractive DLVO regime, which implies that particle attachment is based on the relative power of the DLVO forces and hydrodynamic forces. If the hydrodynamic forces are large enough, they can overcome the attractive DLVO forces and prevent from being attached to the pore surface.

The different variables have different effects on the DLVO regime. Ionic strength I has a direct impact on the size of the Debye length κ (equation 44). This in turn has a large impact in determining the EDL energy. The zeta potential for the pore surface and particles, ζ_W and ζ_P determine the electric potential of the EDL. The zeta potential is an indicator of stability of colloids as well. High zeta potential indicates higher stability, and less capability of coagulation and flocculation [34].

The hydrodynamic forces are determined by the flow velocity u. A higher flow velocity will provide a larger hydrodynamic force and will make it harder for the DLVO forces to capture particles. The particle radius is a high impact variable. Not only are the DLVO forces affected by the radius of the particles, but due to the pore constriction, particles size has a relatively large influence on the straining and clogging of the pore. As will also be discussed later, straining and clogging of pores have high consequences for the porosity-permeability profiles. Furthermore, increasing particle size increases particle mass, making it harder for hydrodynamic forces to move the particle.

The highest impact on the porosity-permeability profiles arises when particles attach near the pore constriction, and subsequently clog the pore. The permeability becomes practically zero. This is why the relative effective impact of the different variables here will be largely based on the clogging of the pore. Table 3 is a copy of Table 2, however, in red are the simulations in which the pore gets clogged, and the hydrodynamic pressure building up is not sufficient to unclog the pore. In green are the simulations where no clogging occurs.

Table 3 Overview of clogging (red) that occurs at any given combination of variables. Here the different values of $\boldsymbol{\zeta, I, U}$ *and* $\boldsymbol{R}$ *were shown during the model setup section (Table 1)*

	$\zeta_1 I_1$	$\zeta_2 I_1$	$\zeta_3 I_1$	$\zeta_1 I_2$	$\zeta_2 I_2$	$\zeta_3 I_2$	$\zeta_1 I_3$	$\zeta_2 I_3$	$\zeta_3 I_3$
$U_1 R_1$	2	8	14	20	26	32	38	44	50
$U_2 R_1$	4	10	16	22	28	34	40	46	52
$U_3 R_1$	6	12	18	24	30	36	42	48	54
$U_1 R_2$	56	62	68	74	80	86	92	98	104
$U_2 R_2$	58	64	70	76	82	88	94	100	106
$U_3 R_2$	60	66	72	78	84	90	96	102	108
$U_1 R_3$	110	116	122	128	134	140	146	152	158
$U_2 R_3$	112	118	124	130	136	142	148	154	160
$U_3 R_3$	114	120	126	132	138	144	150	156	162

Table 1 is constructed from observing data from Appendix A and visual data. In all simulations with the largest particle size, pore clogging occurs. This is primarily due to the geometry of the system. The ratio of the pore throat to pore constriction H/H^* is 0.4. This implies that on a 50 μm pore throat, the constriction is 20 μm wide. The largest particle diameter is taken to be 10 μm. This, in combination with particles being funneled into the constriction results in all the simulations with that size of particle to become clogged.

The first 27 simulations, up to run 54, include the largest particle size. After that, it can be seen that clogging still occurs, but not exclusively. With particles of intermediate size, and small

size, a strong ionic strength appears to be the controlling factor of whether the pore becomes clogged or not. Whereas at larger particle size, the geometry of the system guaranteed clogging, at smaller particle sizes, the geometry has a lesser influence and the attachment is controlled through hydrodynamic and DLVO forces. Because the particles are smaller, more particles need to be deposited in order for clogging to occur.

When the ionic strength is high enough, the attractive forces are high enough to overcome the hydrodynamic forces even at high flow rates. Eventually enough particles will attach to the pore surface to cause clogging of the pore. Simulation runs with intermediate ionic strength show that the attractive DLVO forces are unable to overcome the hydrodynamic forces, except for when the flow velocity is lowest. Simulations with the lowest ionic strength are free of clogging regardless of flow velocity or zeta potential.

There are several other patterns that can be observed regarding porosity-permeability profiles and a change in variables. When the ionic strength is lowest, although there may be flocculation and coagulation, there is little attachment of particles. The particles in suspension will however have an impact on the pressure gradient within the system. This results in porosity-permeability profiles which have a very small range in porosity, and a high variability in permeability on similar porosities.

With intermediate ionic strength, observations show an increase in the range in porosity, as more particles get attached. Although there is no clogging, permeability in these profiles tends to decrease more than in low ionic strength simulations. This is due to further constriction of the pore by attached particles.

Although flow velocity is not the main influencer in terms of likelihood of clogging, there is a notable influence flow velocity has on particle attachment and subsequent data point spread. Comparing for example sets of changing zeta potential and flow velocity (specifically comparing the sets of 146/152/158, 148/152/158 and 150/156/162), there is striking similarity in the spread of data points between scenarios in which zeta potential changes while flow velocity remains constant. This suggests that flow velocity has a larger influence on the

attachment of particles then zeta potential. Lower flow velocities imply that DLVO forces may more easily overcome the hydrodynamic forces and allow particle attachment.

An anomaly can be observed in 126, which, given high ionic strength and low zeta potential, has a high likelihood of enough particle attachment to clog the pore. During this run particles seems to mostly attach far enough away from the pore constriction to allow enough room for other particles to pass. Given more time, there is a significant chance that this pore would be constricted as well.

Simulation 144 seems to be an anomaly as well, but when observing the porosity-permeability profile of 132 and 138, combined with visual data, there is near clogging at later time steps (Figure). Similarly to run 126, given more computation time, the chances of clogging become significantly higher.

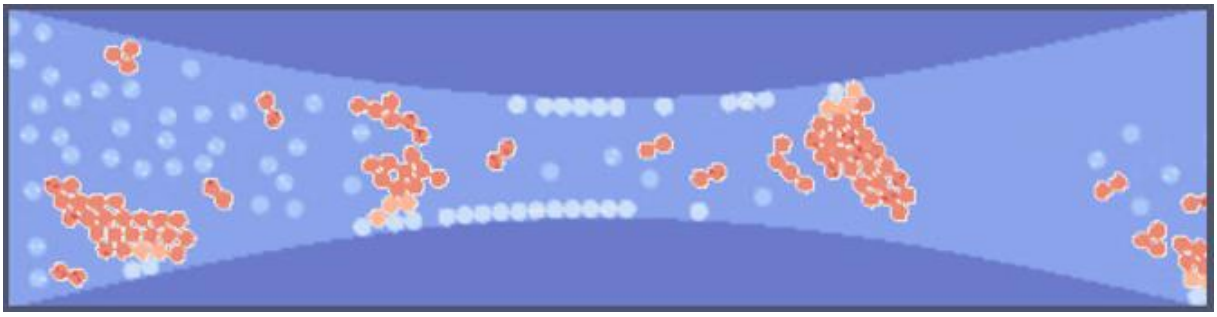

Figure 14. Overview of particle attachment at t=119200000 (47.68s) snapshot from run 132.

Porosity-Permeability Relation

Next the general Kozeny-Carman relation has been applied to the porosity-permeability profiles. The applied equation as mentioned in the previous section:

$$\frac{K}{K_0} = a\frac{\phi^b}{(1-\phi)^c} \qquad 57$$

The Kozeny-Carman equation in this form (equation 56) is mainly applied to porous media on the pore network scale. This implies that there will never be a porosity of 1. However, due to the definition of porosity in this study (equation 63), the porosity will be 1 until a particle has deposited. Therefore, data in the porosity-permeability profiles have omitted any entry of a porosity of 1.

Appendix B will show all applicable fit results for equation 57. Several will be highlighted here and discussed. A proper fit in this study is defined by two criteria. The first being if the curve conforms to realistic expectations of the behavior of permeability and porosity based on the model domain and setup. The second being if within the confidence intervals the fitted coefficients are still necessary for the data to be fitted. One example is if the 95% confidence interval for coefficient a, b or c in equation 57 crosses the value of 1. In this case, the coefficient will have no real influence on the outcome of the curve, as $x^1 = x$, and $1 * f(x) = f(x)$. Another example is when the confidence interval of either b or c crosses a value of 0. This implies that the variable or part of the equation to which it is the power of, is unnecessary in its entirety, as $x^0 = 1$.

A clear distinction can be observed when comparing fit results between different simulations. In general, when the pore becomes clogged, the general Kozeny-Carman relation will not provide a proper fit. The curve provided by the fit function for the unclogged pores follows the given data significantly better. There are fringe cases where clogging occurs, but relatively slow, or where momentary clogging occurs. In these cases, the equation will provide a proper fit. However, when the pore gets clogged rapidly, there a near guarantee that the equation will not yield a proper fit.

There may be several factors controlling this observation. The first is the type of slope the fit function has to provide for the given data. When pores get clogged, $K/K_0 > 0.1$ in a relatively small amount of registered data points. This is well visualized in several simulations.

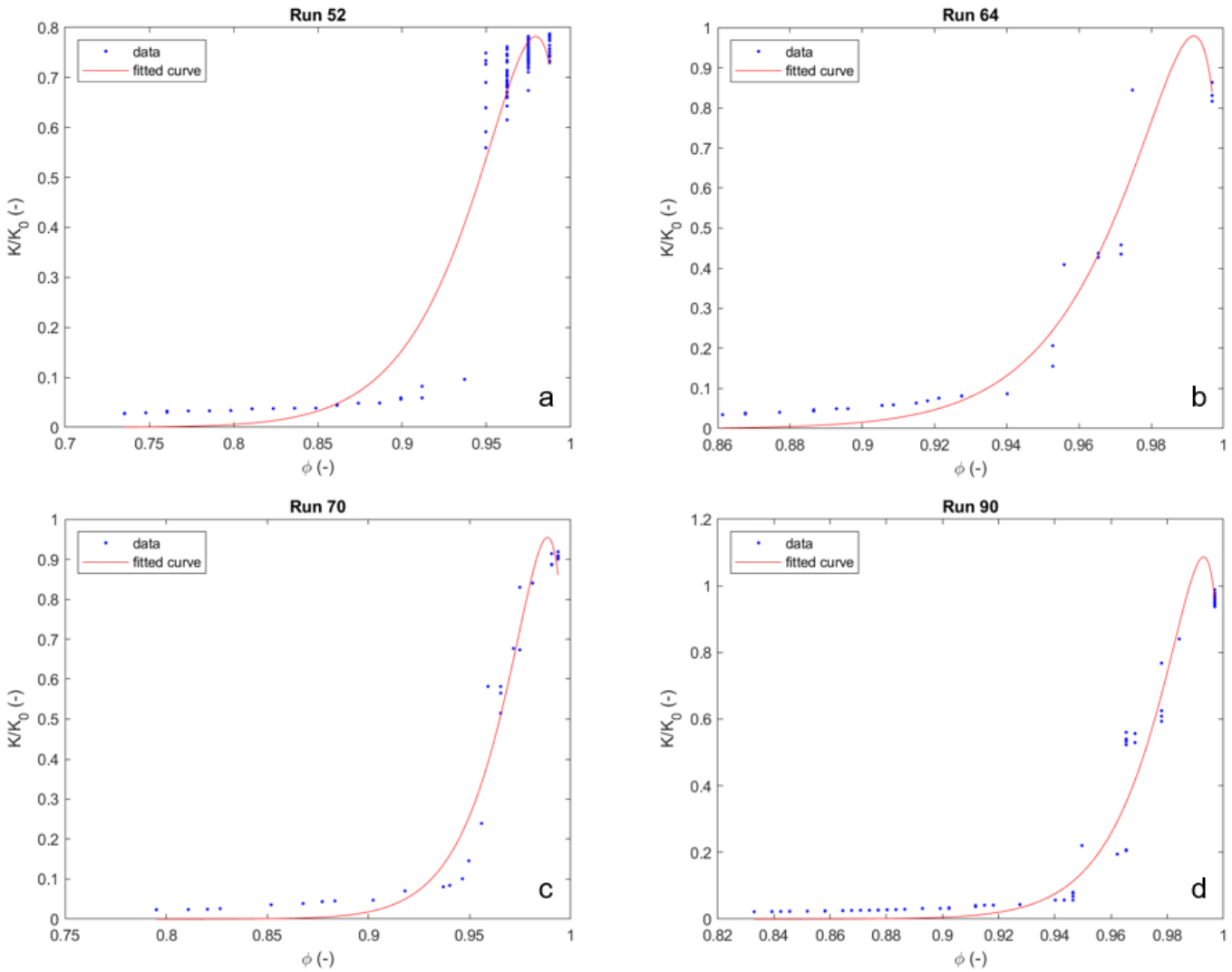

Figure 15. Result of data fitting of run 52 (a), run 64 (b), run 70 (c), and run 90 (d). All these simulations represent clogged scenarios.

Figure 15 shows four different results of fitting equation 57 for simulation 52, 64, 70 and 90. During simulation 52, it is worth noting that the particle radius is largest. It takes a relatively long time with relatively little particle attachment before the pore becomes clogged. Therefore a large amount of high porosity and high permeability data points have been collected. However, because of the clogging of the pore, very low permeability data has been collected as well. Due to the data points being concentrated in specific areas, the equation becomes increasingly hard to fit to the data. During simulation 70, a similar pattern may be observed, although less pronounced.

When observing Figure 15**Error! Reference source not found.**, the fits of the simulations look promising. The fits underestimate lower permeabilities, which may be justified by the fact

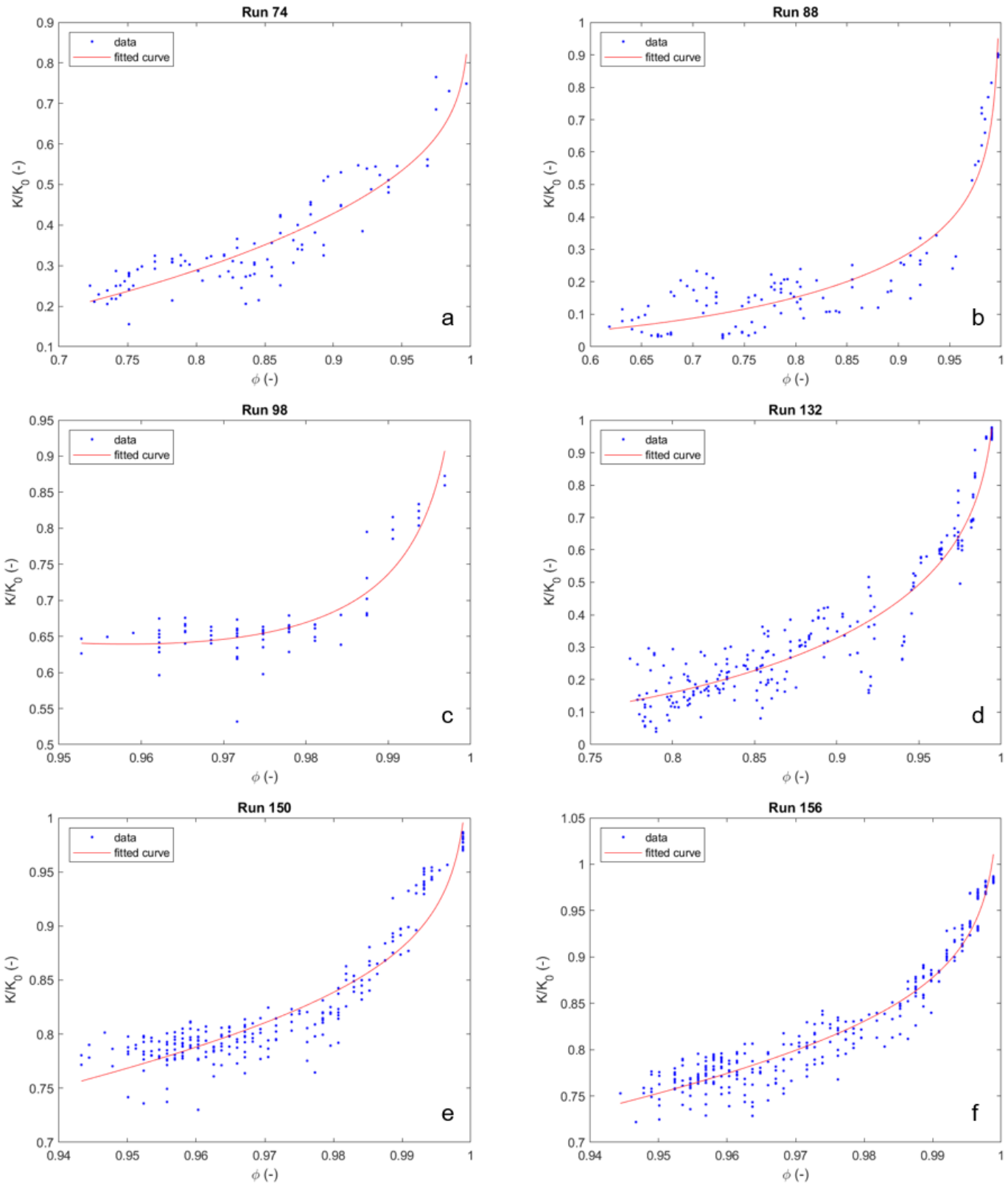

Figure 16. Result of data fitting of run 78 (a), run 88 (b), run 98 (c), run 132 (d), run 150 (e), run 156 (f). All of these simulations represent unclogged scenarios.

that after clogging, the practical permeability becomes zero anyway. The main issue with the fits is the bend in the curve at higher dimensionless permeabilities. Given the model domain

and setup, the dimensionless permeability should be unable to decrease with an increase in porosity. Although not universally, this erroneous curve is exclusively observed in simulations where pore clogging develops. This bend is caused by coefficient c. If this coefficients drops below zero, then the shape of the curve changes. This can be resolved by setting the lower bound for coefficient c to zero, which will be discussed shortly.

In contrast to clogged scenarios, an unclogged pore provides a significantly better fit. This is mainly due to the spread of data points. Not only is the slope of the curve less steep, with a higher average minimum permeability, but there are comparatively more data points between the higher and lower permeabilities (Figure 16). From Appendix B can be observed that for all unclogged simulation (Table 3, green), equation 57 presents a visually acceptable prediction of the porosity-permeability data.

However, regarding the previously mentioned criteria, while the unclogged pores conform to the first criteria of a proper fit, several of the runs do not conform to the second criteria. Table 4 highlights the values of the coefficients and their corresponding confidence intervals. Coefficient b may well be set to 1 within the 95% confidence interval. Figure 17 shows the resulting difference in fit when coefficient b is set to 1 in case of simulation 150. This has been shown to illustrate the difficulties in providing an equation to universally apply to the provided data, or even only data of an unclogged regime.

Table 4 Overview of coefficients for simulation 150

	$\boldsymbol{Value}$	$\boldsymbol{Lower\ bound}$	$\boldsymbol{Upper\ bound}$
$\boldsymbol{a}$	0.704618	0.692602	0.837369
$\boldsymbol{b}$	1.295917	0.866969	1.724864
$\boldsymbol{c}$	0.051211	0.004491	0.057512

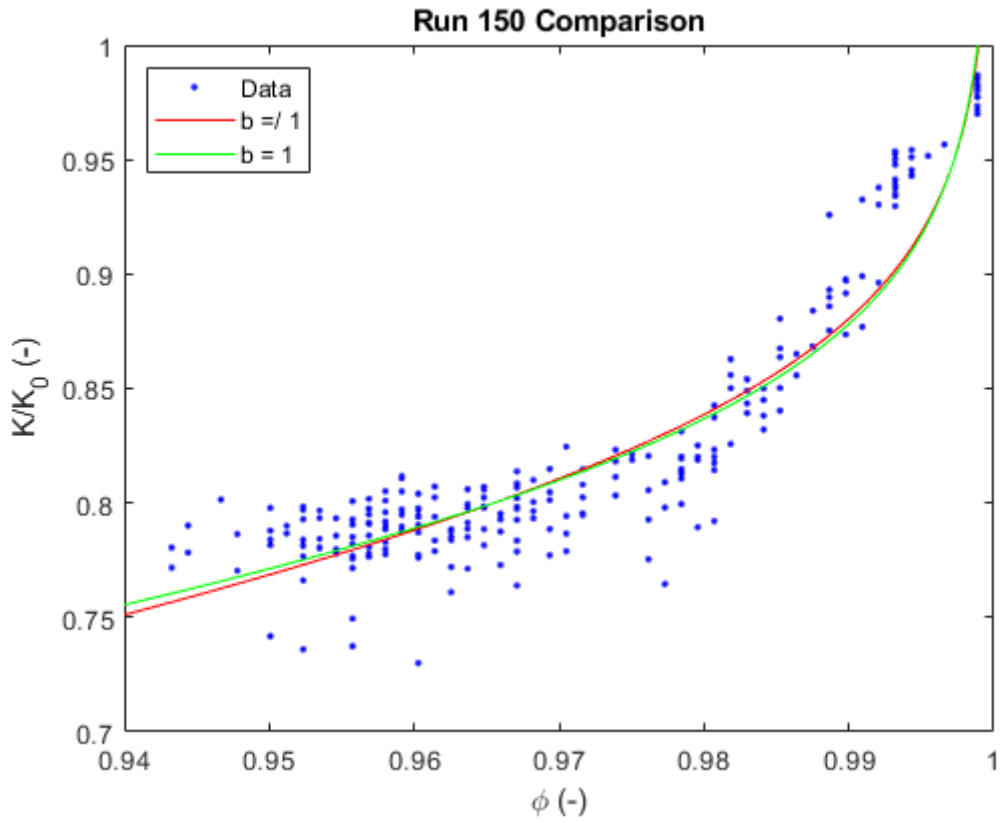

Figure 17. Overview of the difference between coefficients b for simulation 150.

As demonstrated in the previous part of this section, equation 57 works well for unclogged scenarios. For clogged scenarios, the equation is unfit for the data provided, therefore an alternative equation will be suggested here. Recalling the issue regarding coefficient c, setting lower bounds to zero reduces the denominator in equation 57 to 1. This lower bound of zero is reached in most instances of clogged pores. Thus, a simpler power relation will be applied, given by [6]:

$$\frac{K}{K_0} = a\left(\frac{\phi}{\phi_0}\right)^b \qquad 64$$

There are several general observation to be made when evaluating the resulting curves. The first is that they conform to realistic expectations of the modeled system, unlike equation 57 (Figure 15). The second is that this fails to produce a proper curve when the minimum K/K_0 is relatively high. The goal of this equation is to give a better estimate of clogged pores, in which it is successful. There are however several other observations that will be highlighted.

If the spread of porosity is relatively large, and the spread of permeability is large, then the curve will underestimate permeability at lower porosities. In clogged scenarios it is of larger interest to know the evolution the system at higher permeabilities, as when the pore get clogged, effective permeability is zero anyway. However, if the spread of porosity is relatively small, and the spread of permeability remains large, the curve will overestimate permeability at lower porosities. As the spread in data points becomes more gradual, and the change of permeability over smaller porosity ranges becomes larger, the overestimation at lower porosities becomes higher. An example of these observation can be seen in Figure 18.

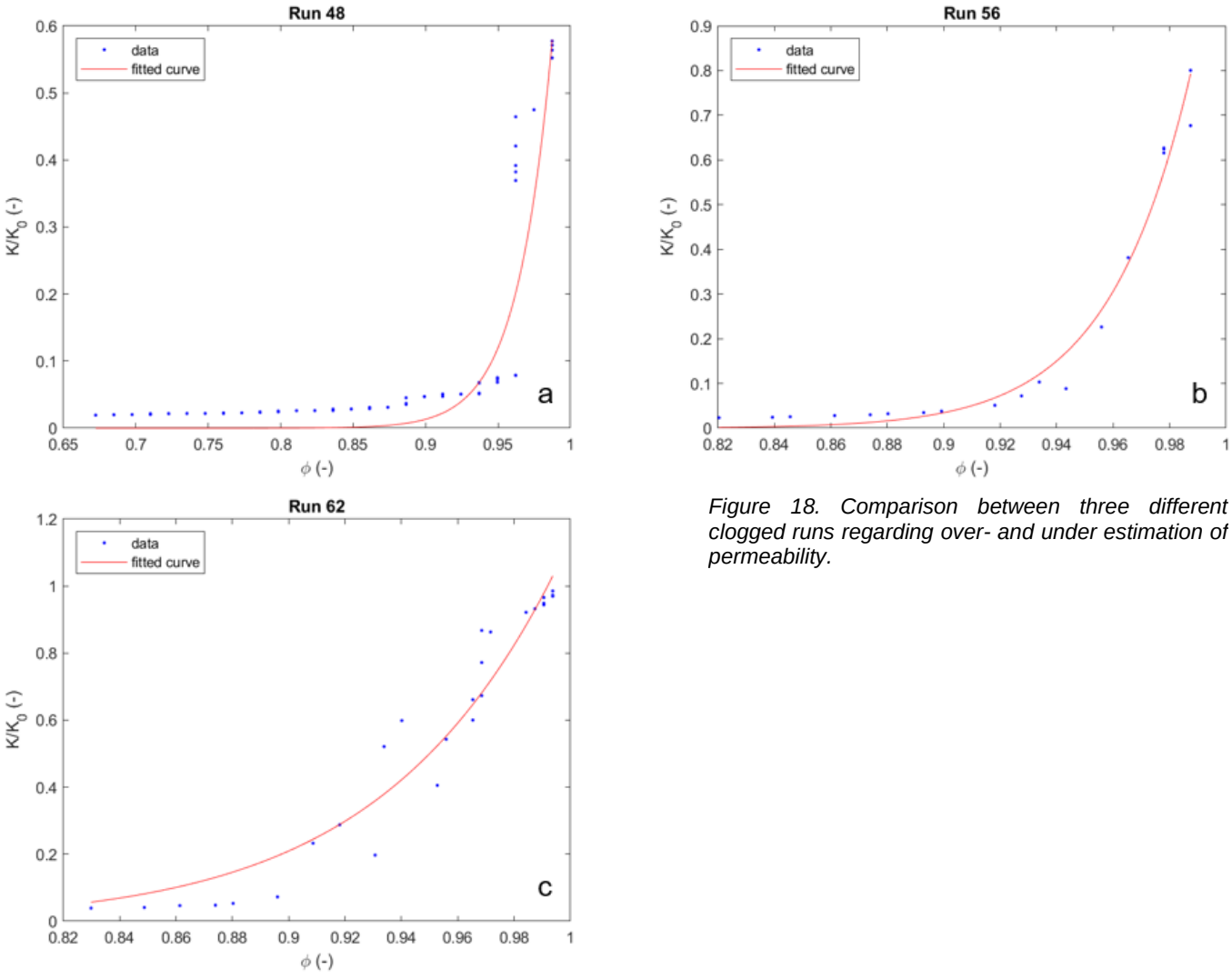

Figure 18. Comparison between three different clogged runs regarding over- and under estimation of permeability.

Another observation that can be made from the coefficients a and b from equation 64 relates to the confidence intervals and necessity of coefficients. Coefficient a allows more flexibility in fitting a function, which is convenient when fitting fewer, more spread out data points. These kind of data points are mainly observed in the simulations up to and including number 54. It is therefore not unexpected to observe that coefficient a and their confidence intervals are nearly exclusively near or passing the value of 1 after simulation 54. Therefore equation 64 may well be simplified further to include only coefficient b for clogged pores beyond scenario 54. All fit results for equation 64 may be found in Appendix C.

Coefficient Trend Analysis

Although equation 57 and 64 give a fair estimate of porosity-permeability, it is highly unlikely that one or two equations will provide the means to predict the porosity-permeability relations in this study, as the data belongs to a highly un-linear system. The system will inevitably provide non-monotonic relations between system properties such as porosity and permeability. Therefore to qualitatively compare that data as a whole will be more difficult.

To analyze the effect of the different variables on porosity-permeability, the data will be broken up into smaller selections. The selection of comparisons will be focused on one variable each. There are however several restrictions here to which variables can effectively be analyzed. Any scenario where particle radius or ionic strength remains constant, will result in at least one of the three scenarios being a simulation where clogging occurs, and the rest of the three being simulation(s) where no clogging occurs. An effective analysis of coefficients cannot be made when the same equation does not apply to all the data sets. Furthermore, any anomalies in the data, caused by for example partial clogging, will inherently shift the fitted curve and provide coefficients that are unsuitable for effective analysis. The simulations that can ultimately selected are those that when taken in groups of three, consist of either three clogged scenarios, or three unclogged scenarios. This results in different sets of simulations that are to be compared for the two remaining variables, flow velocity u and zeta potential ζ. The evaluated groups are shown in Table 5, where the enclosed sections in groups of three

show possible comparisons between flow velocity, and consecutive simulations similarly in color in groups of three show possible combinations between different zeta potentials.

Table 5. Overview of all evaluated sets of simulations. Possible combinations are sets of three that are all clogged(red), or unclogged(green), and that are either sets of three in enclosed sections, or sets of three of consecutive runs of the same color.

	$I_1\zeta_1$	$I_1\zeta_2$	$I_1\zeta_3$	$I_2\zeta_1$	$I_2\zeta_2$	$I_2\zeta_3$	$I_3\zeta_1$	$I_3\zeta_2$	$I_3\zeta_3$
U_1R_1	2	8	14	20	26	32	38	44	50
U_2R_1	4	10	16	22	28	34	40	46	52
U_3R_1	6	12	18	24	30	36	42	48	54
U_1R_2	56	62	68	74	80	86	92	98	104
U_2R_2	58	64	70	76	82	88	94	100	106
U_3R_2	60	66	72	78	84	90	96	102	108
U_1R_3	110	116	122	128	134	140	146	152	158
U_2R_3	112	118	124	130	136	142	148	154	160
U_3R_3	114	120	126	132	138	144	150	156	162

For each of the groups of three shown in Table 5 the applicable coefficients (b for equation 64, and a, b and c for equation 57) are plotted against their respective changes in variable, implying that a change in that specific variable may lead to changes in coefficients. The goal is to find trends within the data that may suggest predictability in the modeled system.

When trying to obtain trends from individual simulations sets, it becomes clear that there is a lack of data to effectively provide any indication of trends. There are however, some noteworthy observations when comparing sets of three to each other. First, clogged scenarios regarding equation 64 will be evaluated, then unclogged simulations regarding equation 57 will be considered.

For both flow velocity and zeta potential, the porosity-permeability profile for all combination of clogged scenarios with radius R_1 ($5\ \mu m$) are extremely depended on the time it takes for the pore be become clogged. In some instances, pores get clogged within relatively little timesteps,

and in others some particles may be deposited before the smallest part of the pore constriction, delaying pore clogging. This results in such a wide variety in profiles, that there is no real trend to be distinguished when comparing different sets of three.

As mentioned previously for clogged pores with a radius smaller than $5\ \mu m$, coefficient a from equation 64 was reduced to 1, which leaves only one coefficient, b to be evaluated. Although there are no distinguishable trends showing regarding zeta potential (Figure 19), when observing changes in flow velocity (Figure 20), a notable similarity of sensitivity to changes in flow velocity from the norm may be observed. Coefficient b is generally highest at the average value, and generally is lower at the extremes. For equation 64, coefficient b determines the slope of the curve, and the slope is depended on the distribution of the porosity-permeability data. Coefficient b may be higher at average flow velocities, because different effects occur at lower and higher velocities. At higher velocities, clogging becomes increasingly difficult due to the increase in hydrodynamic forces, particles will attach less frequently and clogging takes longer. However, at low velocities, the relative impact density differences have become larger, allowing more particles to attach near the front of the pore constriction. Both these processes may result in a more gradual clogging of the pore, and therefore provide a gentler slope than on average flow velocities.

When analyzing unclogged pores, equation 57 provides three different coefficients. This allows for more accurate fitting of the given data, but does increase the difficulty in trend analysis. There is however notable observed behavior between the three different coefficients. Figure 21 through 26 show the coefficient plots for all coefficients between changes in zeta potential and flow velocity. Uniformly, the behavior of coefficients is identical between coefficients a and b, and there is an inverse relation between coefficients a and b, and c. So if between two points, coefficients a and b exhibit an increase, coefficient c will decrease. This may not necessarily provide insight in the modeled system, and be more depended on the nature of the used equation, but it does allow the same qualitive analysis regarding sensitivity of changes in coefficients regarding changes in variables zeta potential and flow velocity. Similar to the power law used for clogged pores, coefficient b determines the main slope of the

curve, while a mainly calibrates the starting point, and c has a small corrective influence on the latter end of the curves. As coefficient b is the most impactful coefficient, and a and c respond predictably to changes in b, mainly coefficient b will be discussed.

For both flow velocity and zeta potential (Figure 22 and Figure 25), changes in coefficients from the mean are not guaranteed to increase or decrease. However, regarding flow velocity u, generally the absolute change in coefficients from the mean is smaller from high velocities to the mean than from low velocities to the mean, implying that low velocities have a higher impact than large velocities.

Although there is no similar observation that can be made for changes in zeta potential, zeta potential does show larger discrepancies between extremes and the mean. This implies that extremes in zeta potential have a much larger impact relative to mean values than flow velocity does. Hydrodynamic force on particles is modeled relatively linearly through equations 29 through 32, while zeta potential has a significantly more non-linear implementation through equations 42 and 43. This would suggest that changes in changes in flow velocity, and thus changes in hydrodynamic force on particles, may behave more linearly to changes in zeta potential.

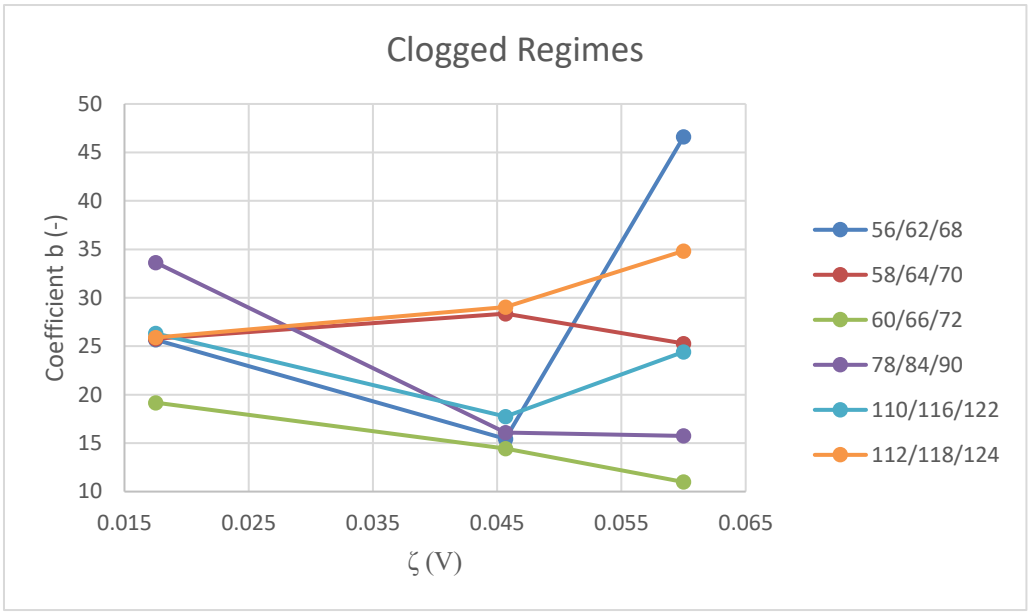

Figure 19. Coefficient b for changes in zeta potential in clogged regimes.

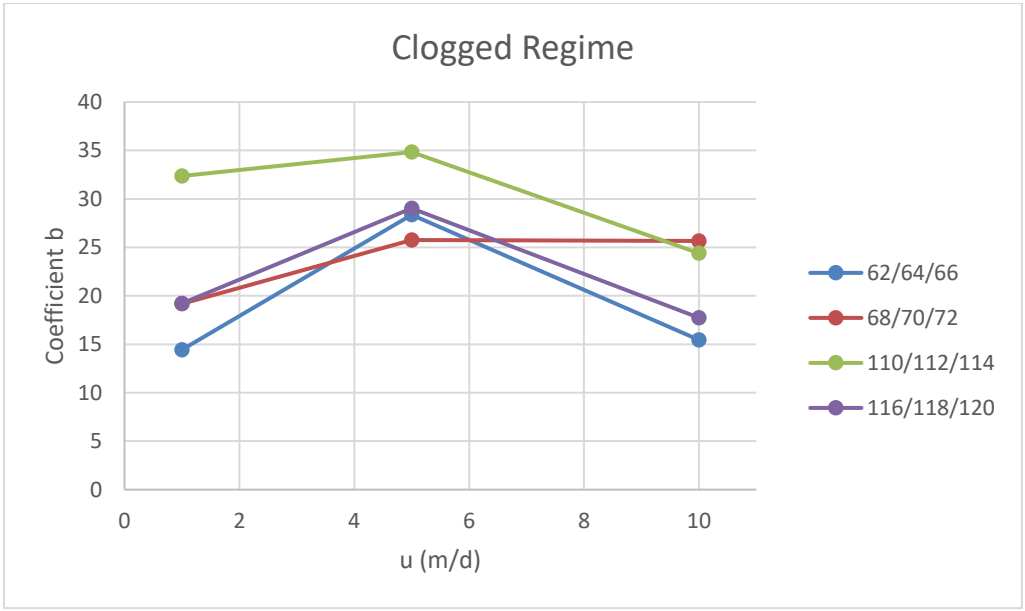

Figure 20. Coefficient b for changes in flow velocity in clogged regimes.

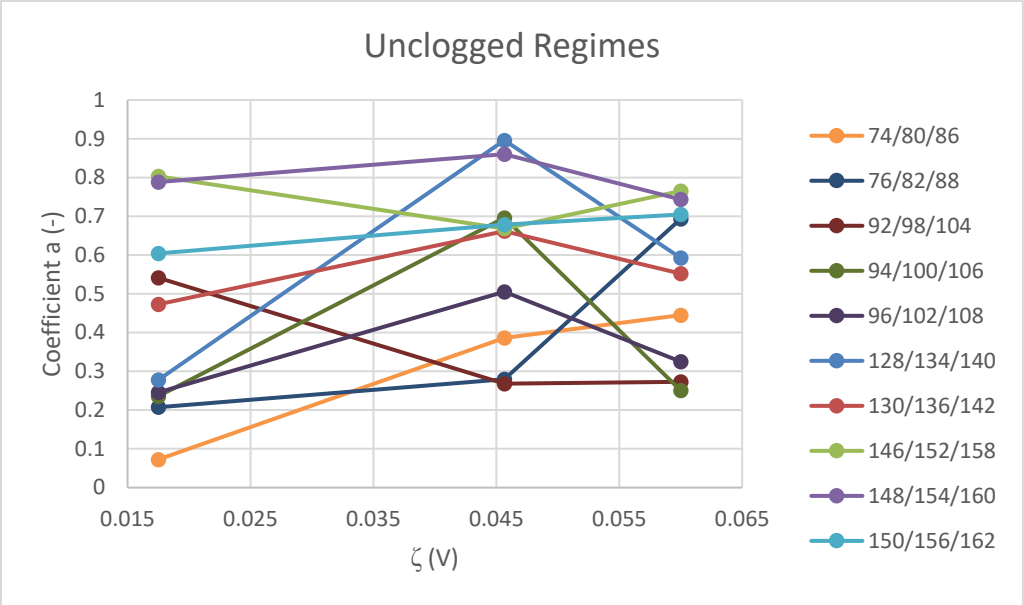

Figure 21. Coefficient a for changes in zeta potential in unclogged regimes.

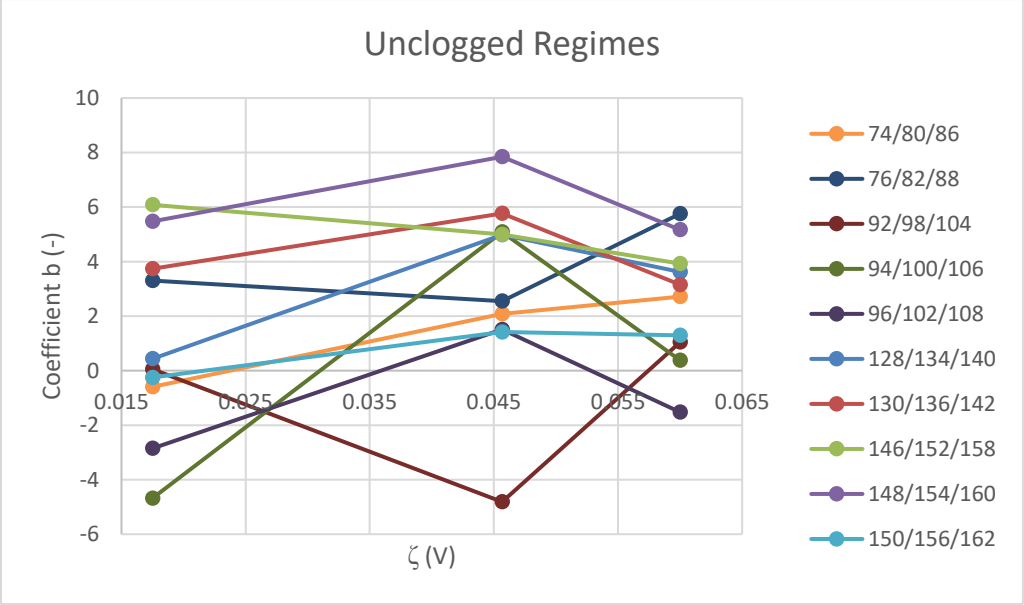

Figure 22. Coefficient b for changes in zeta potential in unclogged regimes.

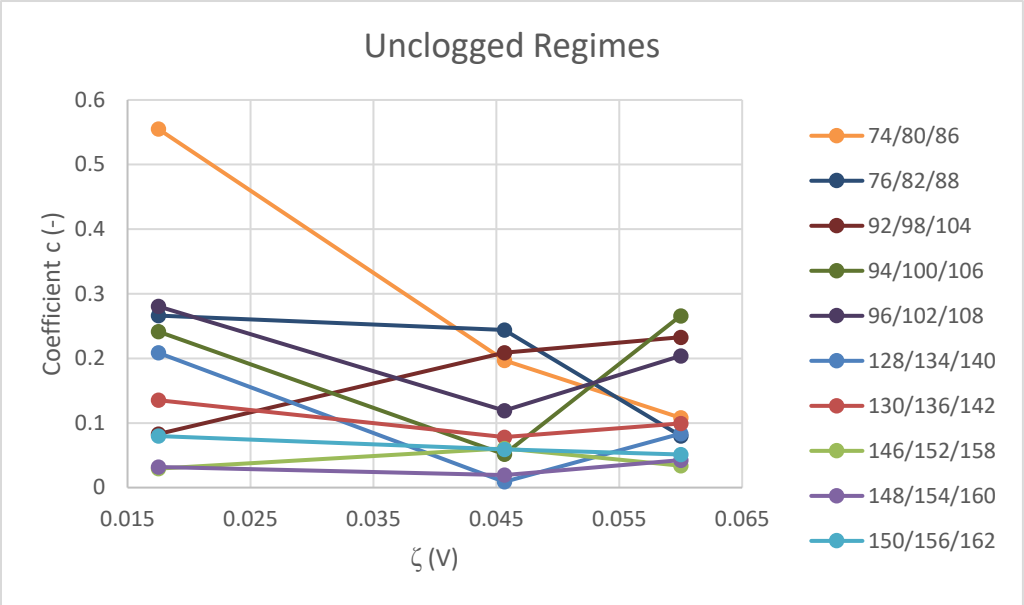

Figure 23. Coefficient c for changes in zeta potential in unclogged regimes.

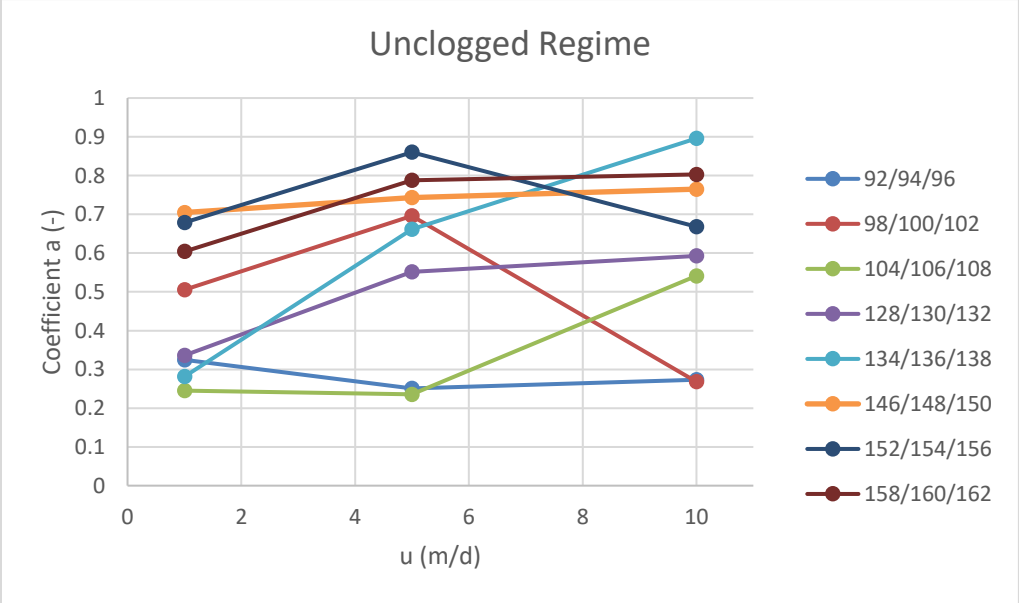

Figure 24. Coefficient a for changes in flow velocity in unclogged regimes.

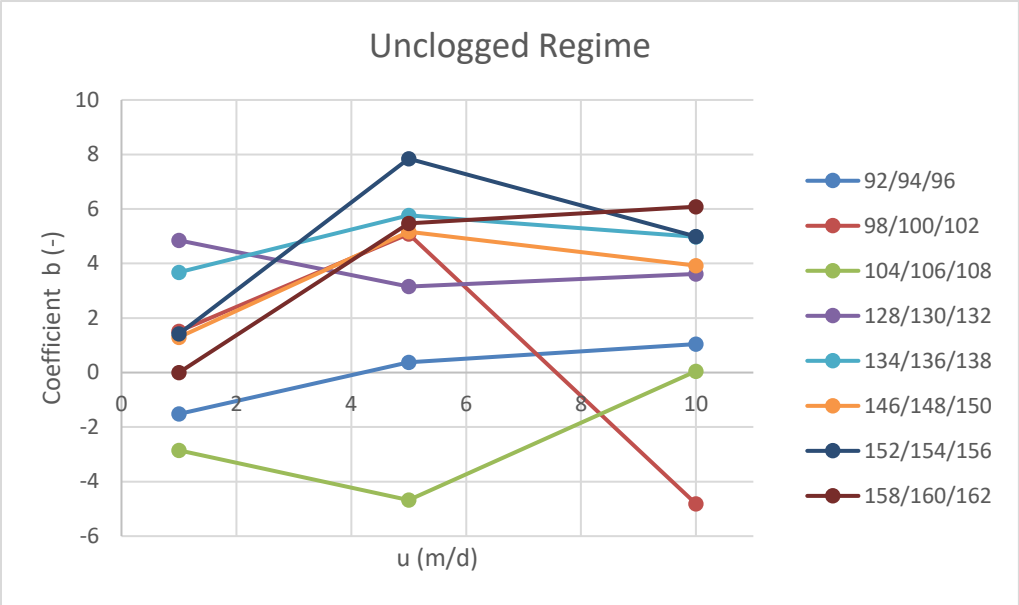

Figure 25. Coefficient b for changes in flow velocity in unclogged regimes.

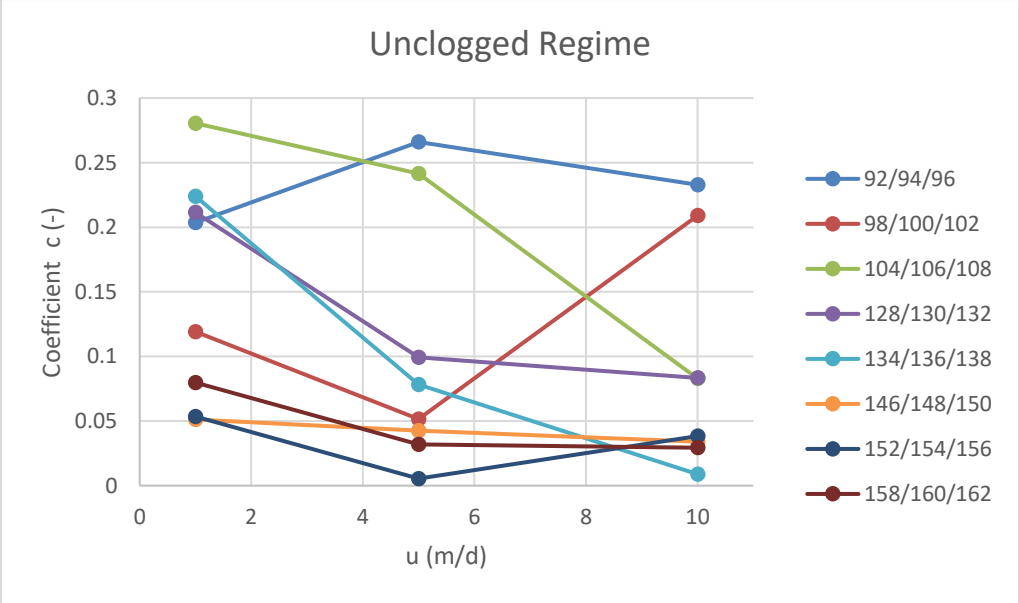

Figure 26. Coefficient c for changes in flow velocity in unclogged regimes.

Improvements

This part of the discussion will focus on the potential improvements and future research that may lead to more accurate and conclusive results. There are several reasons why the coefficient trend analysis cannot provide conclusive results. The first is the type of system that is being modeled. As mentioned before, the types of equations modeled in this study are highly non-linear. This implies that any change in variables, may already have relatively unpredictable results.

The second reason is that way the porosity-permeability data is obtained inherently provides a large spread in data points. Fitting data with a large spread in data points increases the difficulty of finding a proper fit, and results in a large potential spread in the confidence of the fitted coefficients.

Especially in simulations where there is little to no attachment, mainly simulations with a low ionic strength, the way data points are distributed can become misrepresented. Take for example run 160. Here ionic strength, zeta potential and particle radius are at their lowest respective values. Flow velocity is average. There is very little particle attachment, as may be seen from the snapshots provided by Figure 27. However, besides the existing particles in the domain having an impact on the permeability, making the spread in permeability increasingly variable. Through the way porosity is calculated (equation 63), anytime a particle or a group of particles attach themselves to an already deposited particle, but does not remain attached to that deposited particle, the porosity may change disproportionally to the permeability (Figure 27). Figure 19 shows two snapshots of simulation 160. It can be seen that at both times, several particles are attached to already deposited particles, which are counted towards a decrease in porosity. However, in both cases, in the next timestep hydrodynamic forces were large enough to detach the particles again from the primary deposited particles.

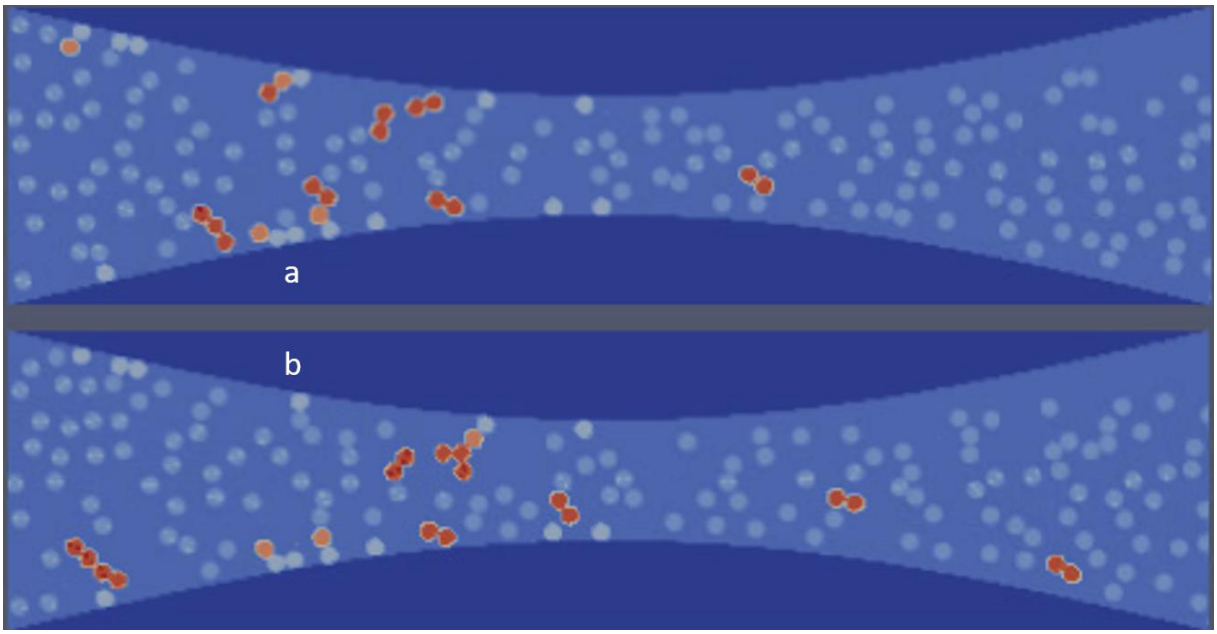

Figure 27. a) Snapshot of simulation 160 at t=17200000 (6.88s). b) Snapshot of simulation 160 at t= 19200000 (7.6s).

Another reason is that when trying to discover trends in data, three data points are not enough to justify any trend that may seem to be present. Notably the combination between an already spread out data set that provides the coefficients needed for the analysis, and the lack of data points in the coefficient analysis make it difficult to provide any evidence for any observable trends.

When trying to model these kinds of systems, simplifications in the model may lead to more predictable results. However, when modeling on this scale with the intend of improving process understanding, it is imperative that processes are to be modeled as closely as they would in reality. Based on insight obtained on this scale, then through up-scaling to scales useful for practical application, simplifications are more easily permitted.

To try and resolve misrepresented porosity-permeability data would imply that an improved or different way of calculation porosity is required. One suggestion may be that only particles or aggregations that are attached for a certain threshold of time-steps, and therefore have had significant impact on the permeability are recorded and used in porosity calculations. However, the same approach may be used, accepting and acknowledging its shortcomings, as long as this method is used consistently in future research.

To resolve the lack of data points, the only option is to expand the sensitivity analysis to include a wider range in variables. As the pore constriction seems to have significant influence on at least particles of large radii, another suggestion may be to include different sizes of pore constrictions. This however means a significant increase in computation time and resources. Through this solution trends within coefficients may be observed which would provide more predictability of these kinds of systems as well.

Future research may include, as mentioned above, a wider range of variables. Furthermore, this model is based on a simple instance of a porous medium, with particles of identical size, valence and zeta potential. The model may be adjusted to provide a wide range of particle radii, differences in valence and different zeta potentials between particles. Properties of the pore wall and medium may be adjusted to accommodate to specific problems. Another suggestion might be to model non-spherical particles, although this would be relatively more difficult than previously mentioned suggestions.

Conclusion

The goal of this study was to evaluate if, on a micro-scale, conventional porosity-permeability relations may be used to predict porosity-permeability relations, similar to larger scales. Depending two regimes – clogged and unclogged regimes – porosity-permeability may accurately be described by a generalized power law or a generalized Kozeny-Carman equation respectively.

The additional goal of this study was to find any trends between the obtained coefficients of the fitted equations on their respective regimes and the change in variable. The data belong to a highly un-linear system. Such a system provides non-monotonic relations between system properties such as porosity and permeability. Due to this and the lack of data points for comparison, no conclusive trends may be found within the given data. However, it may be concluded that zeta potential is much more sensitive to changes than flow velocity.

Future research might include a wider range in sensitivity analysis, to provide a wider range in data points, with which trends might be more easily observed.

Appendix A

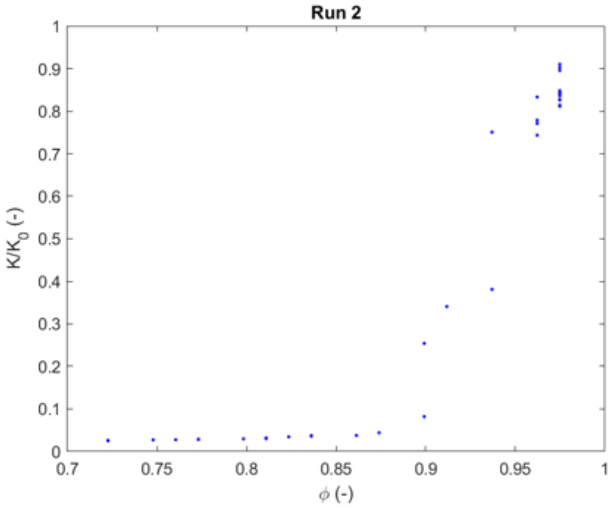
Run 2
K/K0 (-)
ϕ (-)

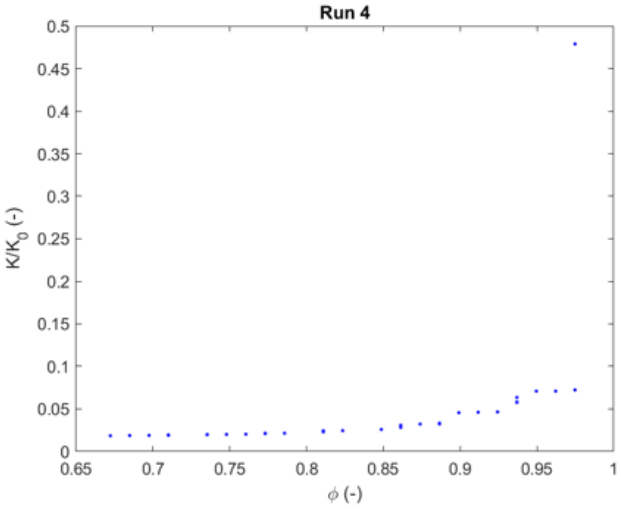
Run 4
K/K0 (-)
ϕ (-)

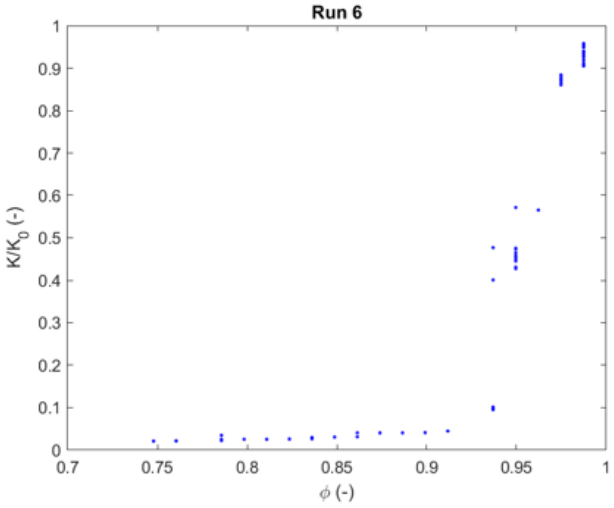
Run 6
K/K0 (-)
ϕ (-)

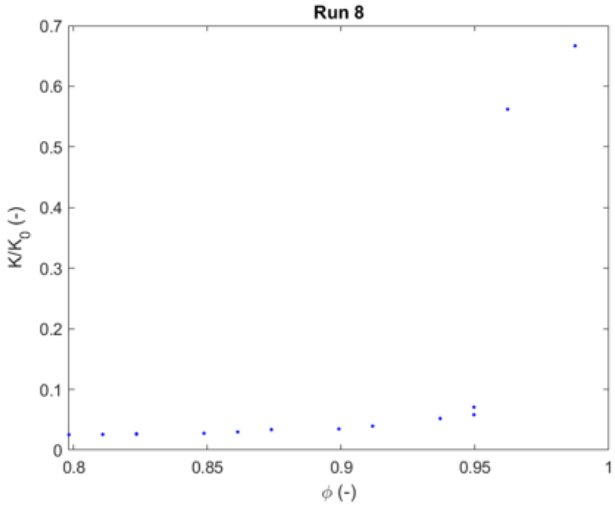
Run 8
K/K0 (-)
ϕ (-)

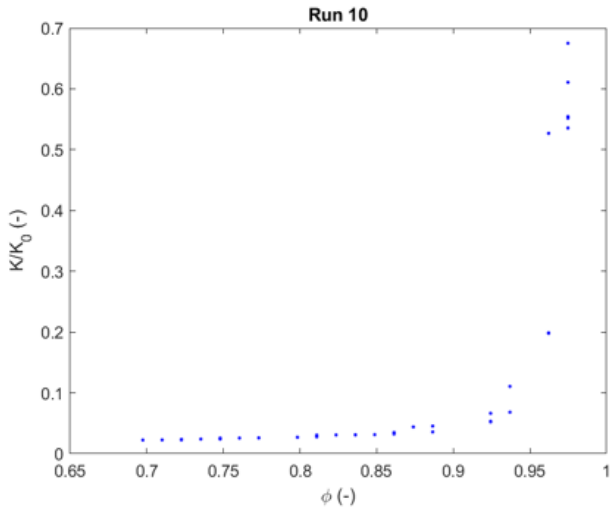
Run 10
K/K0 (-)
ϕ (-)

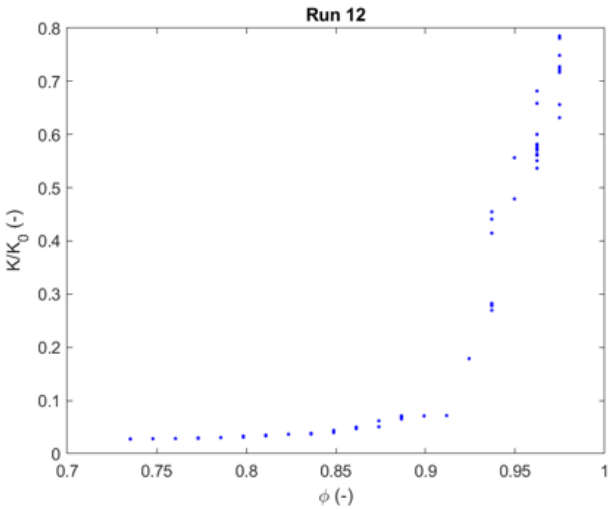
Run 12
K/K0 (-)
ϕ (-)

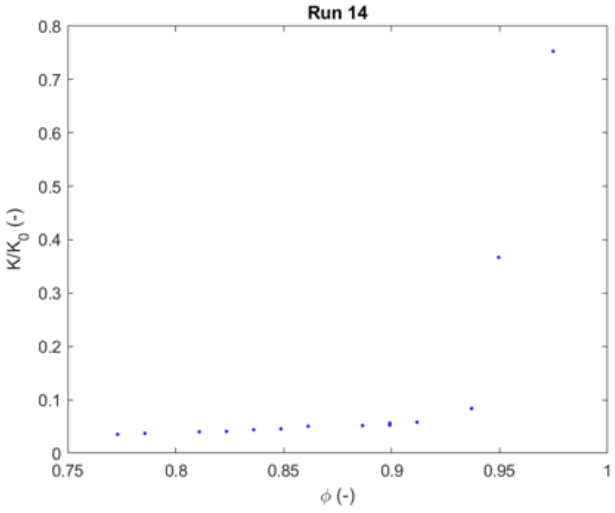
Run 14
K/K0 (-)
ϕ (-)

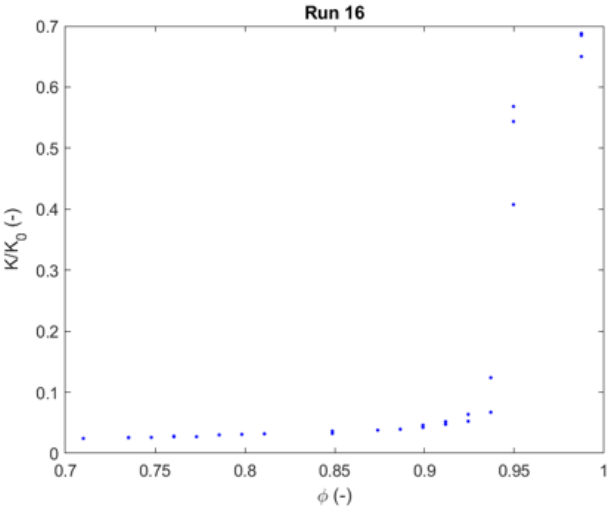
Run 16
K/K0 (-)
ϕ (-)

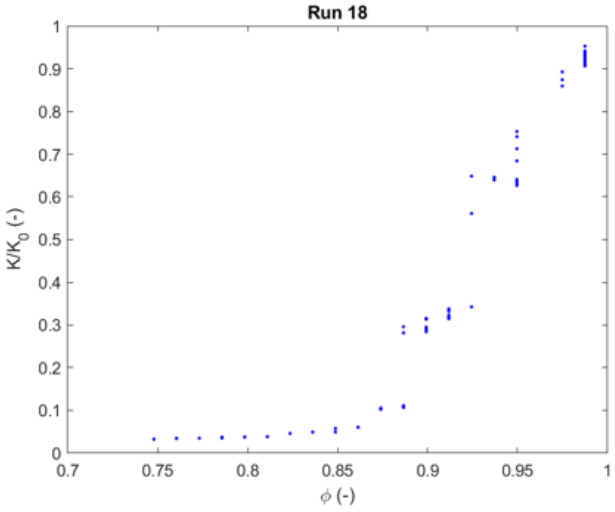
Run 18
K/K0 (-)
ϕ (-)

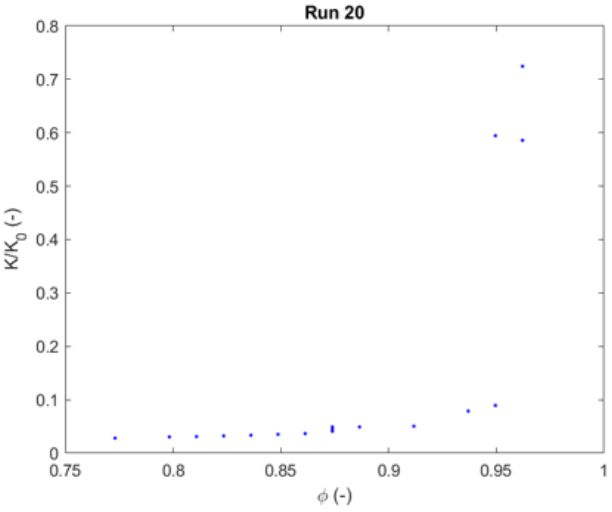
Run 20
K/K0 (-)
ϕ (-)

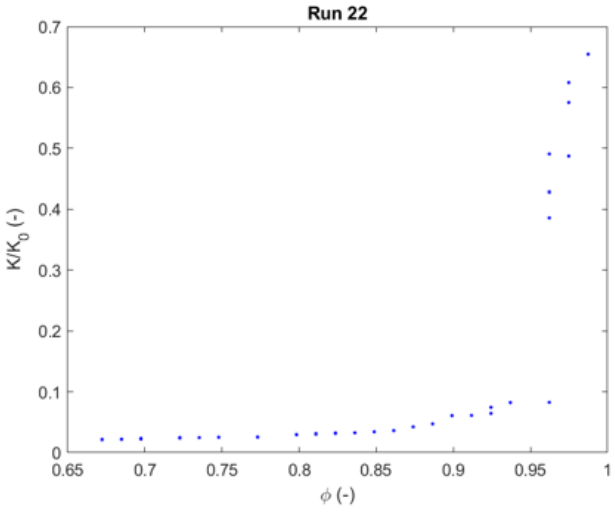
Run 22
K/K0 (-)
ϕ (-)

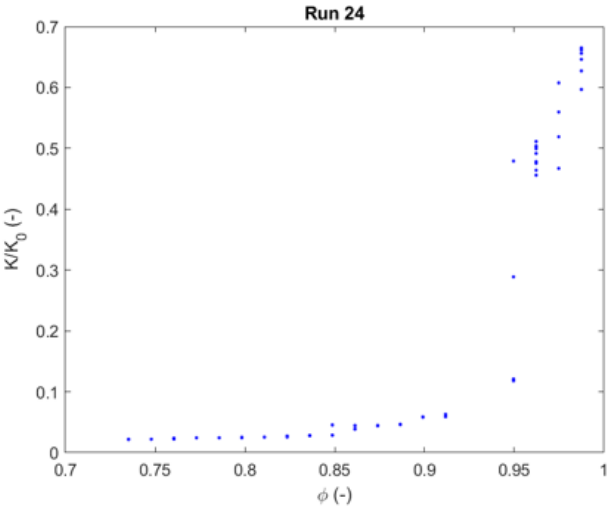
Run 24
K/K0 (-)
ϕ (-)

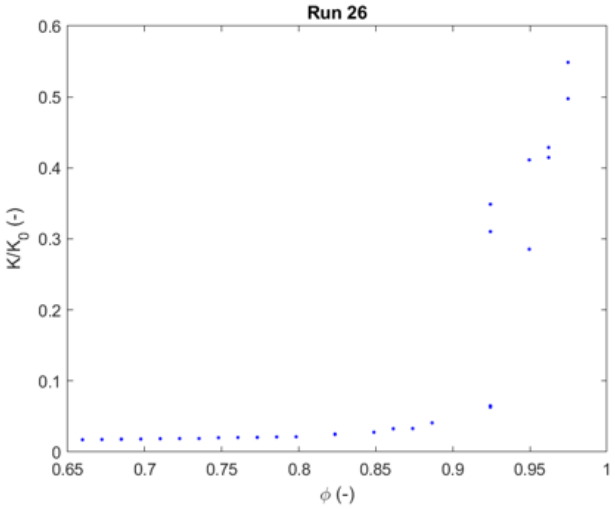
Run 26
K/K0 (-)
ϕ (-)

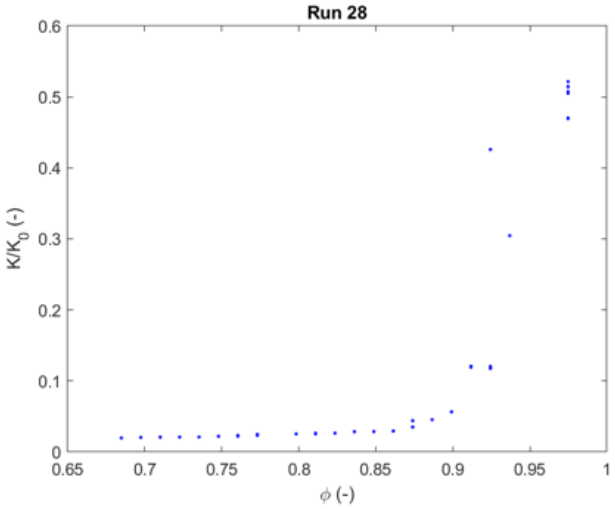
Run 28
K/K0 (-)
ϕ (-)

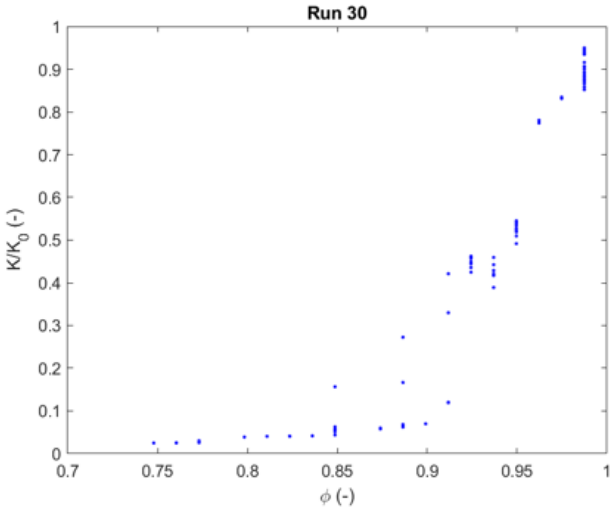
Run 30
K/K0 (-)
ϕ (-)

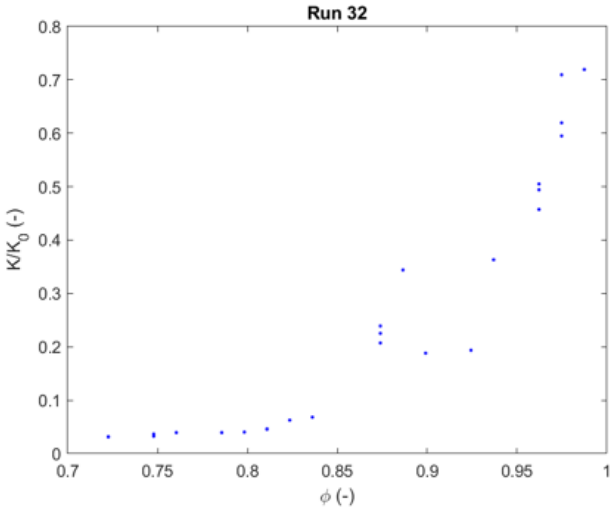
Run 32
K/K0 (-)
ϕ (-)

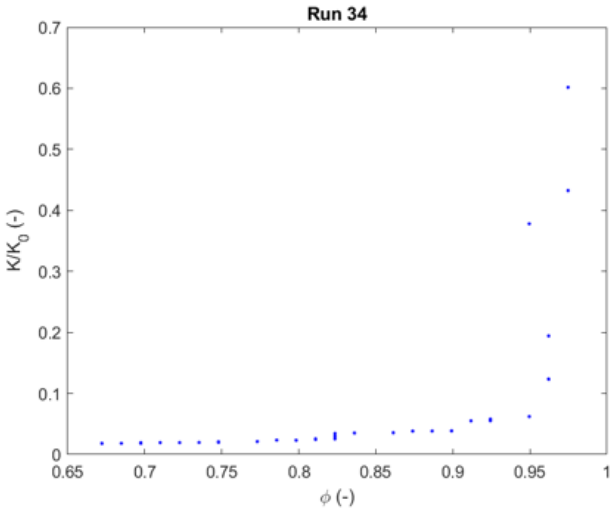
Run 34
K/K0 (-)
ϕ (-)

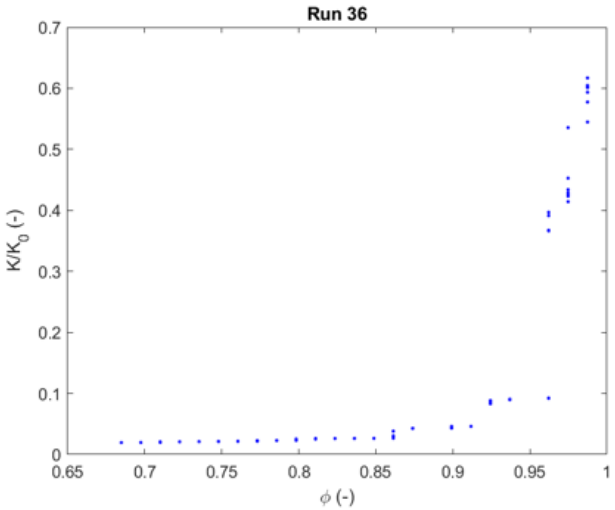
Run 36
K/K0 (-)
ϕ (-)

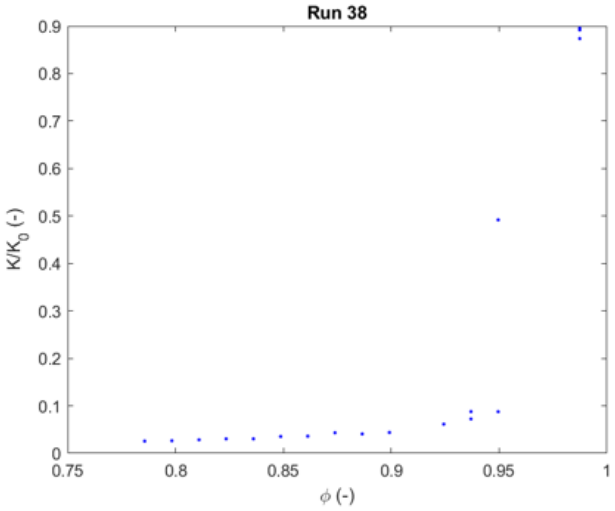
Run 38
K/K0 (-)
ϕ (-)

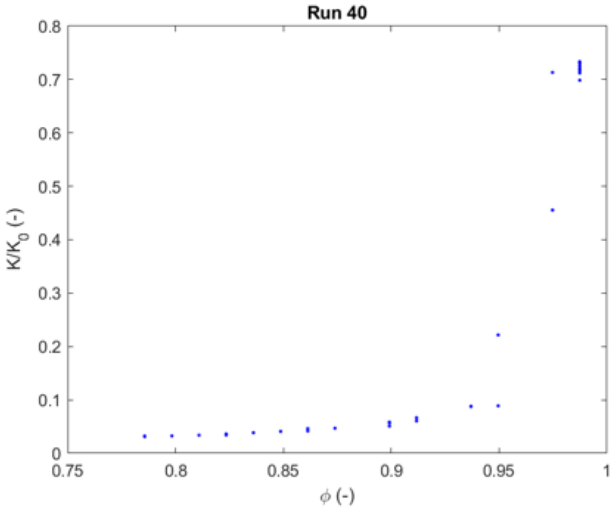
Run 40
K/K0 (-)
ϕ (-)

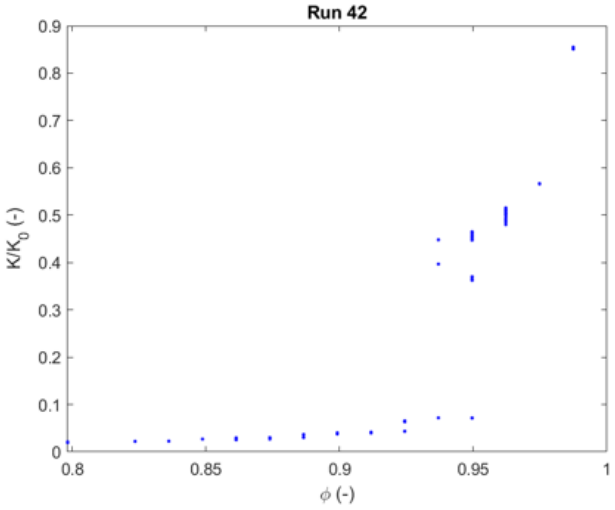
Run 42
K/K0 (-)
ϕ (-)

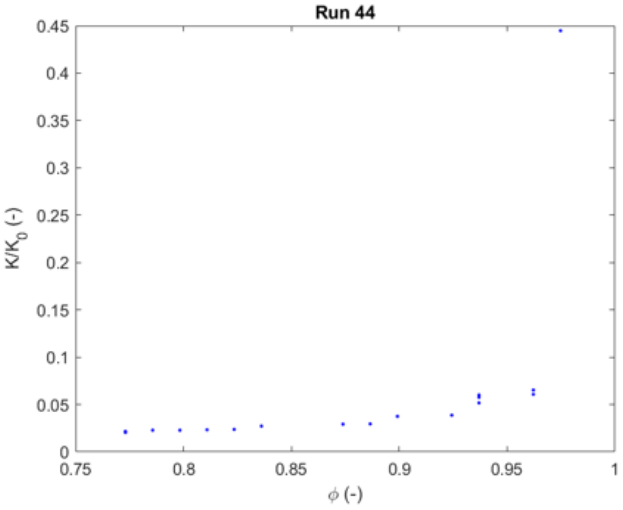
Run 44
K/K0 (-)
ϕ (-)

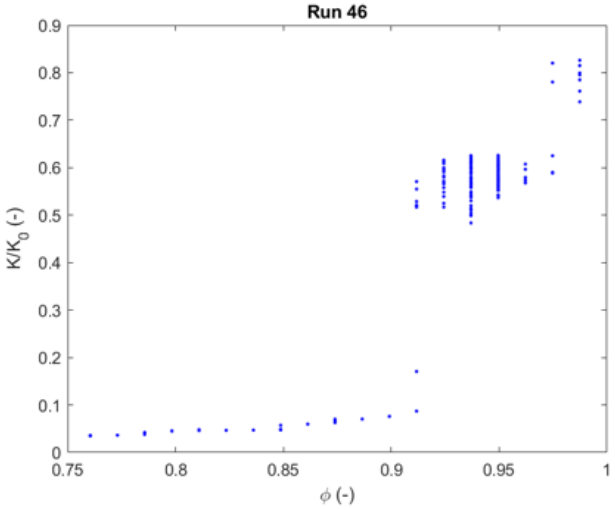
Run 46
K/K0 (-)
ϕ (-)

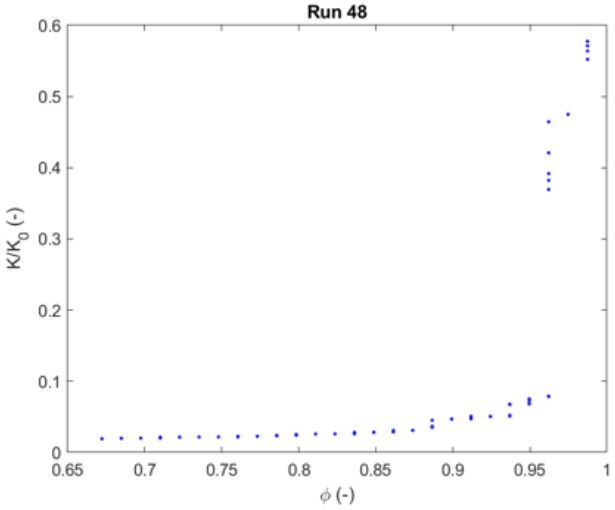
Run 48
K/K0 (-)
ϕ (-)

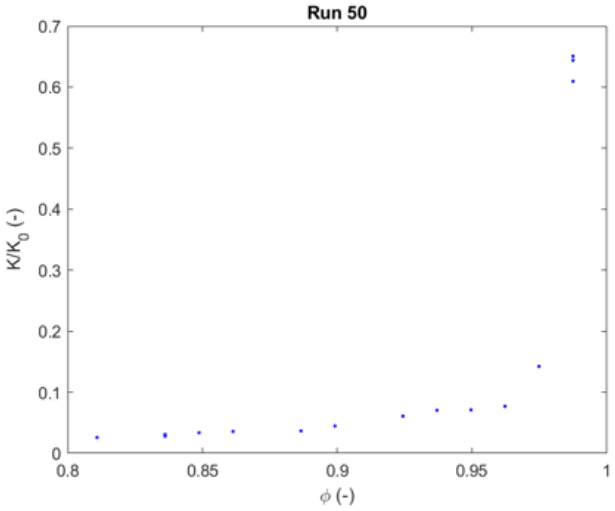
Run 50
K/K0 (-)
ϕ (-)

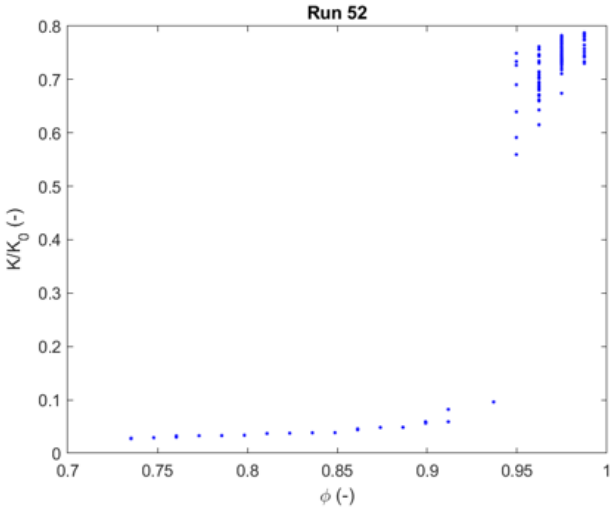
Run 52
K/K0 (-)
ϕ (-)

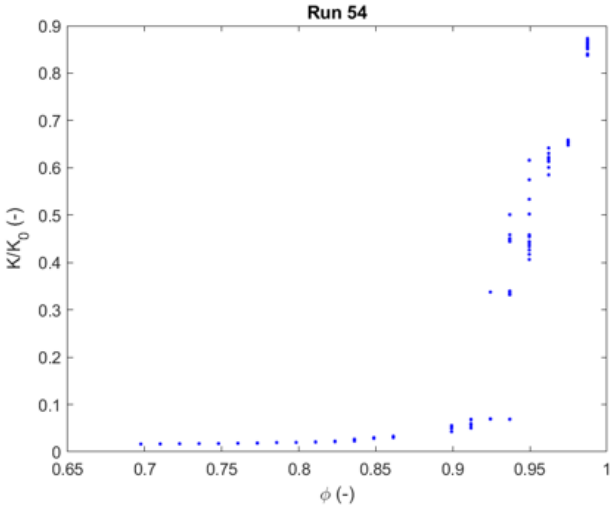
Run 54
K/K0 (-)
ϕ (-)

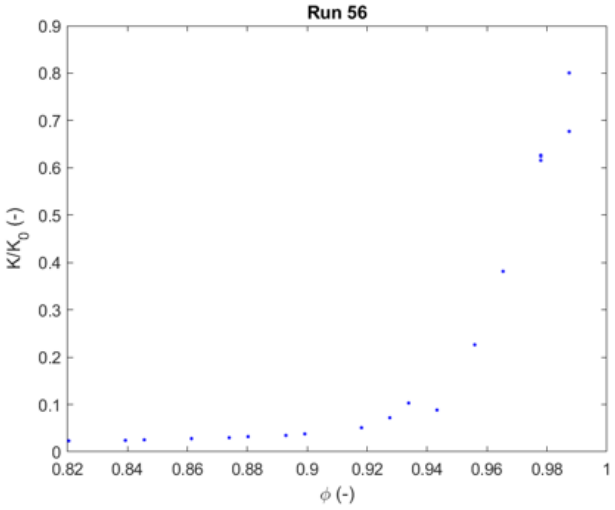
Run 56
K/K0 (-)
ϕ (-)

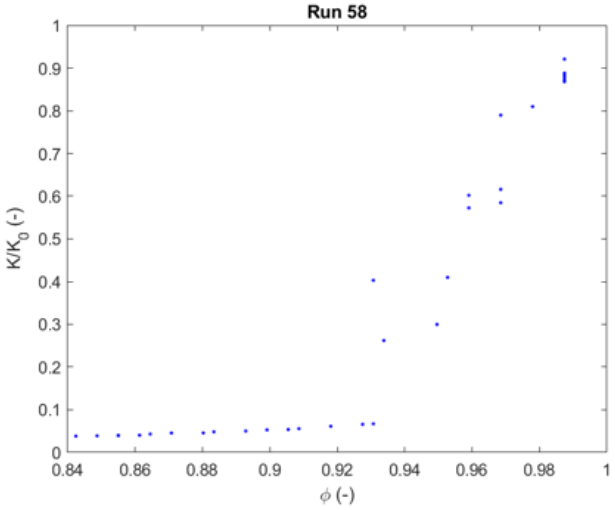
Run 58
K/K0 (-)
ϕ (-)

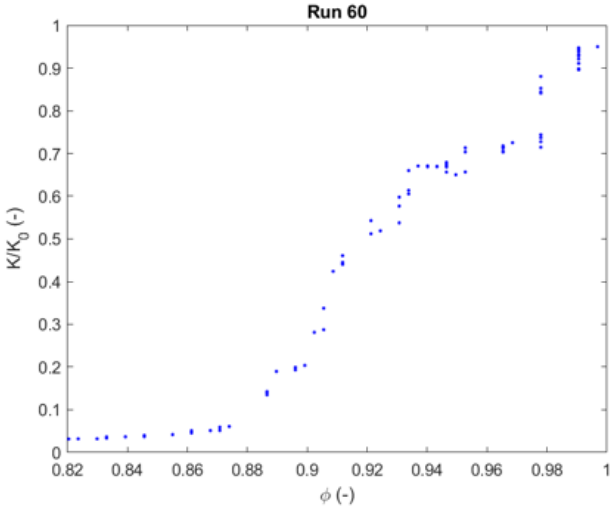
Run 60
K/K0 (-)
ϕ (-)

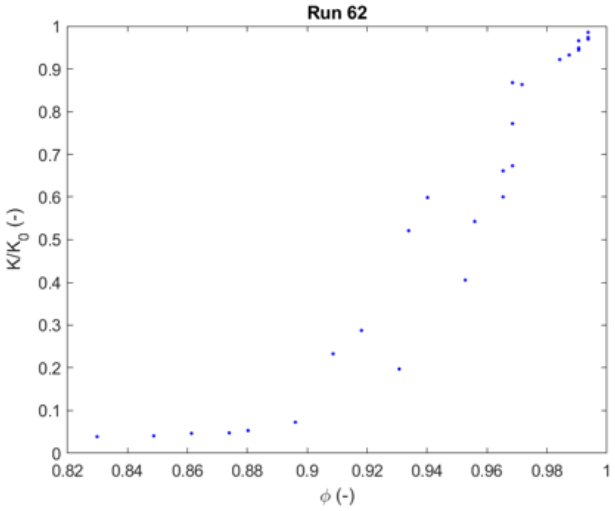
Run 62
K/K0 (-)
ϕ (-)

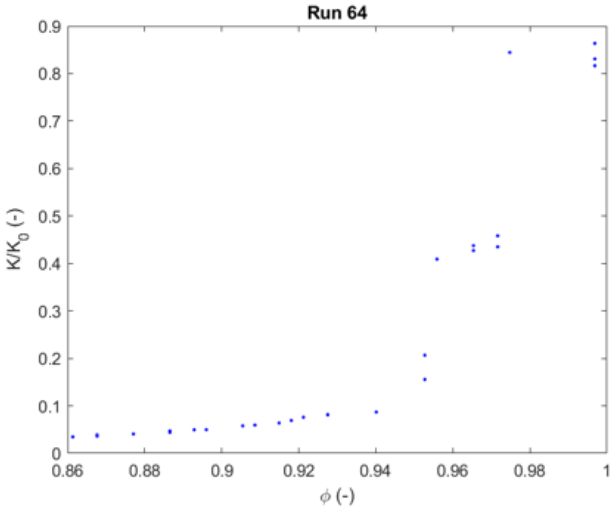
Run 64
K/K0 (-)
ϕ (-)

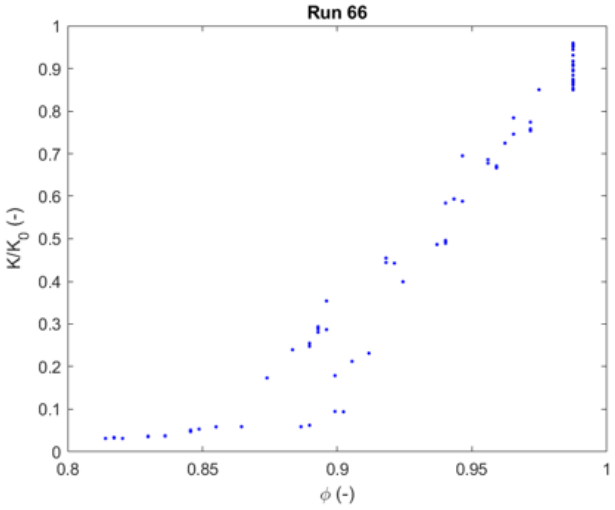
Run 66
K/K0 (-)
ϕ (-)

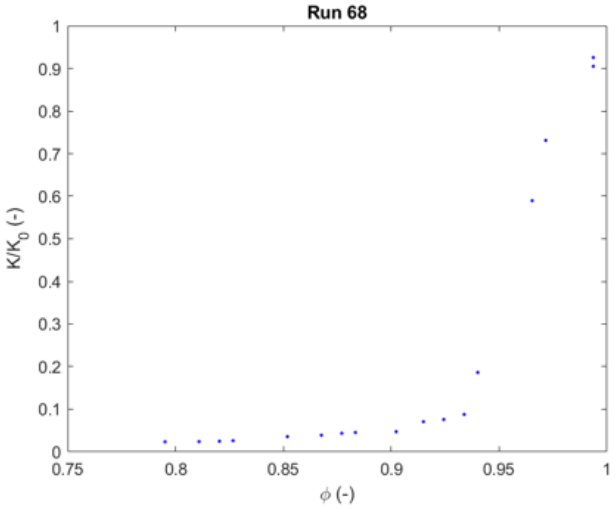
Run 68
K/K0 (-)
ϕ (-)

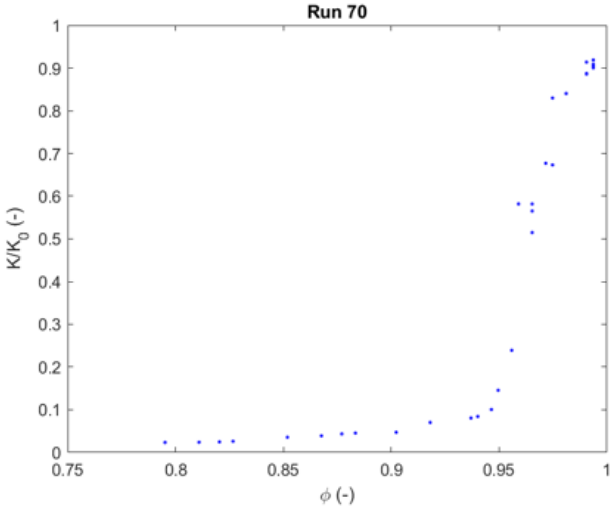
Run 70
K/K0 (-)
ϕ (-)

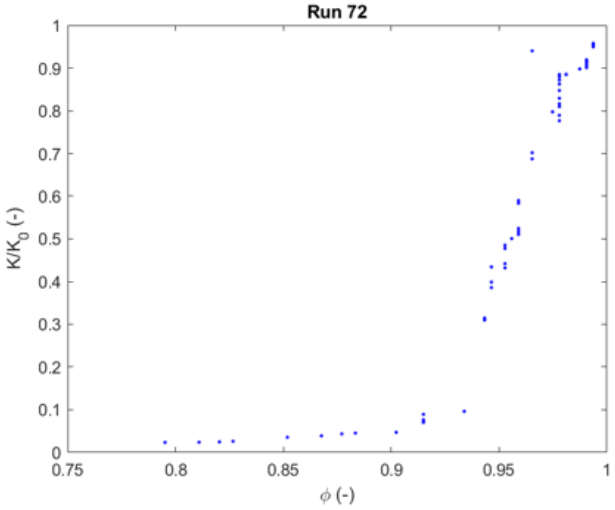
Run 72
K/K0 (-)
ϕ (-)

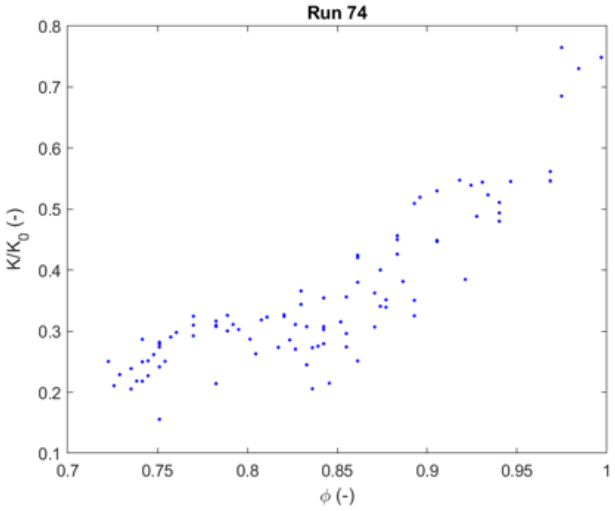
Run 74
K/K0 (-)
ϕ (-)

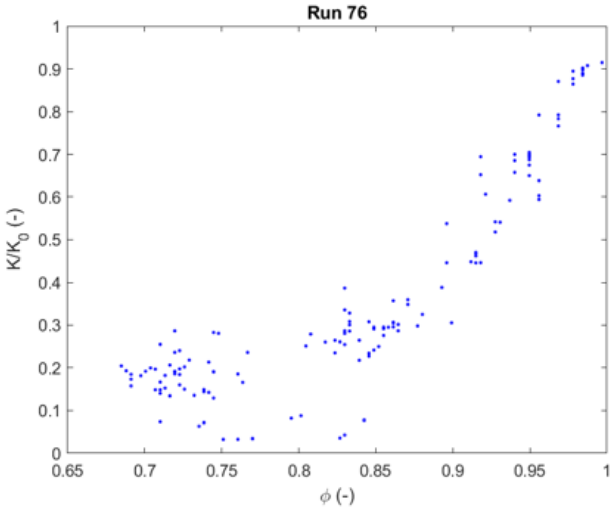
Run 76
K/K0 (-)
ϕ (-)

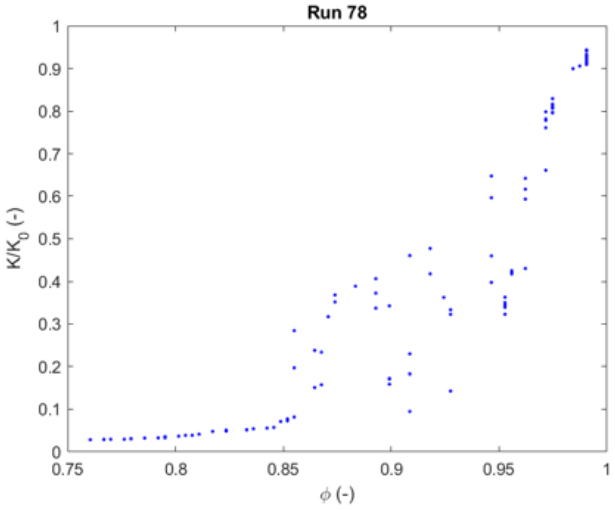
Run 78
K/K0 (-)
ϕ (-)

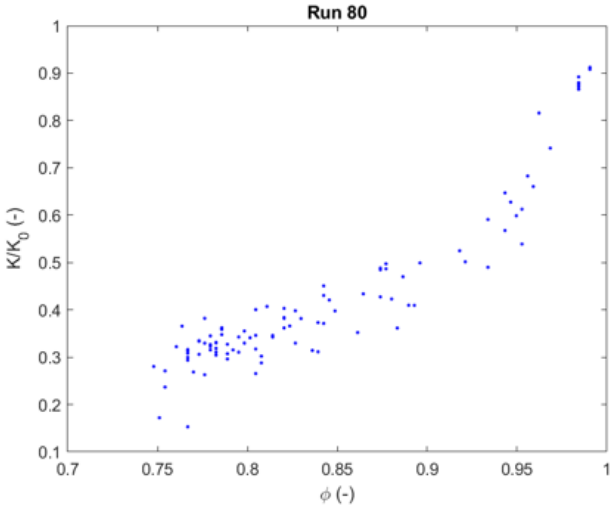
Run 80
K/K0 (-)
ϕ (-)

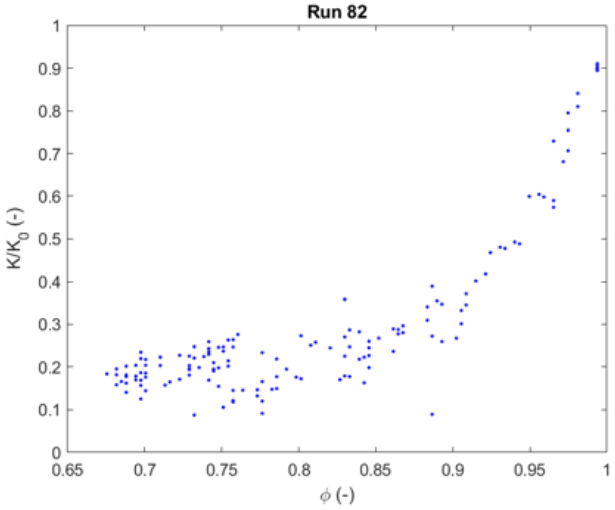
Run 82
K/K0 (-)
ϕ (-)

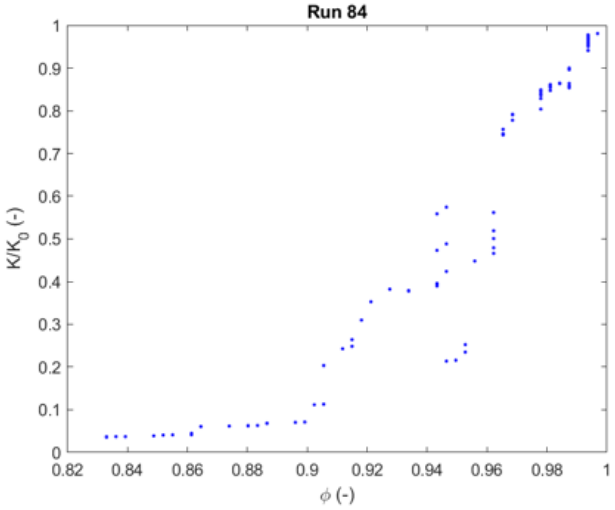
Run 84
K/K0 (-)
ϕ (-)

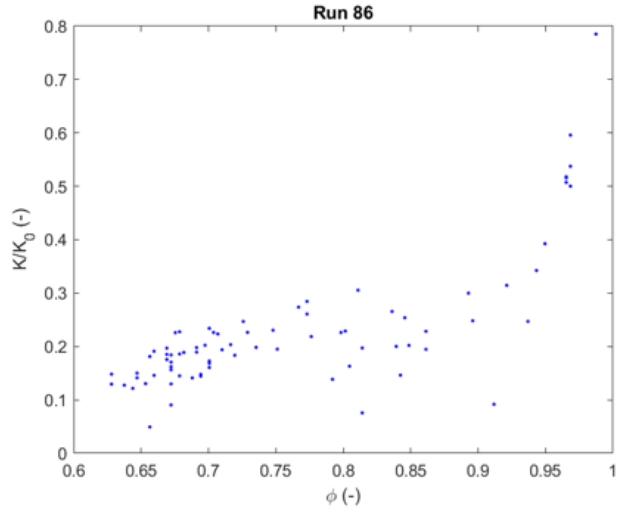
Run 86
K/K0 (-)
ϕ (-)

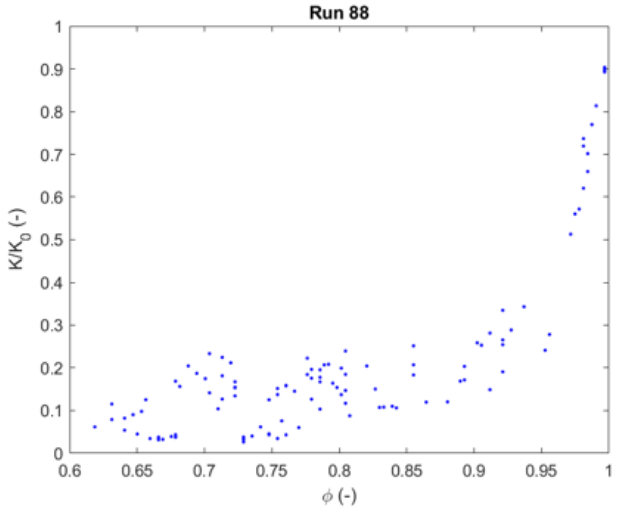
Run 88
K/K0 (-)
ϕ (-)

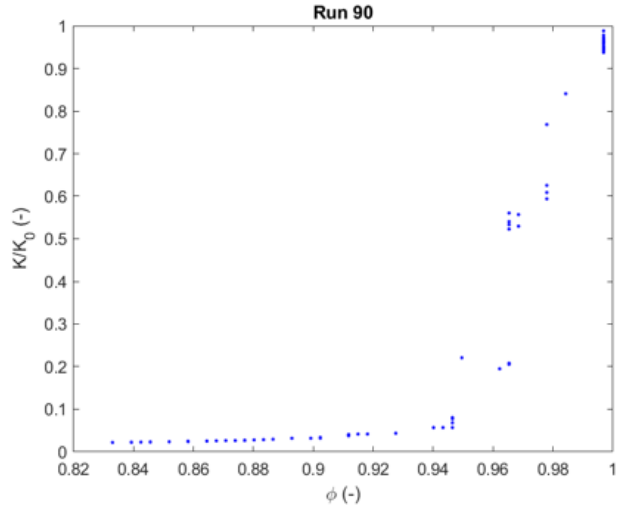
Run 90
K/K0 (-)
ϕ (-)

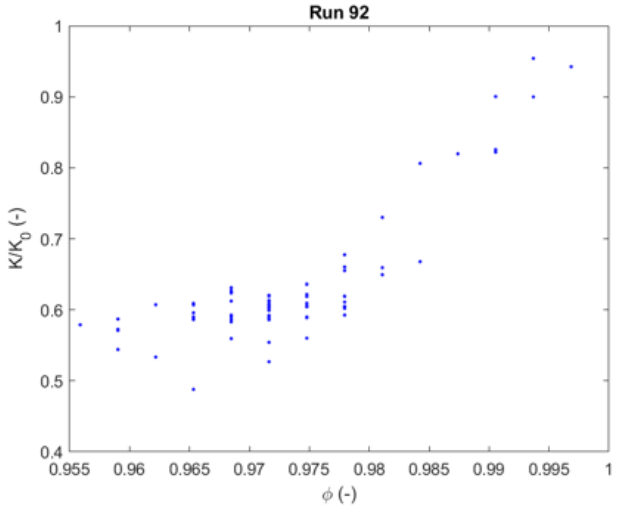
Run 92
K/K0 (-)
ϕ (-)

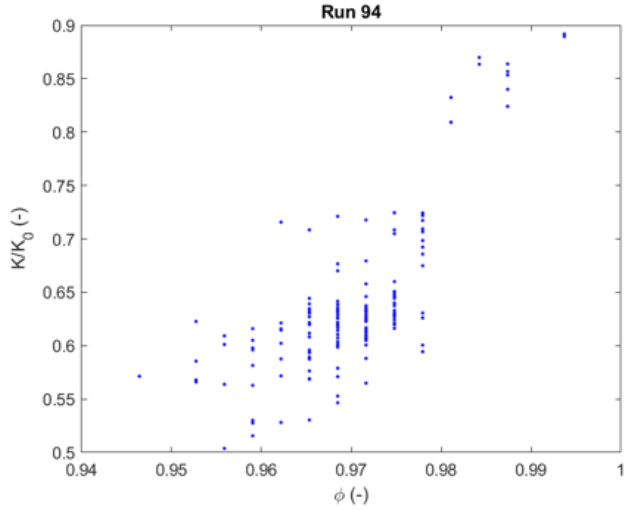
Run 94
K/K0 (-)
ϕ (-)

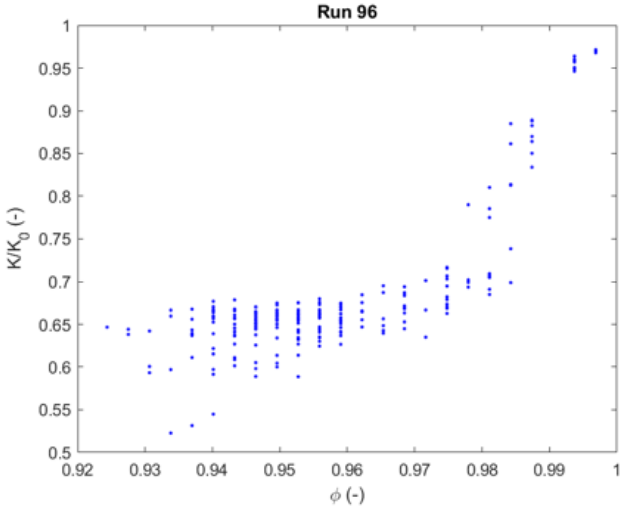
Run 96
K/K0 (-)
ϕ (-)

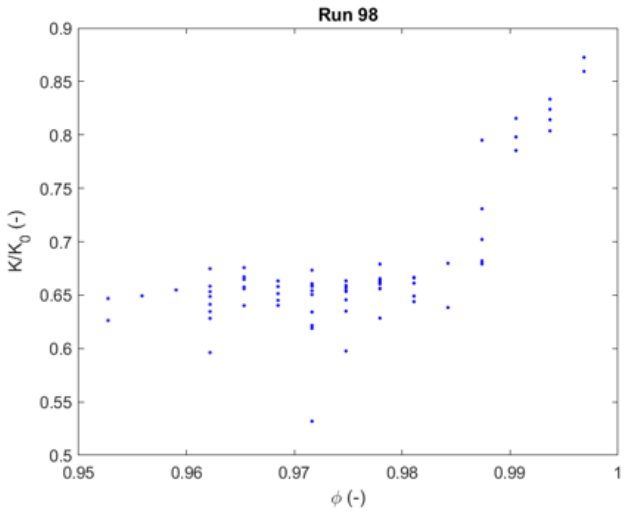
Run 98
K/K0 (-)
ϕ (-)

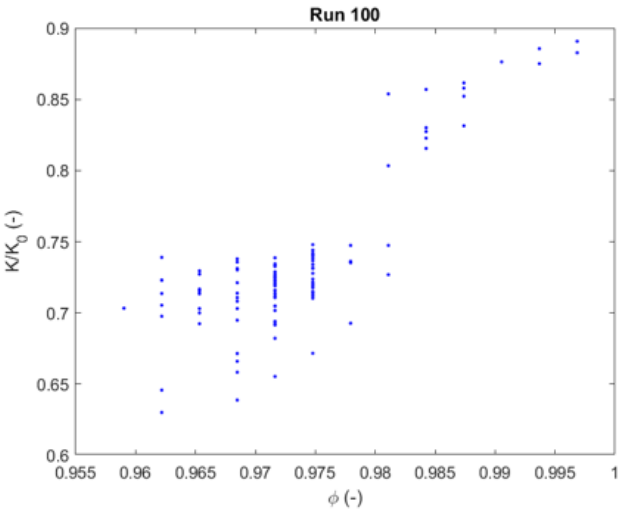
Run 100
K/K0 (-)
ϕ (-)

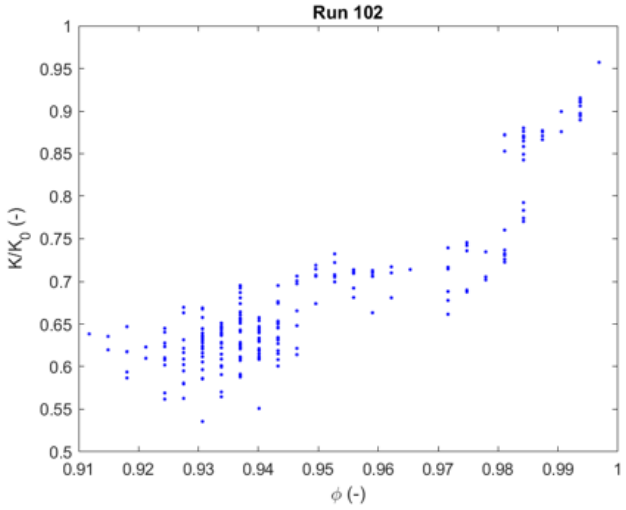
Run 102
K/K0 (-)
ϕ (-)

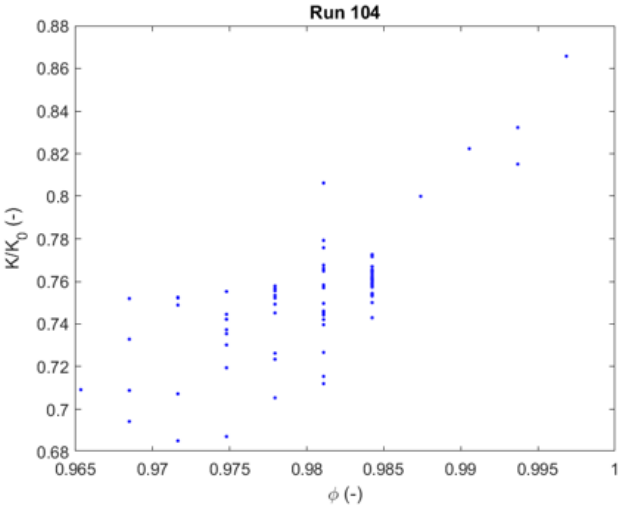
Run 104
K/K0 (-)
ϕ (-)

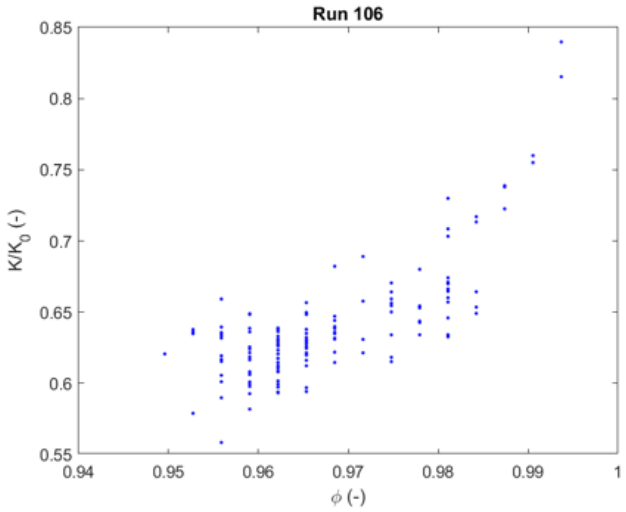
Run 106
K/K0 (-)
ϕ (-)

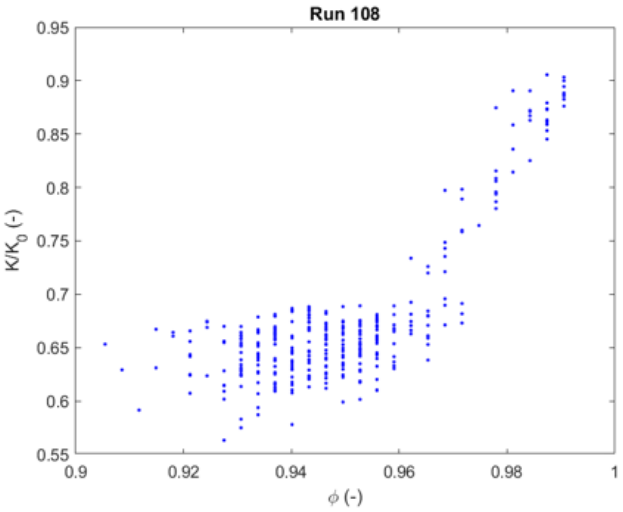
Run 108
K/K0 (-)
ϕ (-)

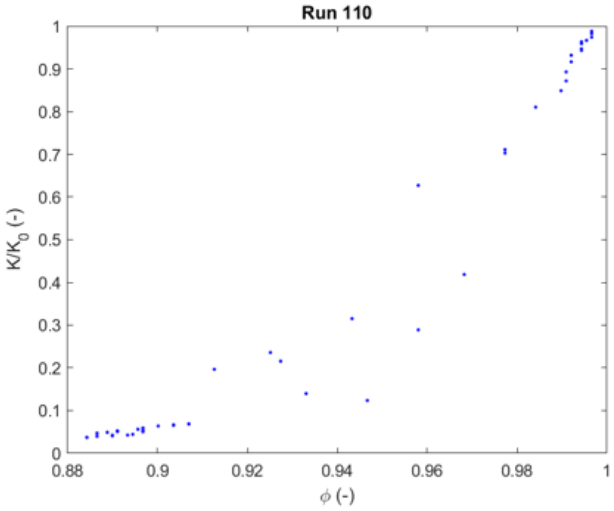
Run 110
K/K0 (-)
ϕ (-)

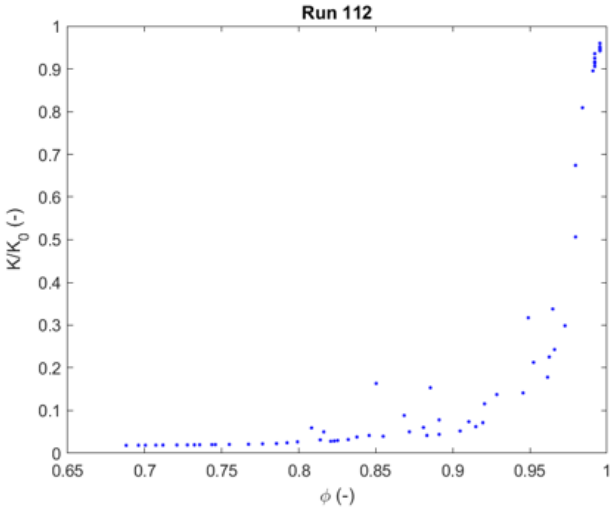
Run 112
K/K0 (-)
ϕ (-)

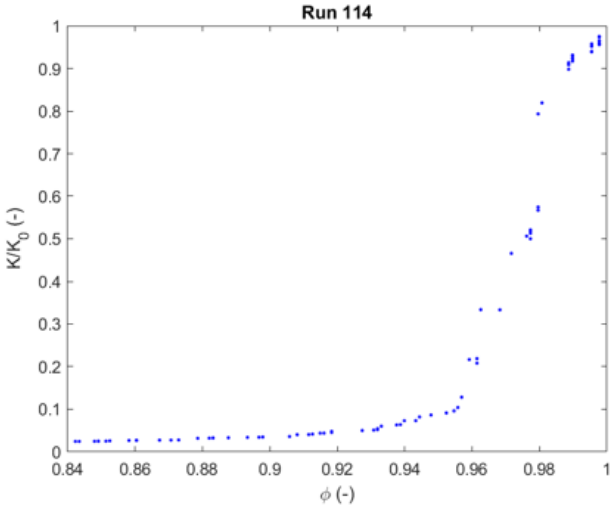
Run 114
K/K0 (-)
ϕ (-)

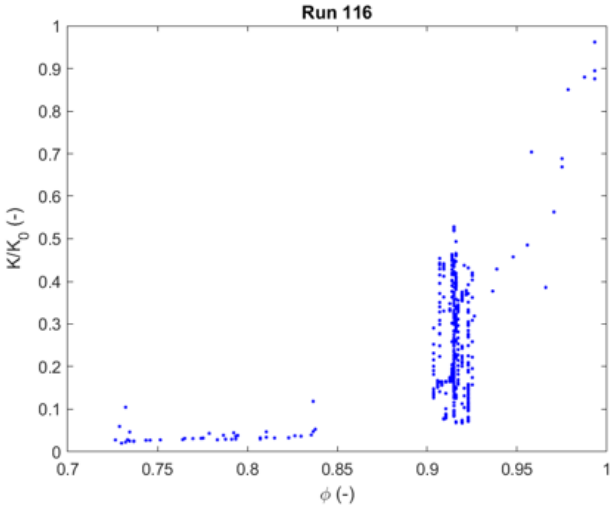
Run 116
K/K0 (-)
ϕ (-)

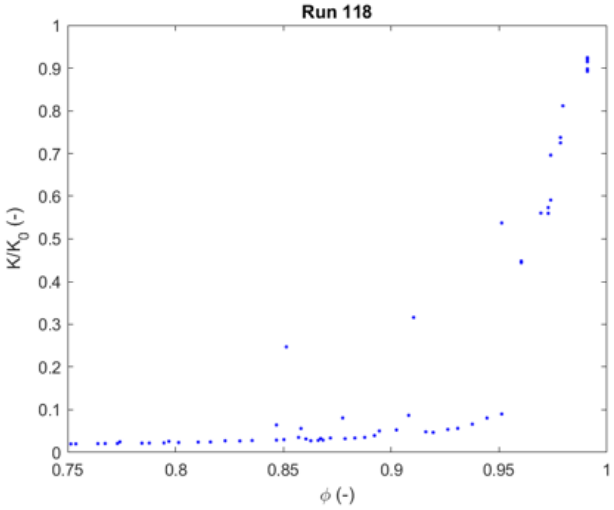
Run 118
K/K0 (-)
ϕ (-)

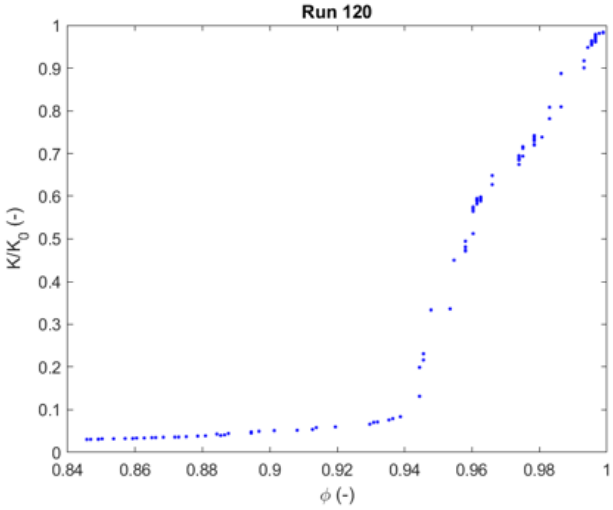
Run 120
K/K0 (-)
ϕ (-)

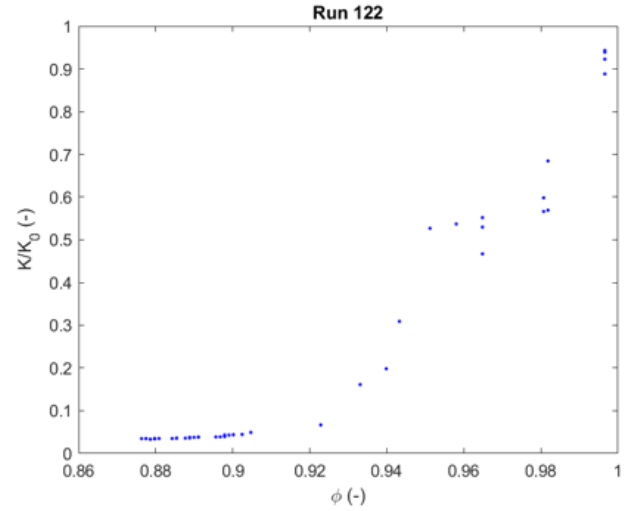
Run 122
K/K0 (-)
ϕ (-)

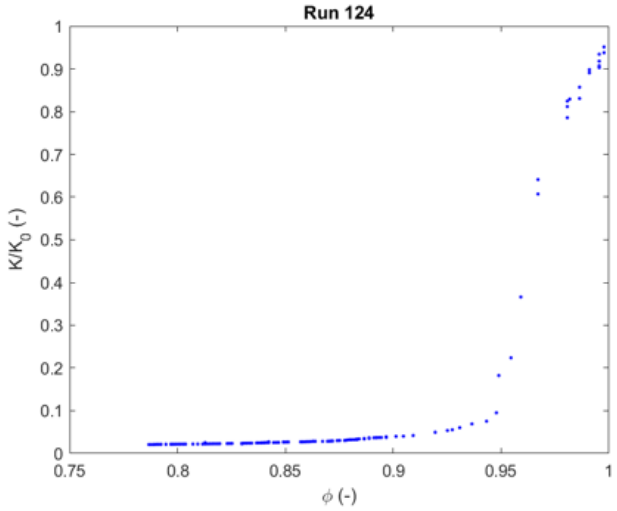
Run 124
K/K0 (-)
ϕ (-)

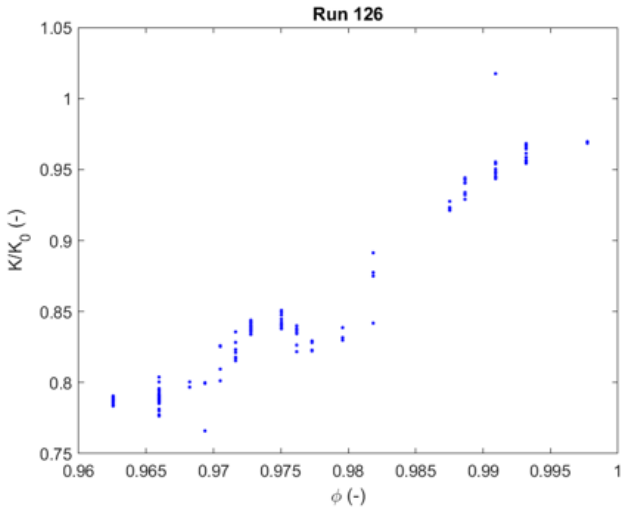
Run 126
K/K0 (-)
ϕ (-)

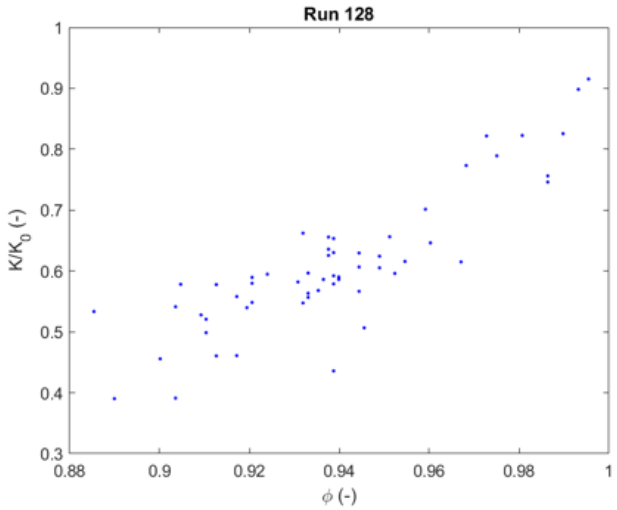
Run 128
K/K0 (-)
ϕ (-)

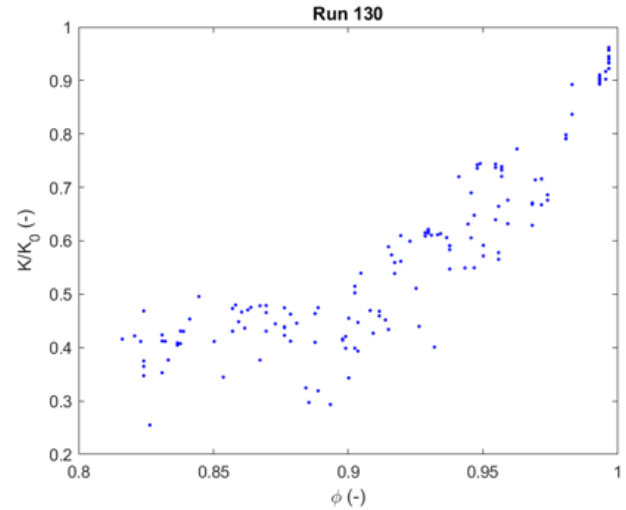
Run 130
K/K0 (-)
ϕ (-)

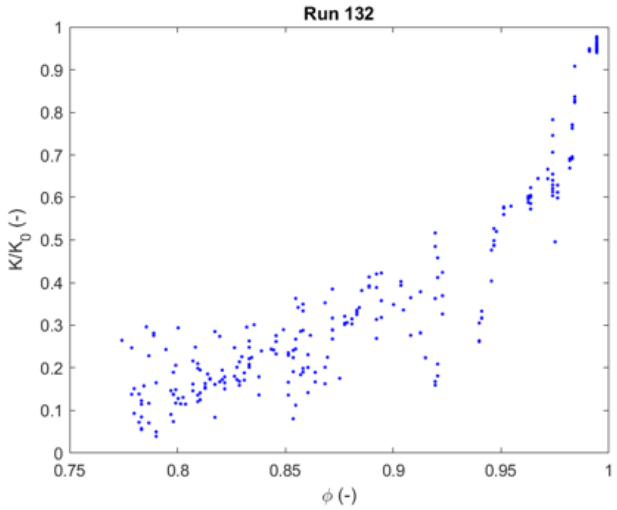
Run 132
K/K0 (-)
ϕ (-)

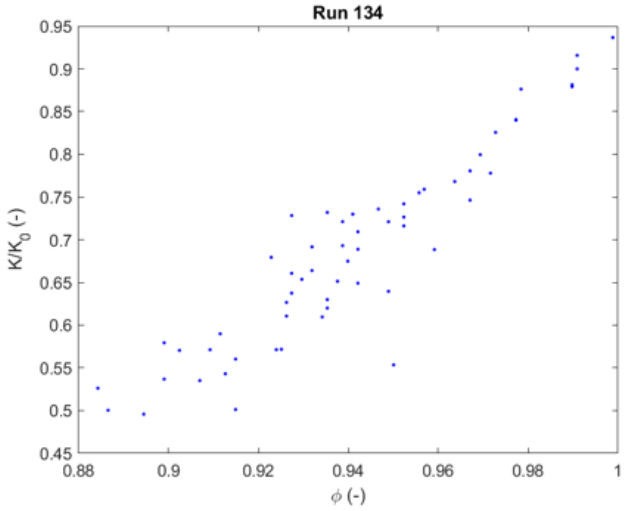
Run 134
K/K0 (-)
ϕ (-)

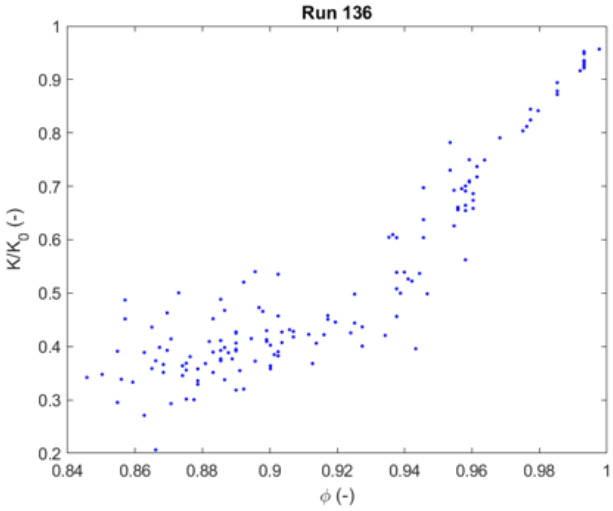
Run 136
K/K0 (-)
ϕ (-)

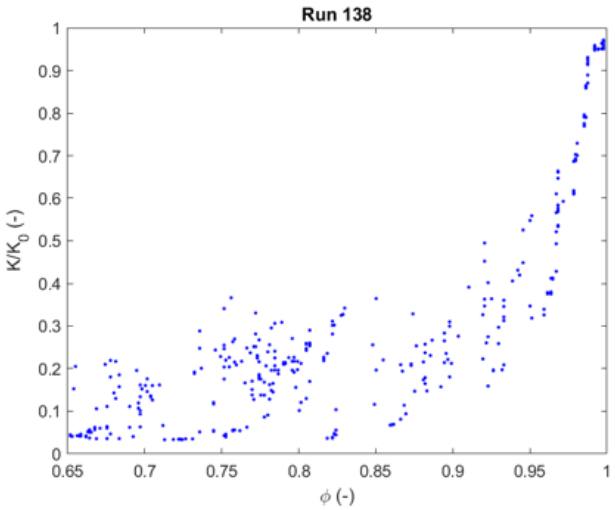
Run 138
K/K0 (-)
ϕ (-)

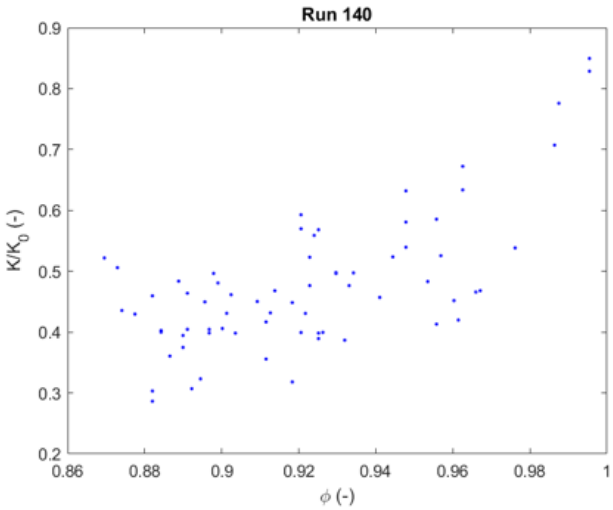
Run 140
K/K0 (-)
ϕ (-)

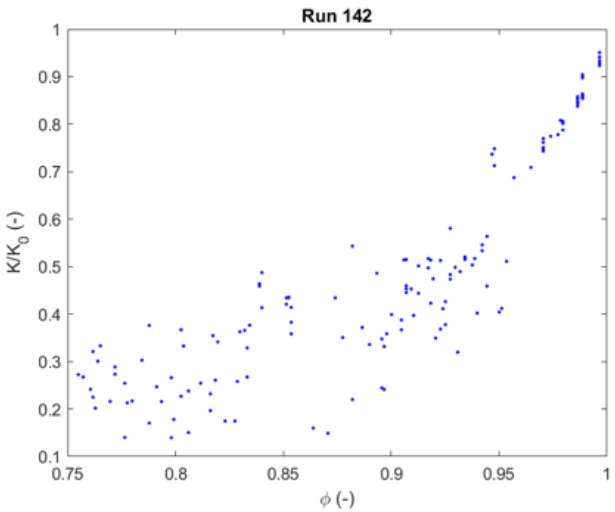
Run 142
K/K0 (-)
ϕ (-)

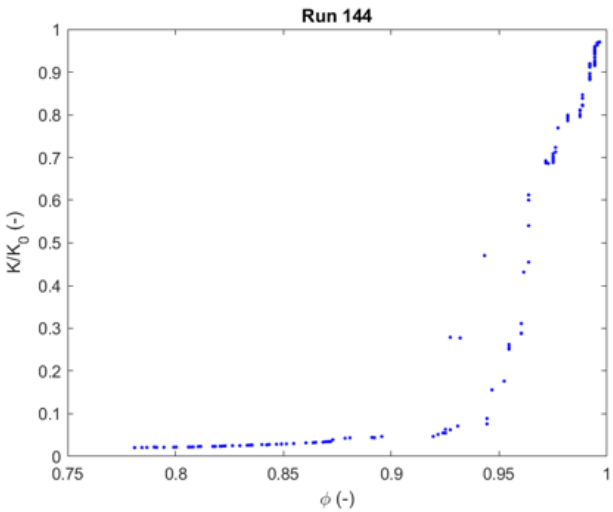
Run 144
K/K0 (-)
ϕ (-)

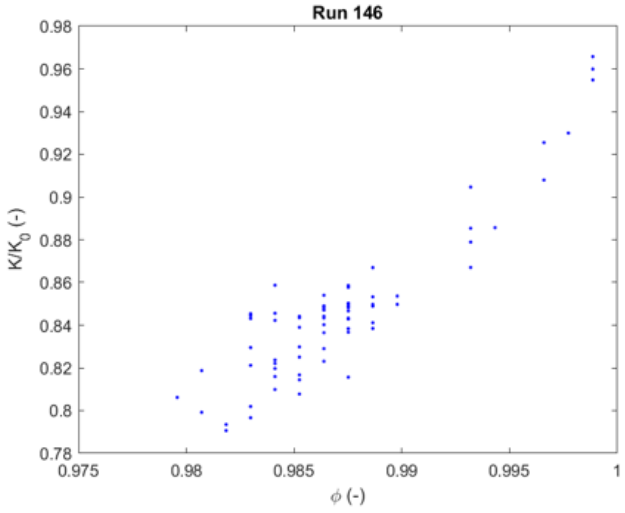
Run 146
K/K0 (-)
ϕ (-)

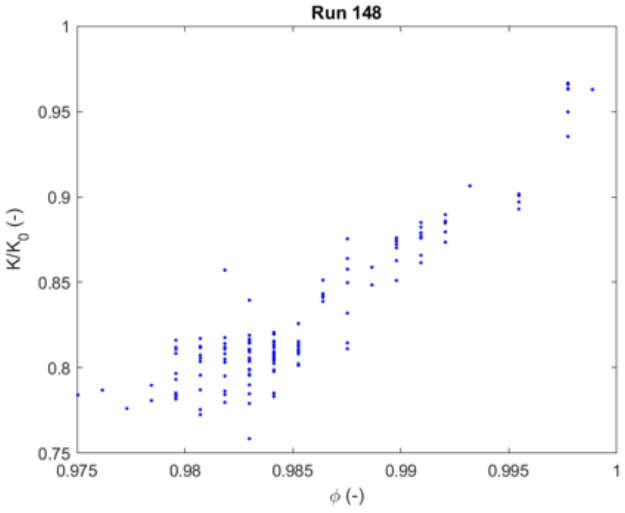
Run 148
K/K0 (-)
ϕ (-)

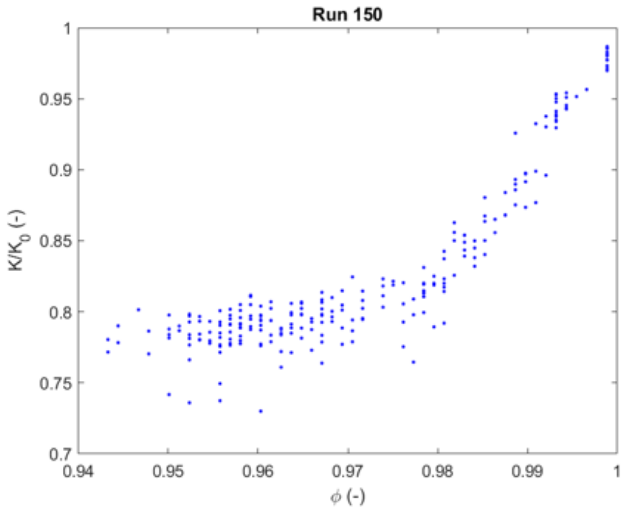
Run 150
K/K0 (-)
ϕ (-)

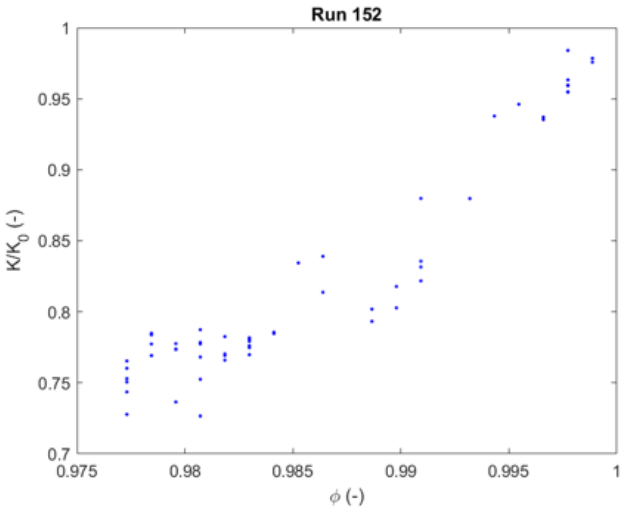
Run 152
K/K0 (-)
ϕ (-)

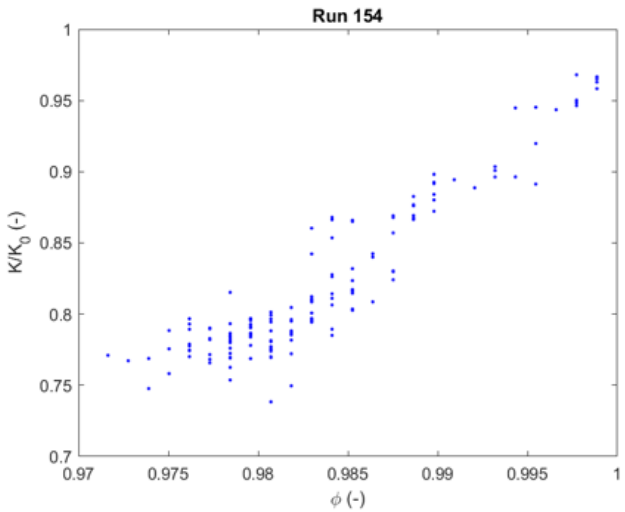
Run 154
K/K0 (-)
ϕ (-)

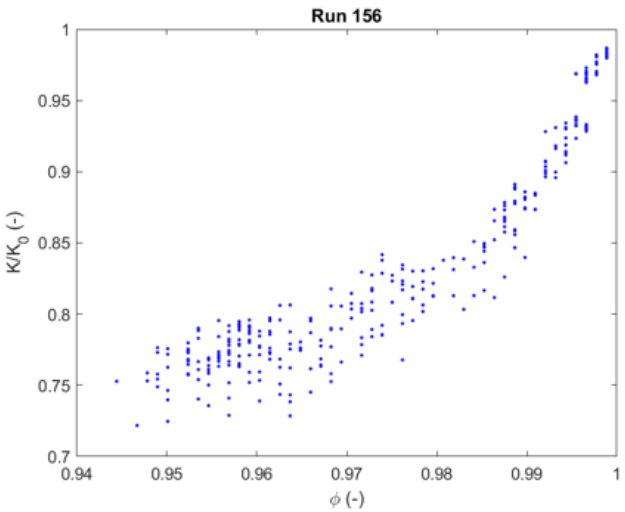
Run 156
K/K0 (-)
ϕ (-)

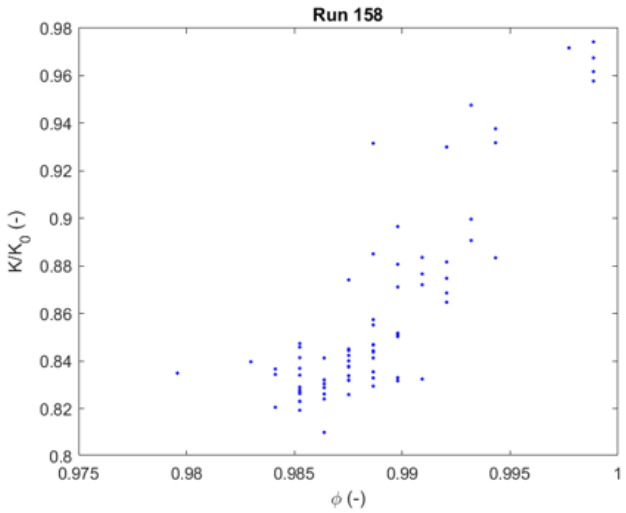
Run 158
K/K0 (-)
ϕ (-)
0.98
0.96
0.94
0.92
0.9
0.88
0.86
0.84
0.82
0.8
0.975
0.98
0.985
0.99
0.995
1

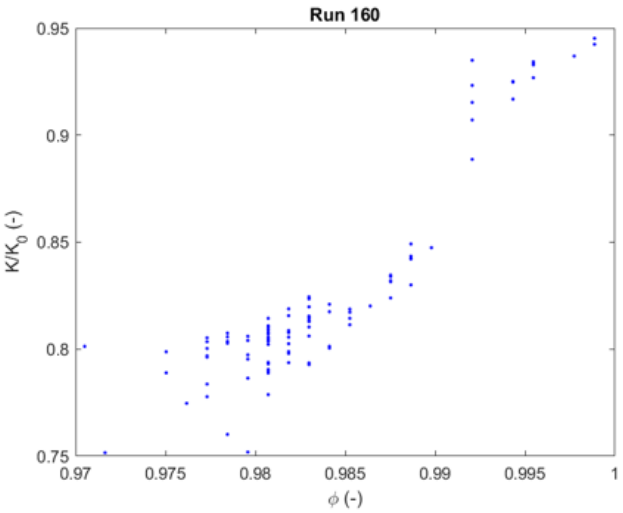
Run 160
K/K0 (-)
ϕ (-)
0.95
0.9
0.85
0.8
0.75
0.97
0.975
0.98
0.985
0.99
0.995
1

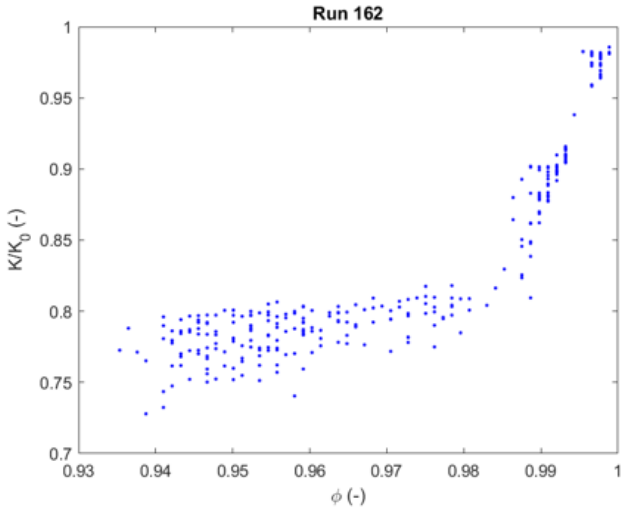
Run 162
K/K0 (-)
ϕ (-)
1
0.95
0.9
0.85
0.8
0.75
0.7
0.93
0.94
0.95
0.96
0.97
0.98
0.99
1

Appendix B

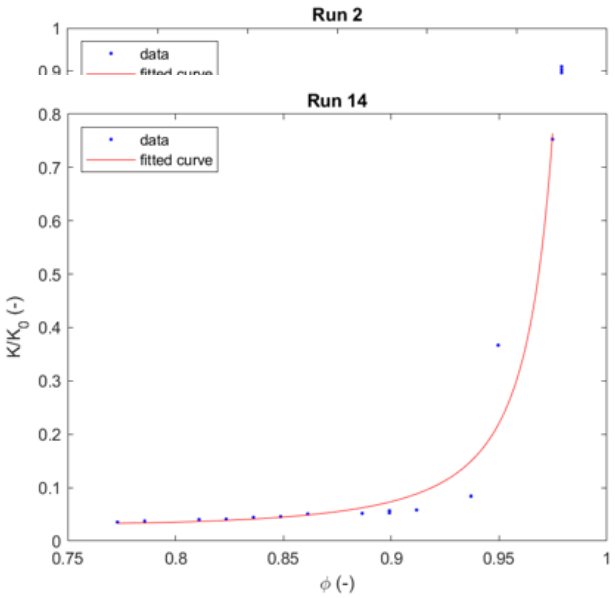
Run 2
data
fitted curve
K/K0 (-)
ϕ (-)

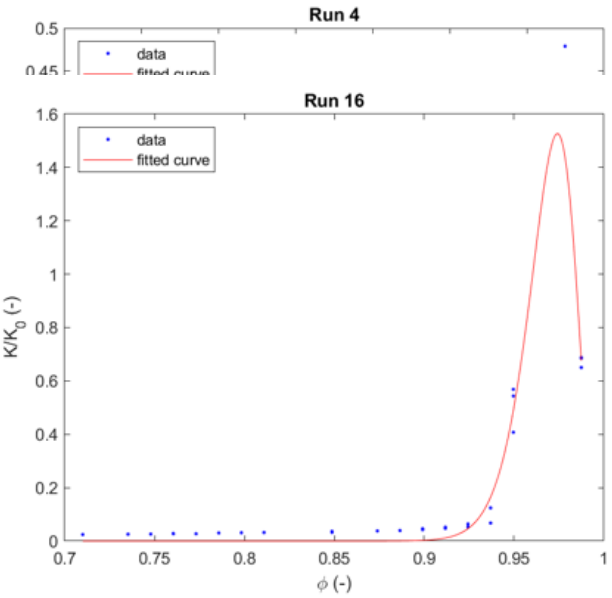
Run 4
data
fitted curve
K/K0 (-)
ϕ (-)

Run 14
data
fitted curve
K/K0 (-)
ϕ (-)

Run 16
data
fitted curve
K/K0 (-)
ϕ (-)

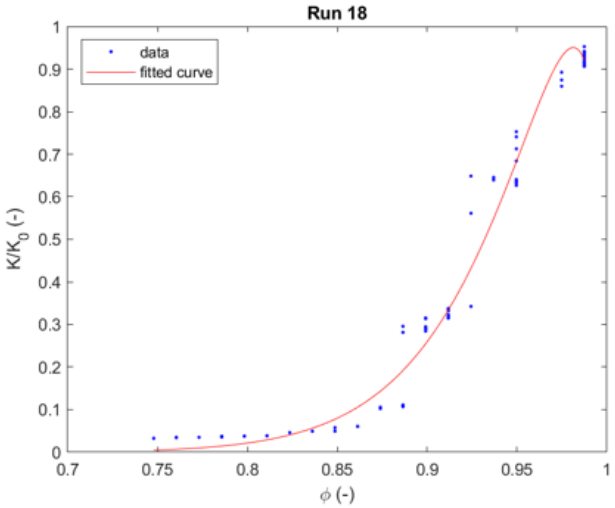
Run 18
data
fitted curve
K/K0 (-)
ϕ (-)

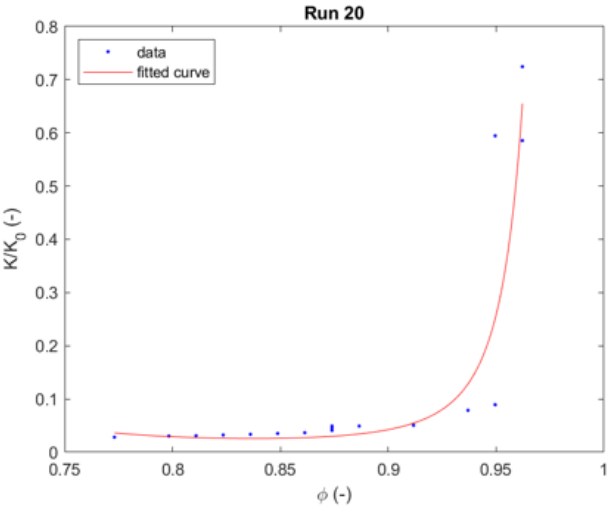
Run 20
data
fitted curve
K/K0 (-)
ϕ (-)

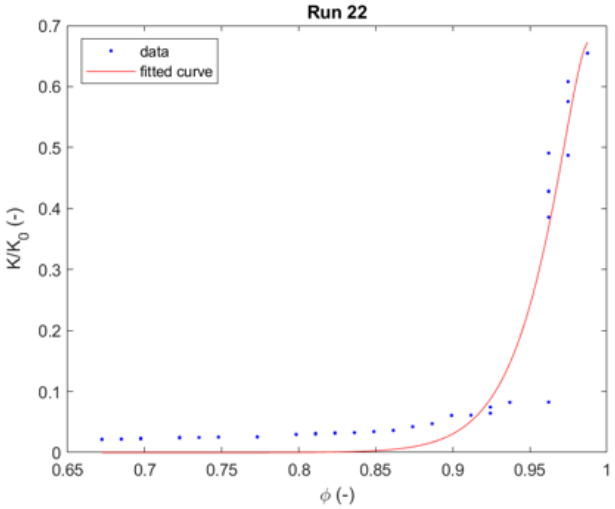
Run 22
data
fitted curve
K/K0 (-)
ϕ (-)

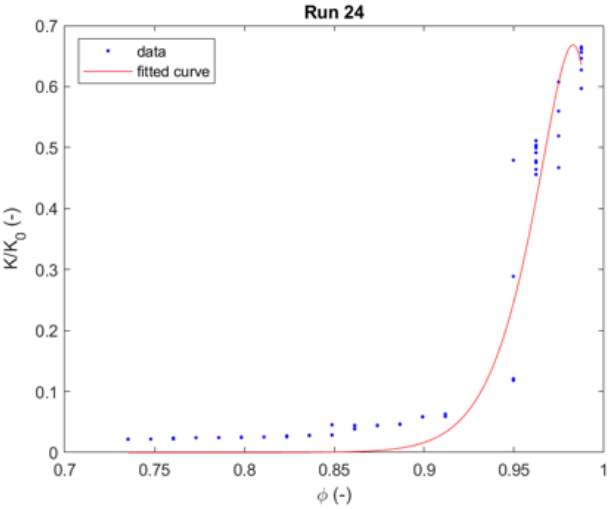
Run 24
data
fitted curve
K/K0 (-)
ϕ (-)

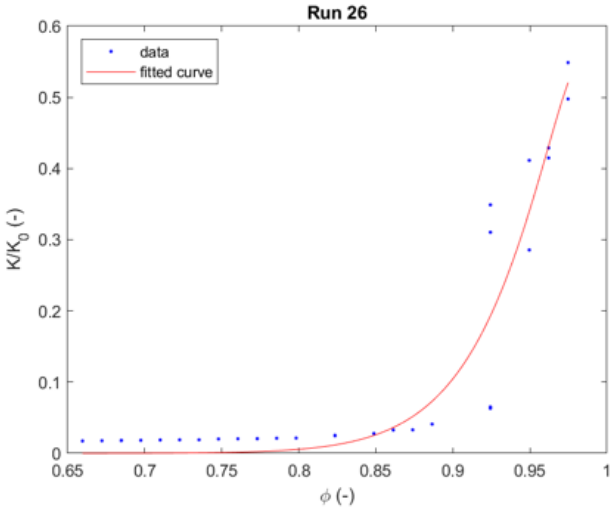
Run 26
data
fitted curve
K/K0 (-)
ϕ (-)

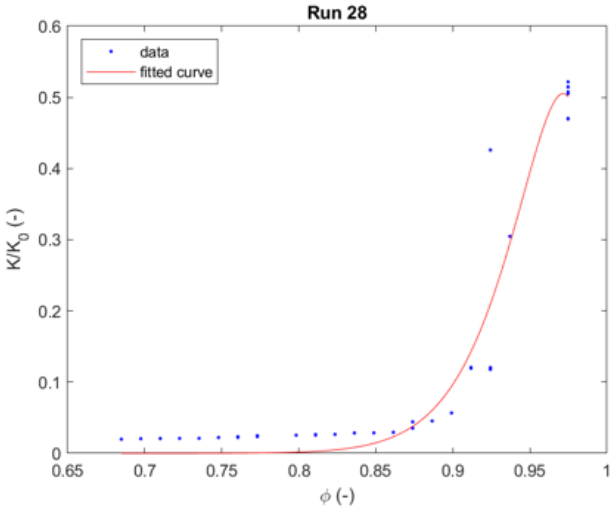
Run 28
data
fitted curve
K/K0 (-)
ϕ (-)

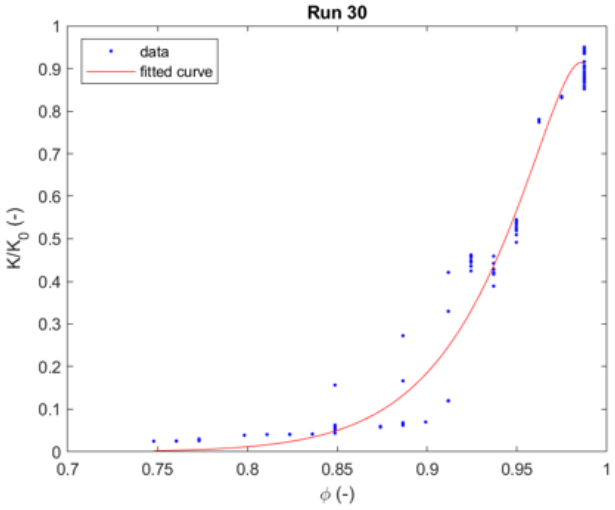
Run 30
data
fitted curve
K/K0 (-)
ϕ (-)

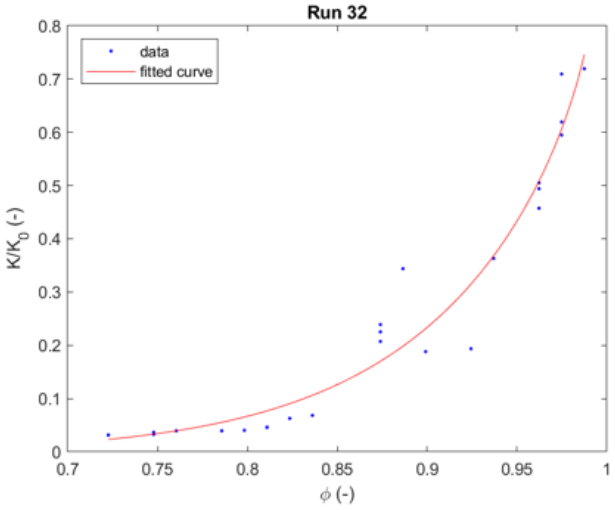
Run 32
data
fitted curve
K/K0 (-)
ϕ (-)

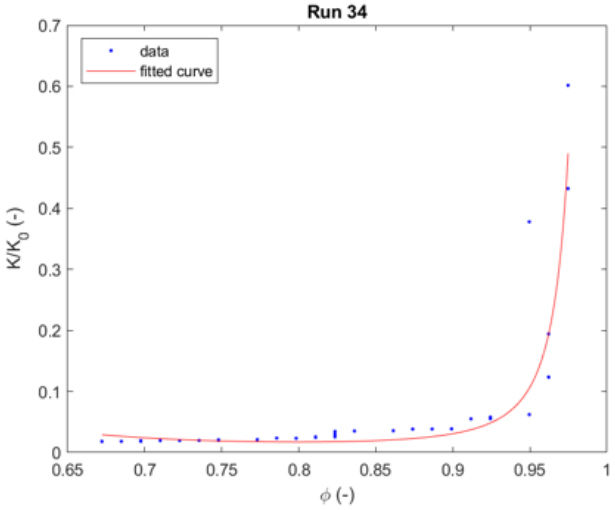
Run 34
data
fitted curve
K/K0 (-)
ϕ (-)

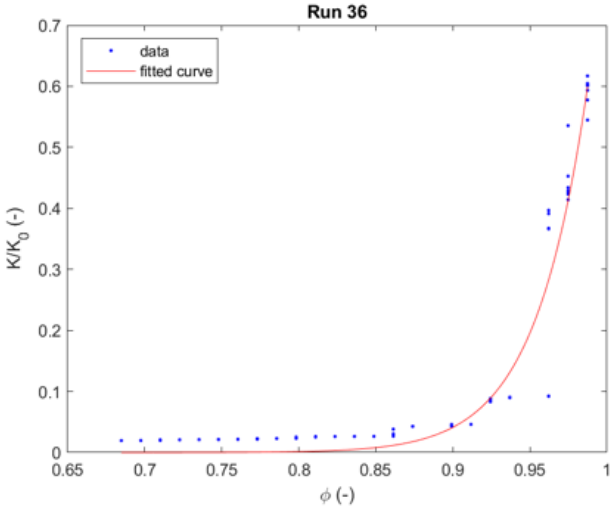
Run 36
data
fitted curve
K/K0 (-)
ϕ (-)

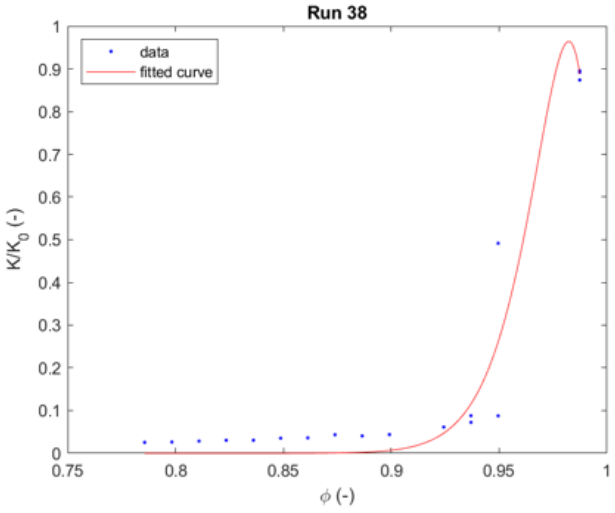
Run 38
data
fitted curve
K/K0 (-)
ϕ (-)

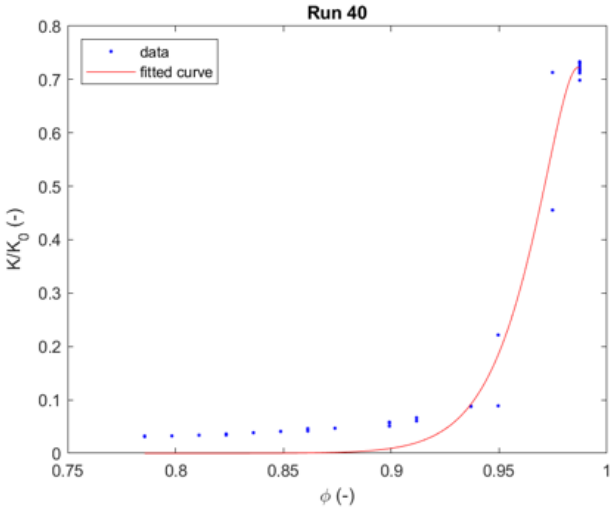
Run 40
data
fitted curve
K/K0 (-)
ϕ (-)

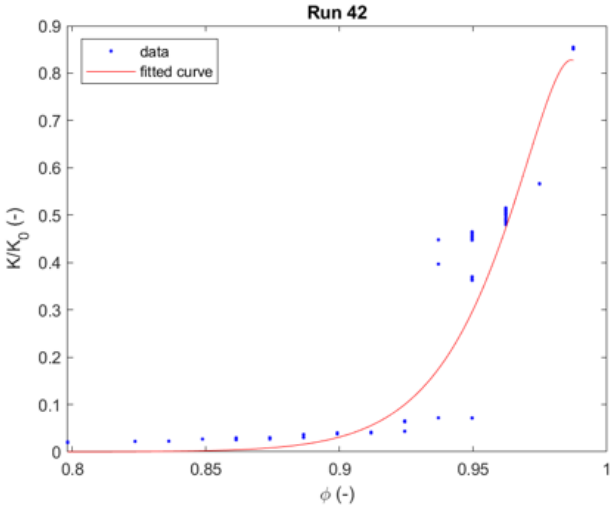
Run 42
data
fitted curve
K/K0 (-)
ϕ (-)

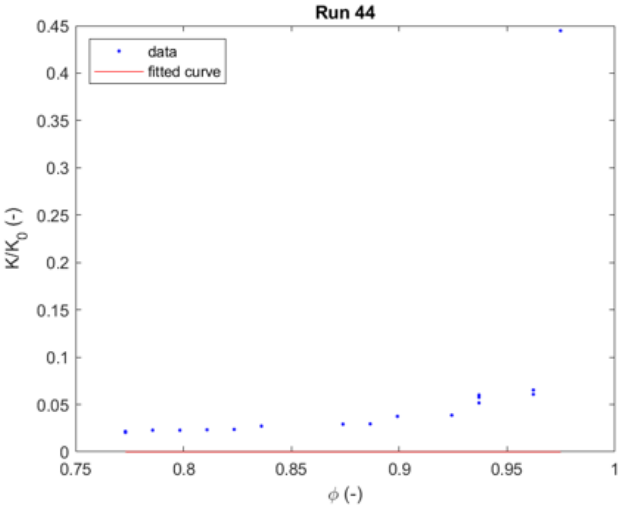
Run 44
data
fitted curve
K/K0 (-)
ϕ (-)

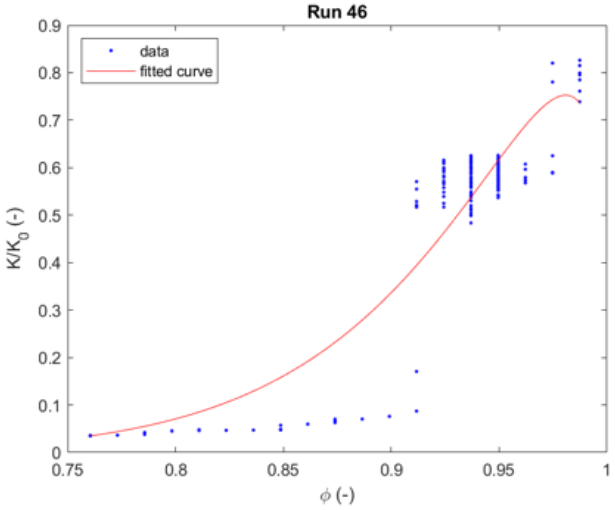
Run 46
data
fitted curve
K/K0 (-)
ϕ (-)

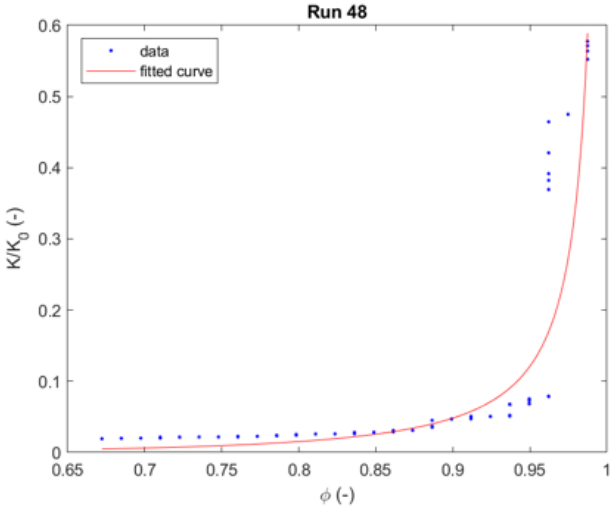
Run 48
data
fitted curve
K/K0 (-)
ϕ (-)

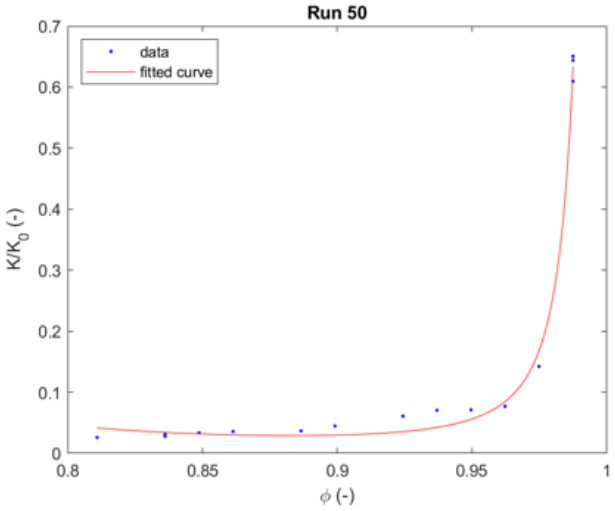
Run 50
data
fitted curve
K/K0 (-)
ϕ (-)

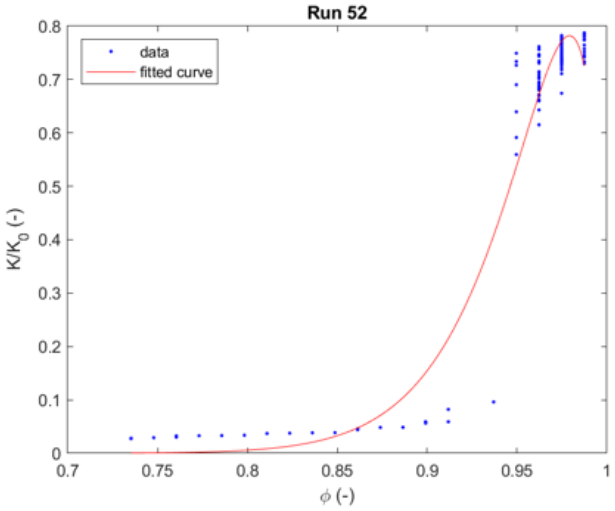
Run 52
data
fitted curve
K/K0 (-)
ϕ (-)

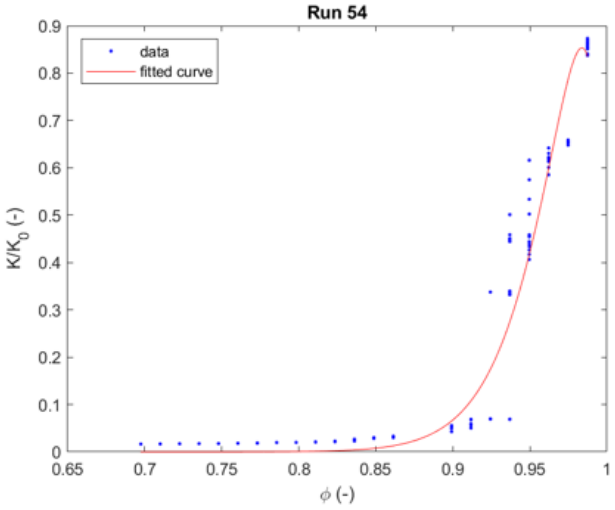
Run 54
data
fitted curve
K/K0 (-)
ϕ (-)

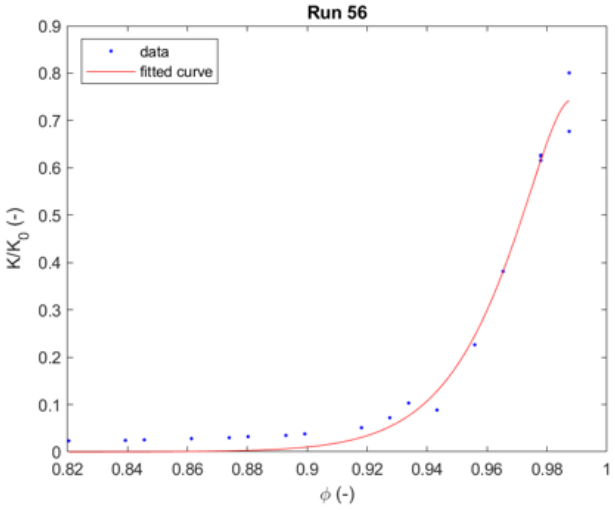
Run 56
data
fitted curve
K/K0 (-)
ϕ (-)

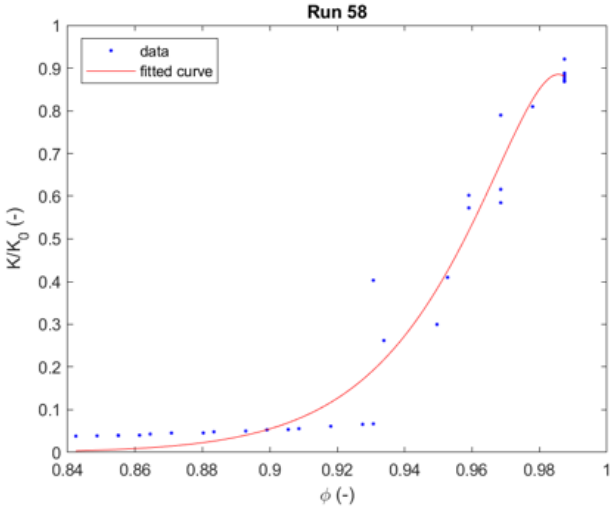
Run 58
data
fitted curve
K/K0 (-)
ϕ (-)

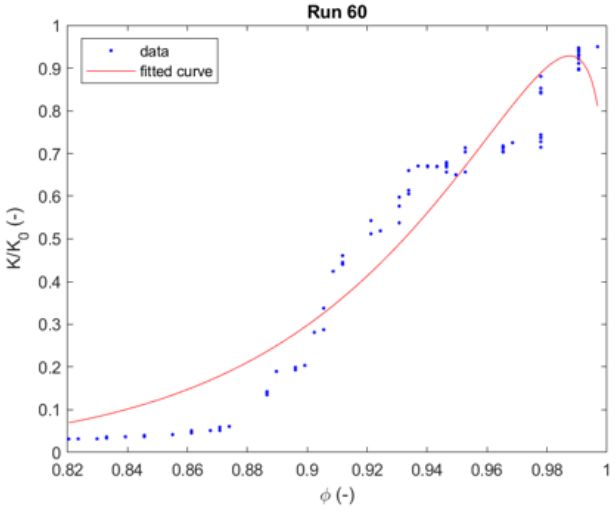
Run 60
data
fitted curve
K/K0 (-)
ϕ (-)

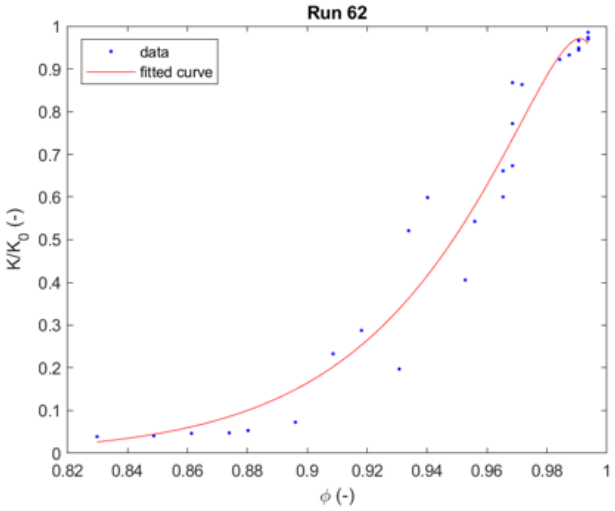
Run 62
data
fitted curve
K/K0 (-)
ϕ (-)

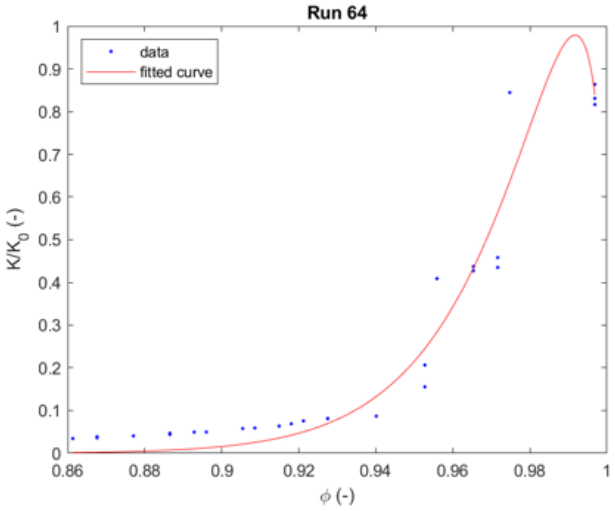
Run 64
data
fitted curve
K/K0 (-)
ϕ (-)

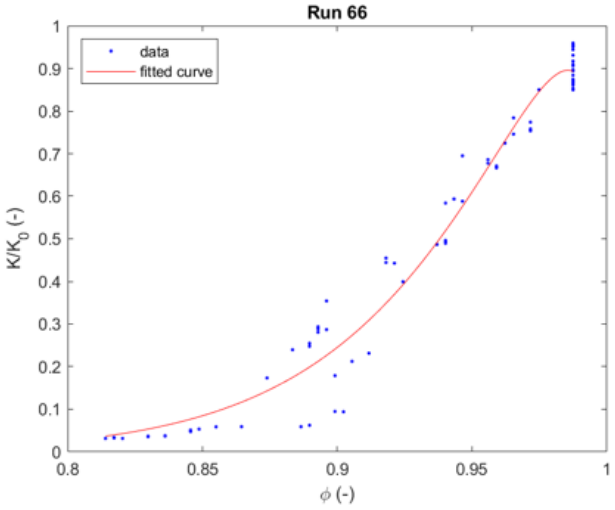
Run 66
data
fitted curve
K/K0 (-)
ϕ (-)

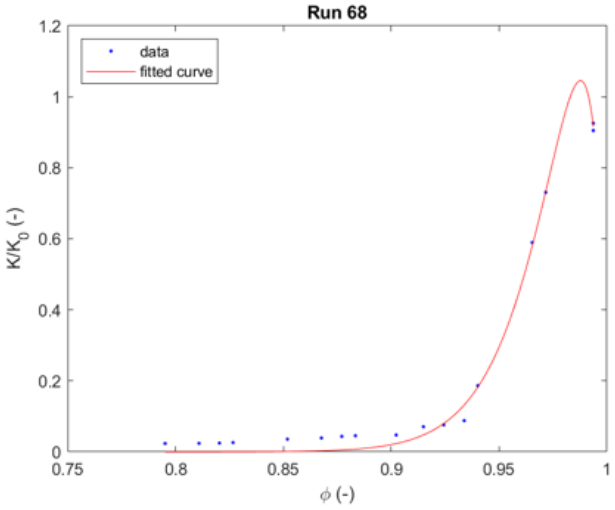
Run 68
data
fitted curve
K/K0 (-)
ϕ (-)

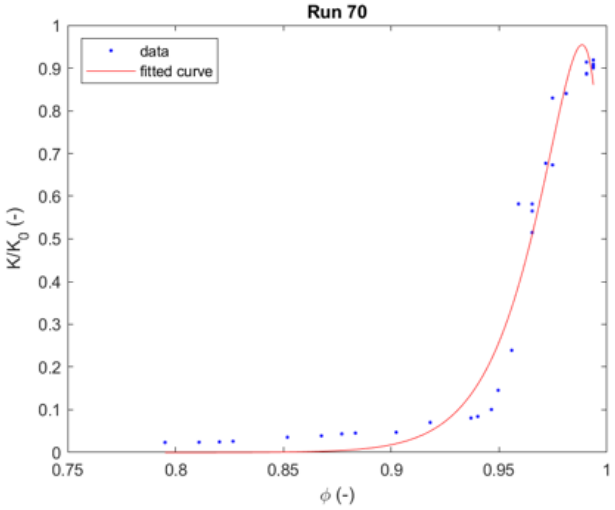
Run 70
data
fitted curve
K/K0 (-)
ϕ (-)

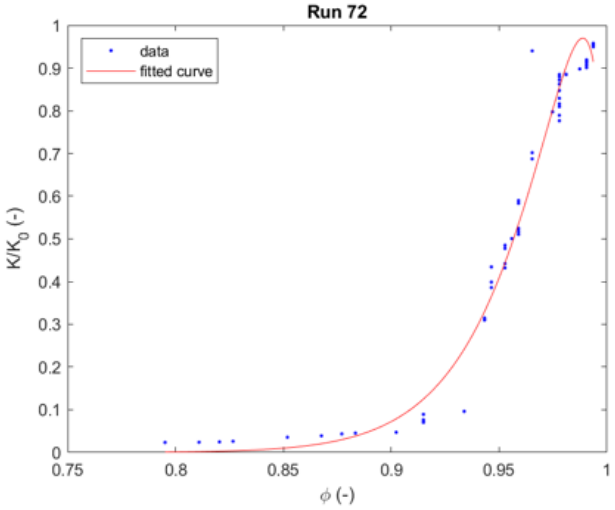
Run 72
data
fitted curve
K/K0 (-)
ϕ (-)

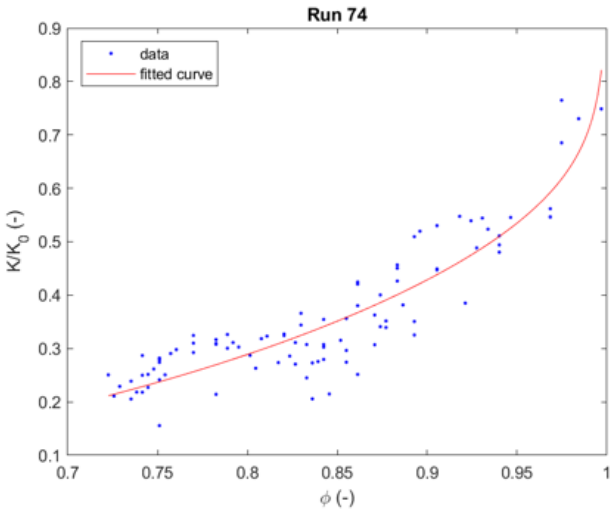
Run 74
data
fitted curve
K/K0 (-)
ϕ (-)

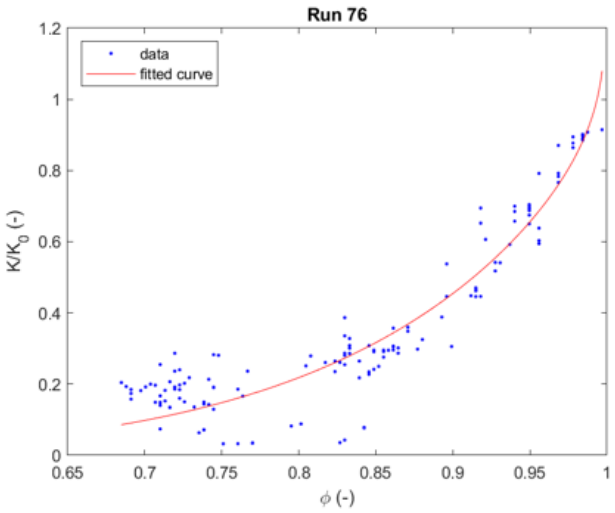
Run 76
data
fitted curve
K/K0 (-)
ϕ (-)

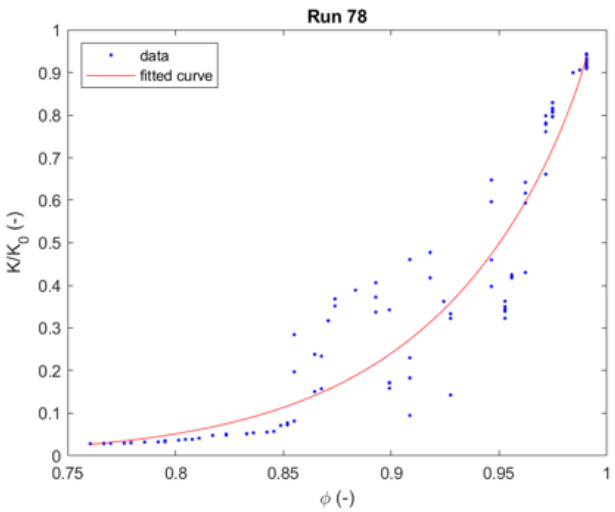
Run 78
data
fitted curve
K/K0 (-)
ϕ (-)

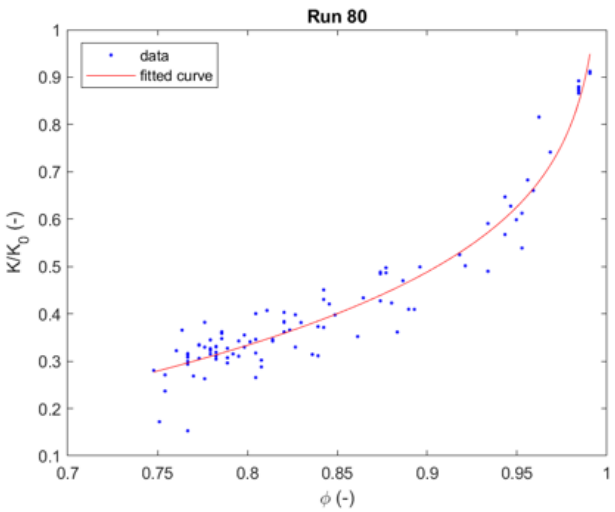
Run 80
data
fitted curve
K/K0 (-)
ϕ (-)

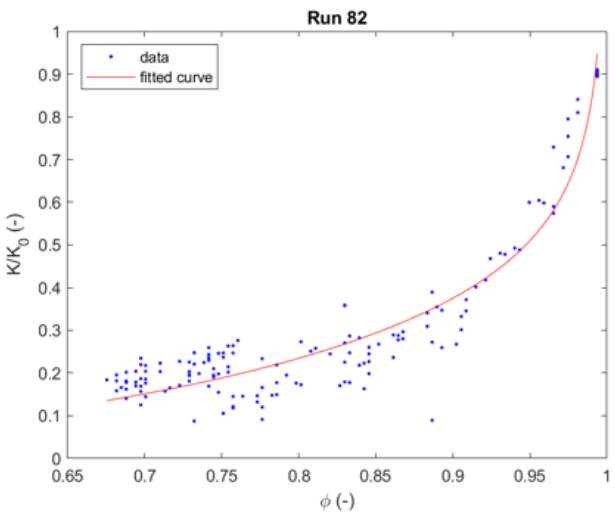
Run 82
data
fitted curve
K/K0 (-)
ϕ (-)

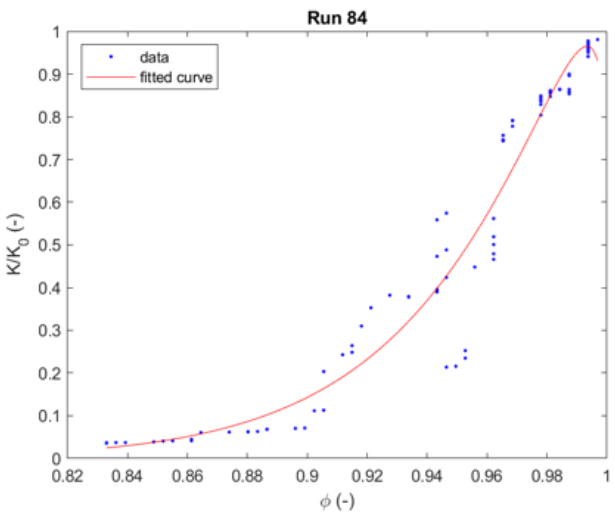
Run 84
data
fitted curve
K/K0 (-)
ϕ (-)

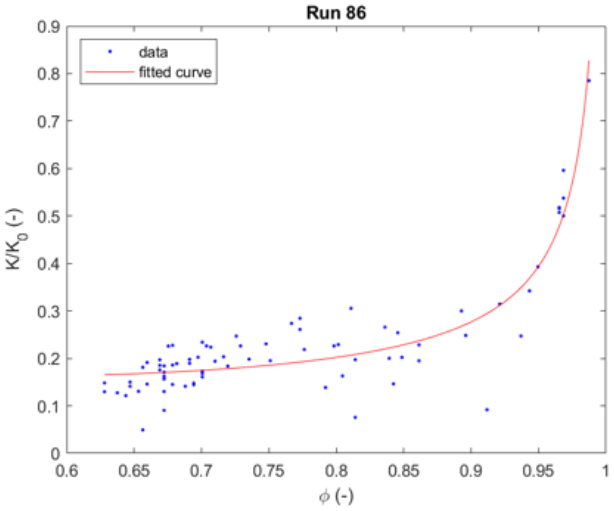
Run 86
data
fitted curve
K/K0 (-)
ϕ (-)

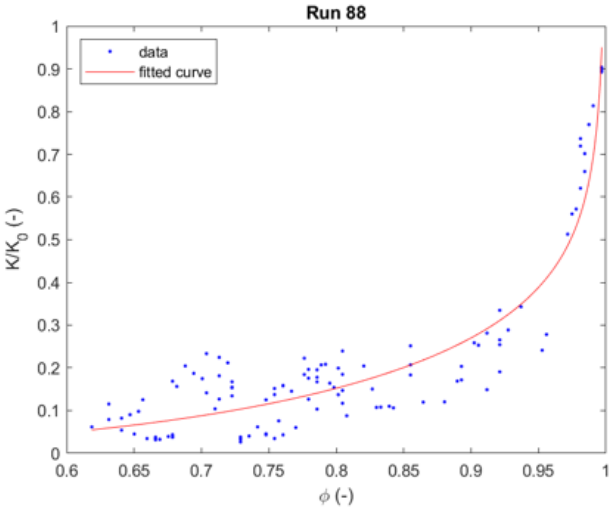
Run 88
data
fitted curve
K/K0 (-)
ϕ (-)

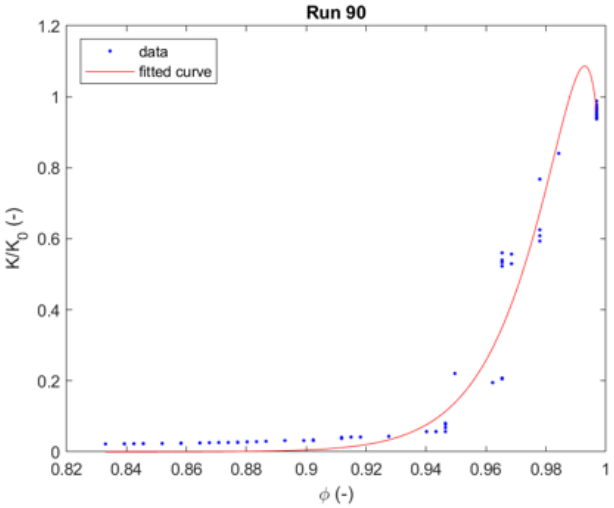
Run 90
data
fitted curve
K/K0 (-)
ϕ (-)

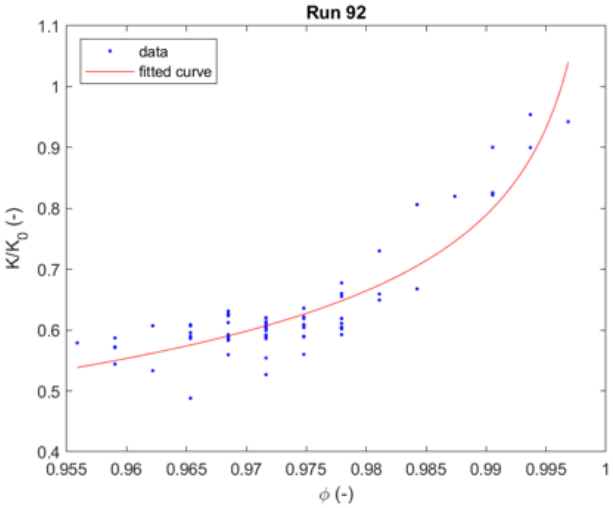
Run 92
data
fitted curve
K/K0 (-)
ϕ (-)

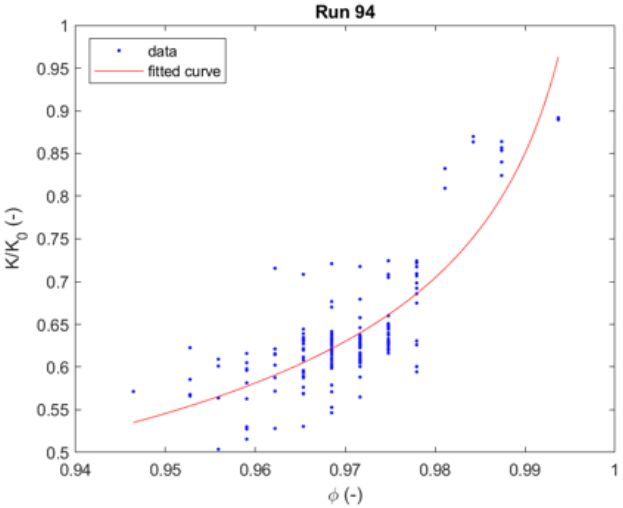
Run 94
data
fitted curve
K/K0 (-)
ϕ (-)

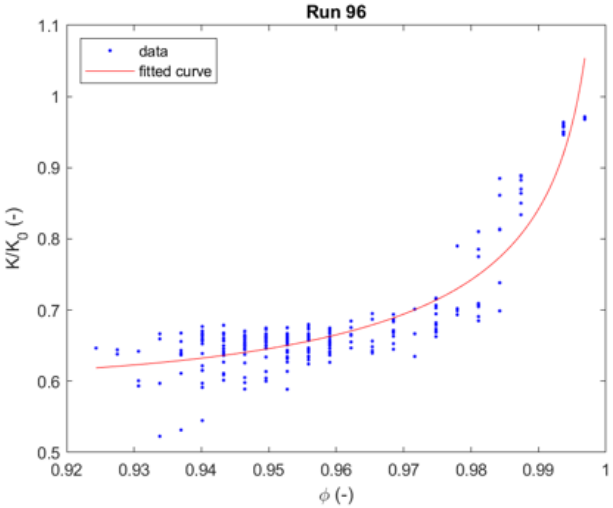
Run 96
data
fitted curve
K/K0 (-)
ϕ (-)

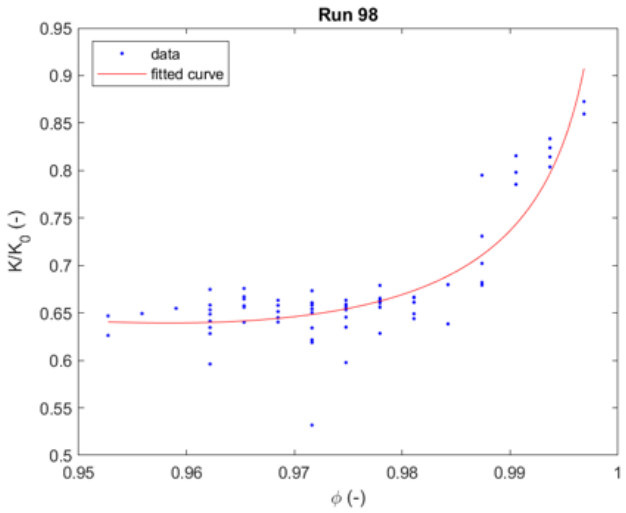
Run 98
data
fitted curve
K/K0 (-)
ϕ (-)

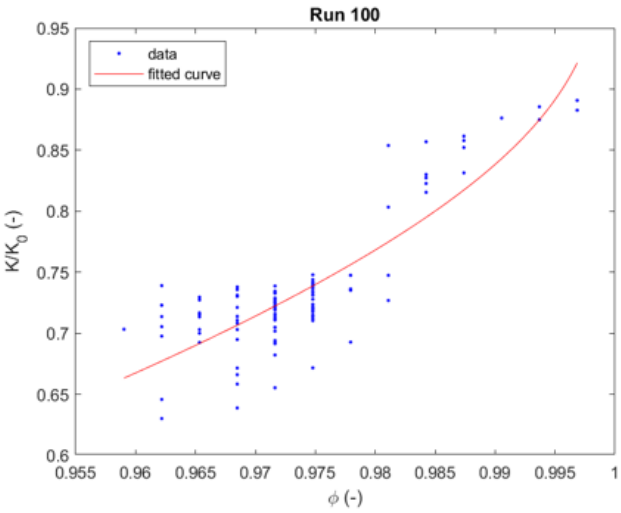
Run 100
data
fitted curve
K/K0 (-)
ϕ (-)

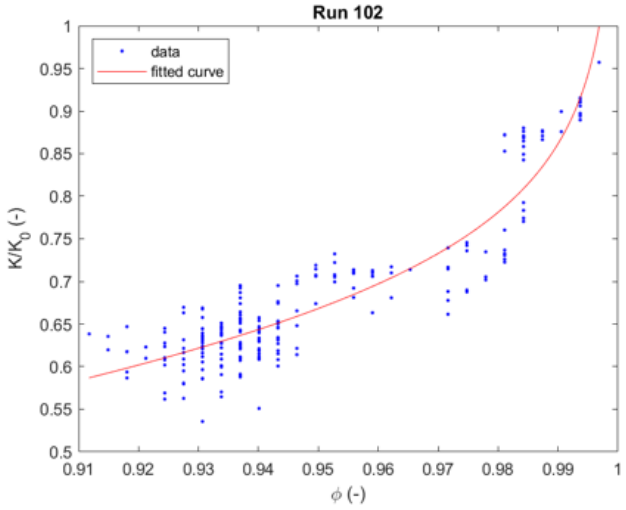
Run 102
data
fitted curve
K/K0 (-)
ϕ (-)

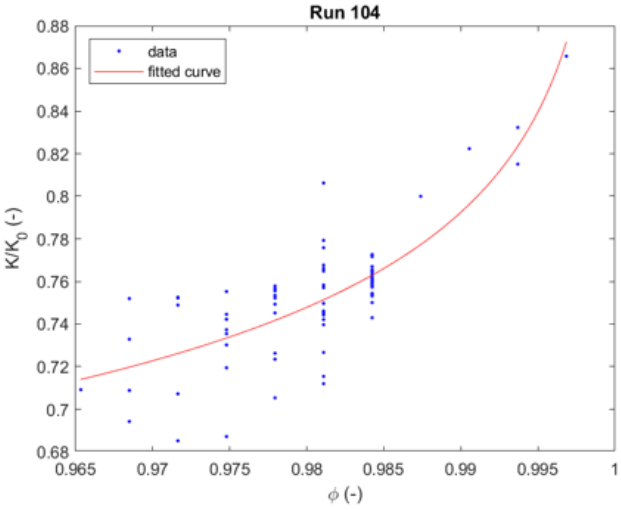
Run 104
data
fitted curve
K/K0 (-)
ϕ (-)

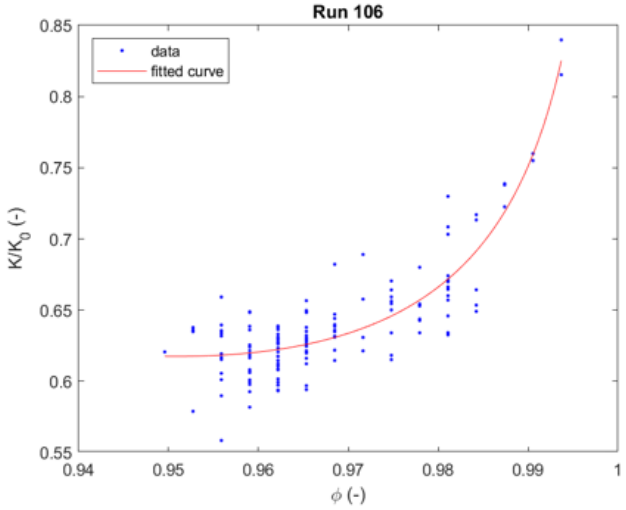
Run 106
data
fitted curve
K/K0 (-)
ϕ (-)

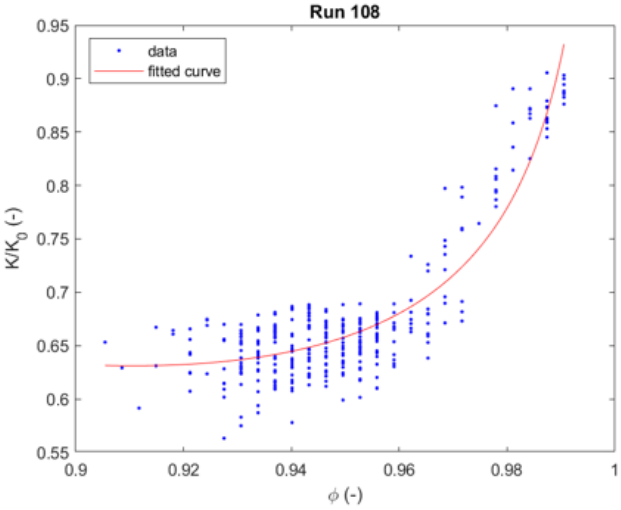
Run 108
data
fitted curve
K/K0 (-)
ϕ (-)

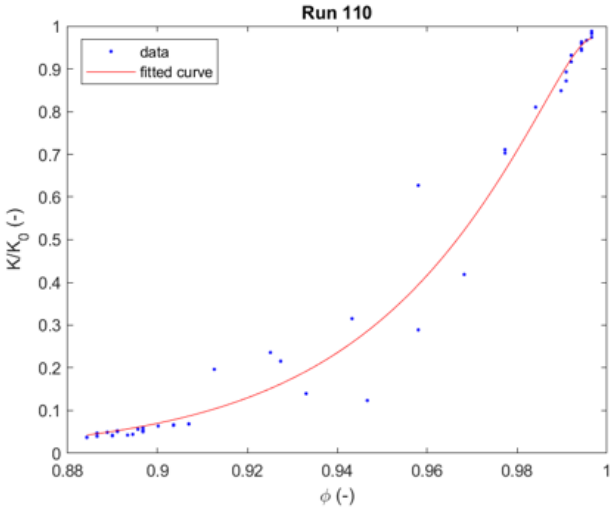
Run 110
data
fitted curve
K/K0 (-)
ϕ (-)

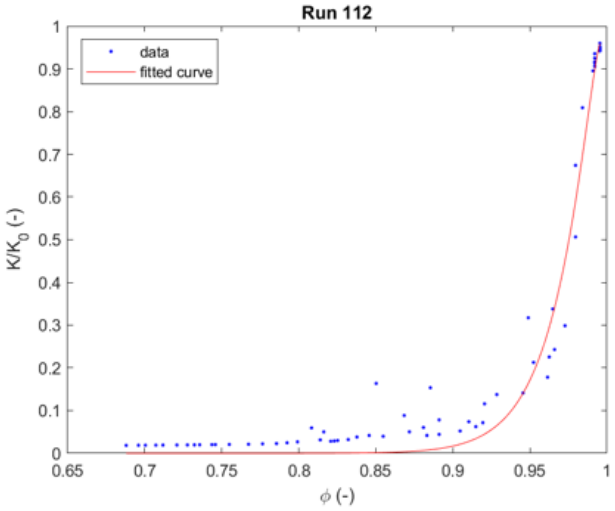
Run 112
data
fitted curve
K/K0 (-)
ϕ (-)

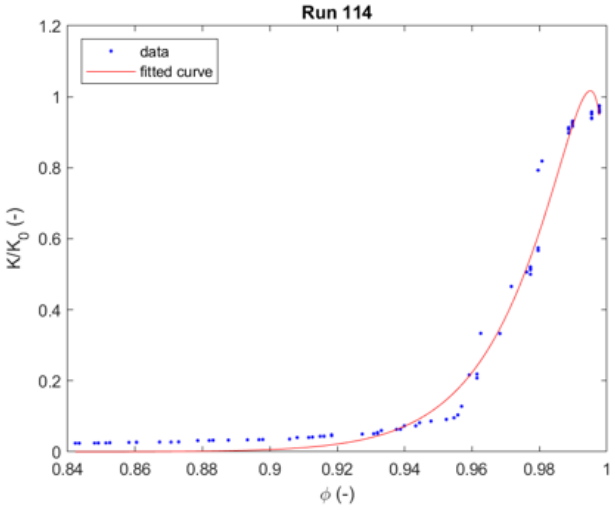
Run 114
data
fitted curve
K/K0 (-)
ϕ (-)

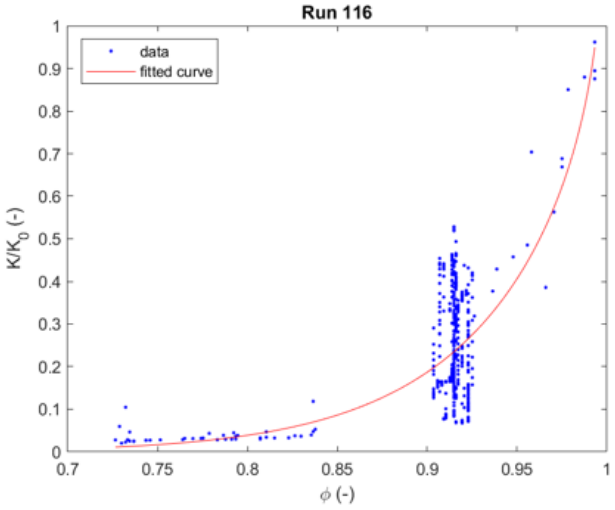
Run 116
data
fitted curve
K/K0 (-)
ϕ (-)

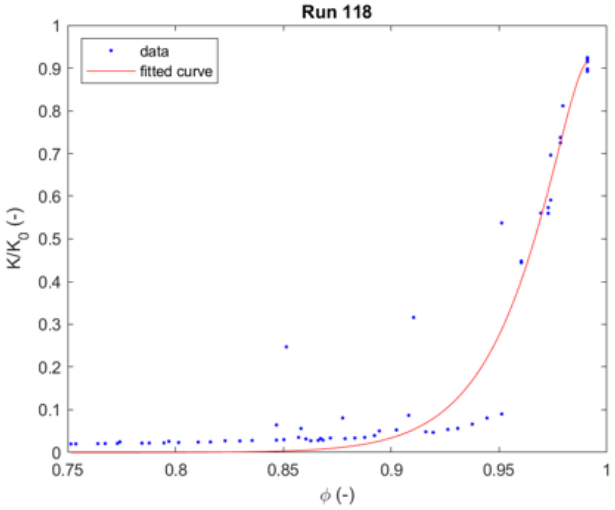
Run 118
data
fitted curve
K/K0 (-)
ϕ (-)

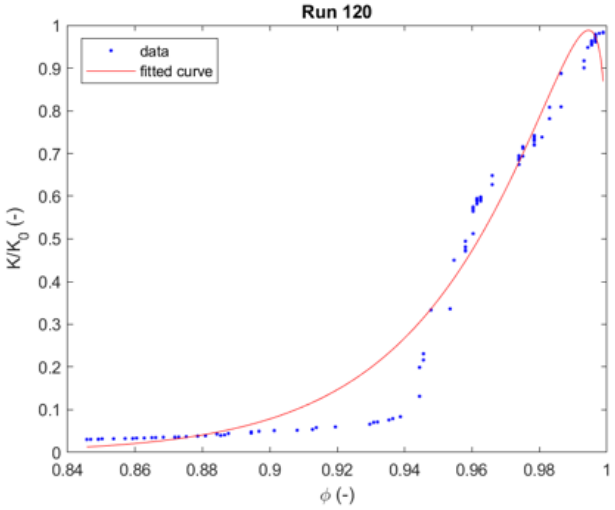
Run 120
data
fitted curve
K/K0 (-)
ϕ (-)

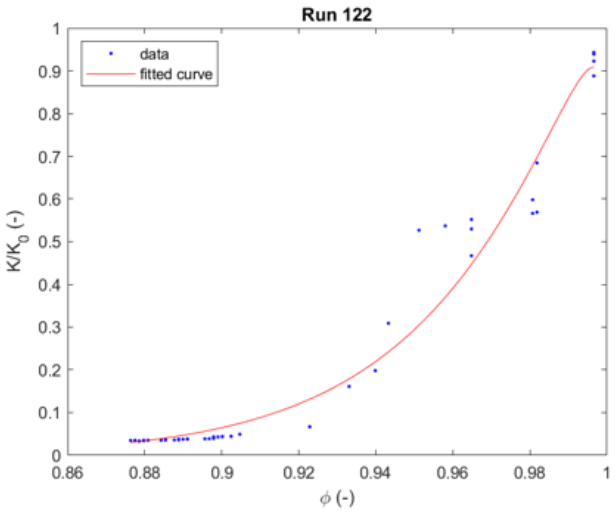
Run 122
data
fitted curve
K/K0 (-)
ϕ (-)

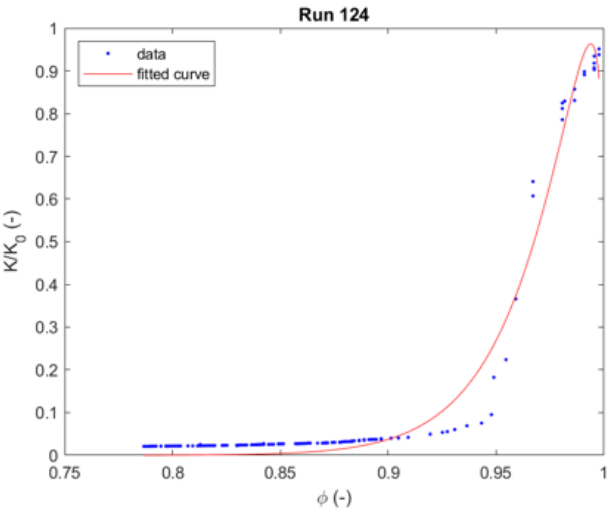
Run 124
data
fitted curve
K/K0 (-)
ϕ (-)

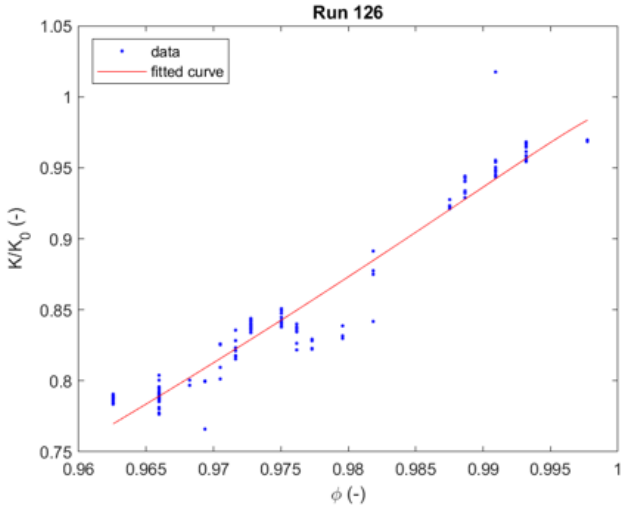
Run 126
data
fitted curve
K/K0 (-)
ϕ (-)

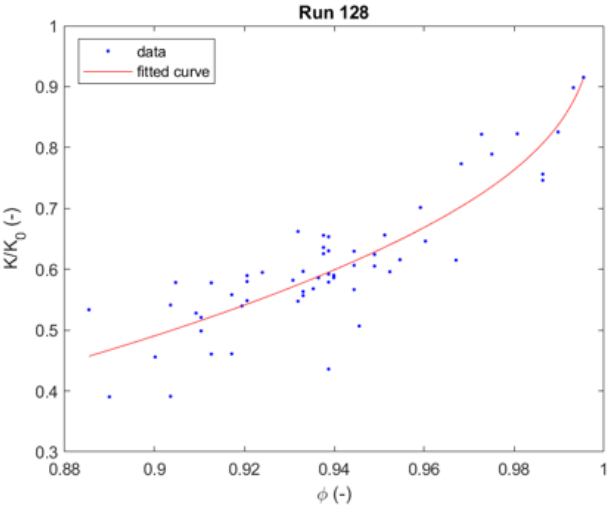
Run 128
data
fitted curve
K/K0 (-)
ϕ (-)

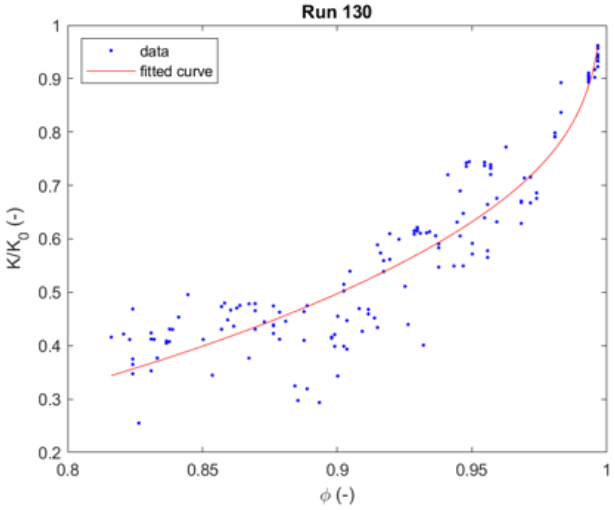
Run 130
data
fitted curve
K/K0 (-)
ϕ (-)

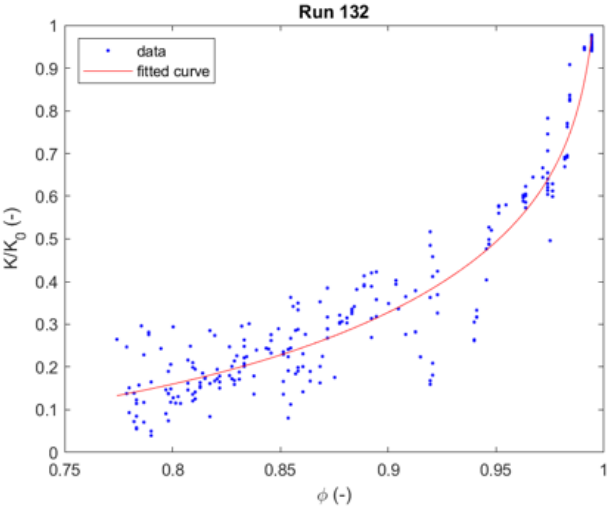
Run 132
data
fitted curve
K/K0 (-)
ϕ (-)

b

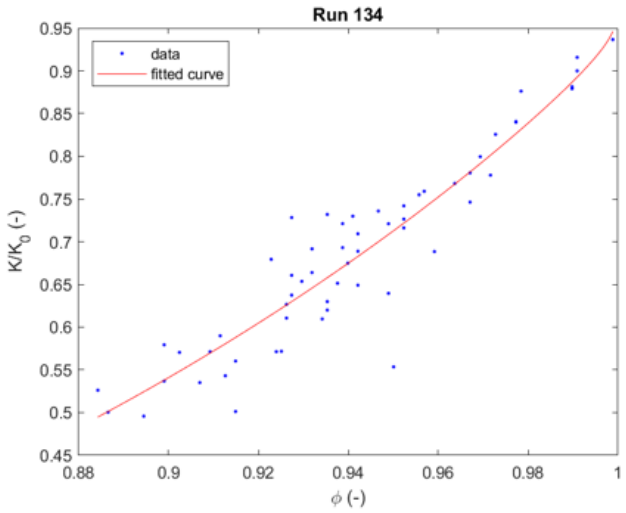
Run 134
data
fitted curve
K/K0 (-)
ϕ (-)

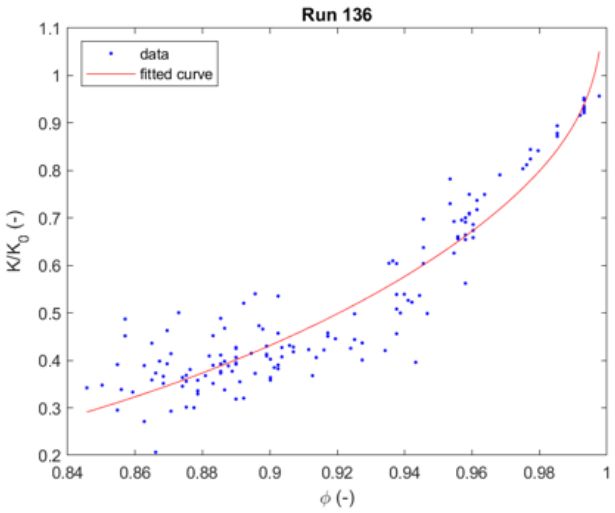
Run 136
data
fitted curve
K/K0 (-)
ϕ (-)

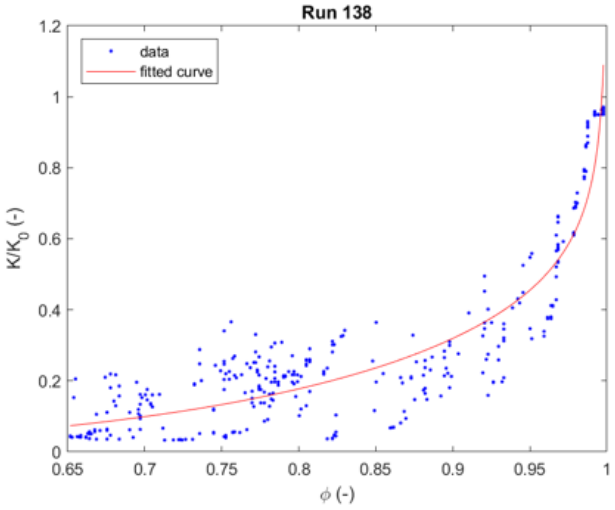
Run 138
data
fitted curve
K/K0 (-)
ϕ (-)

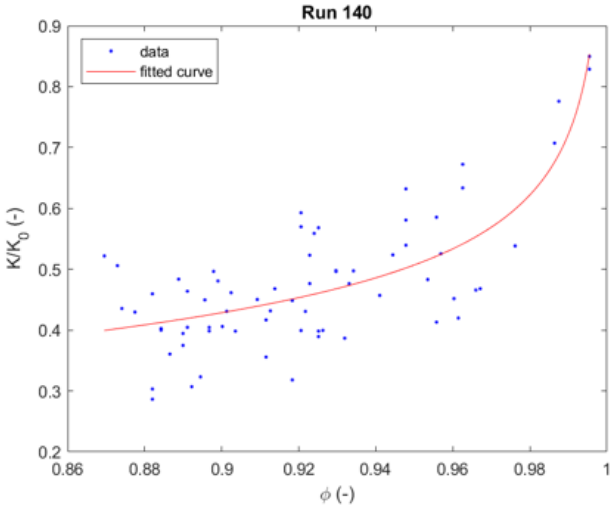
Run 140
data
fitted curve
K/K0 (-)
ϕ (-)

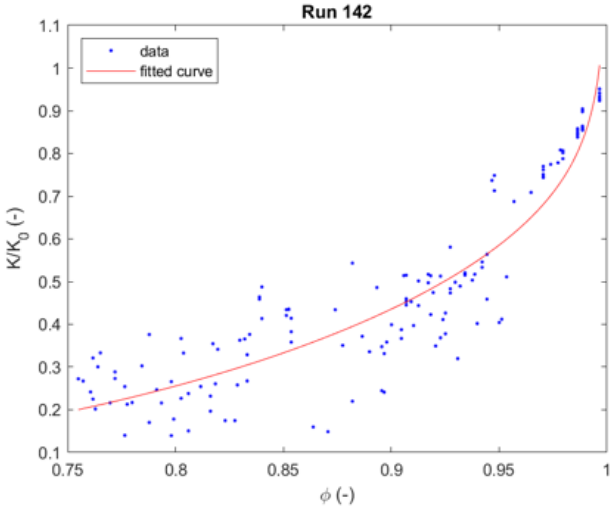
Run 142
data
fitted curve
K/K0 (-)
ϕ (-)

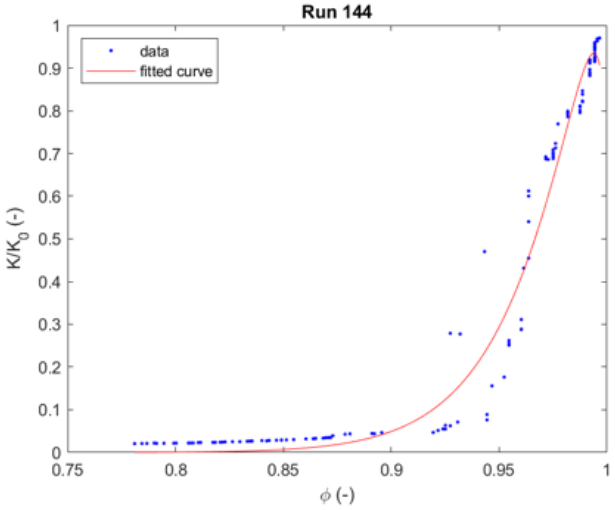
Run 144
data
fitted curve
K/K0 (-)
ϕ (-)

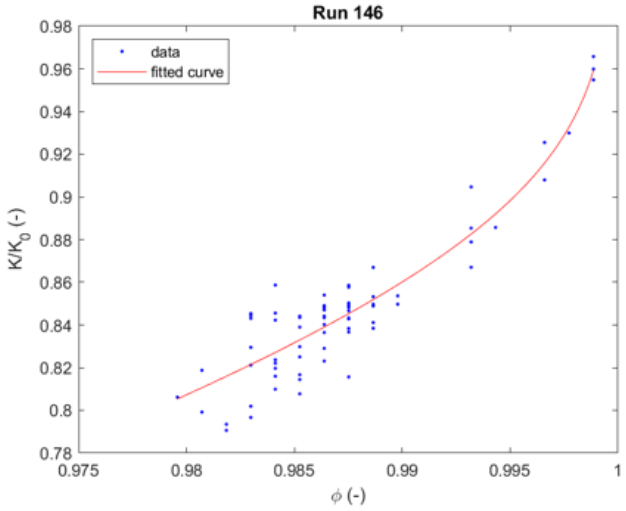
Run 146
data
fitted curve
K/K0 (-)
ϕ (-)

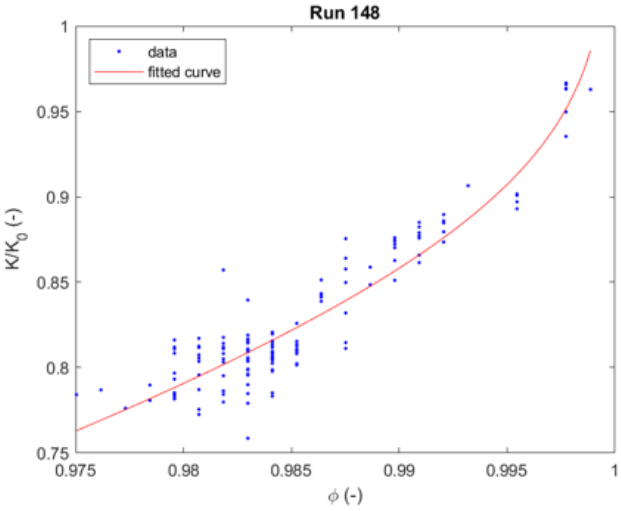
Run 148
data
fitted curve
K/K0 (-)
ϕ (-)

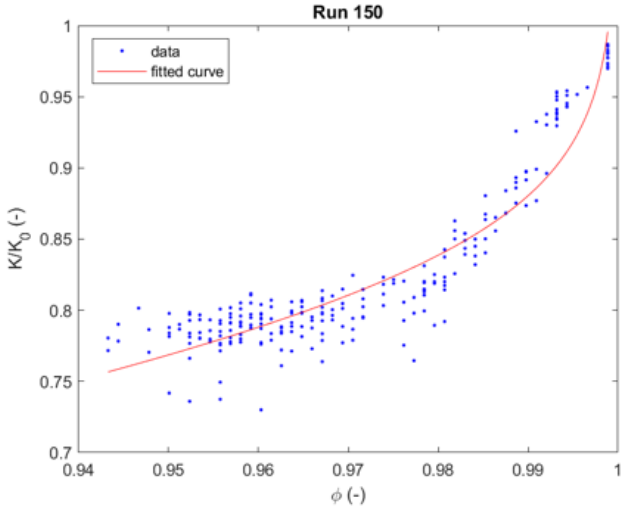
Run 150
data
fitted curve
K/K0 (-)
ϕ (-)

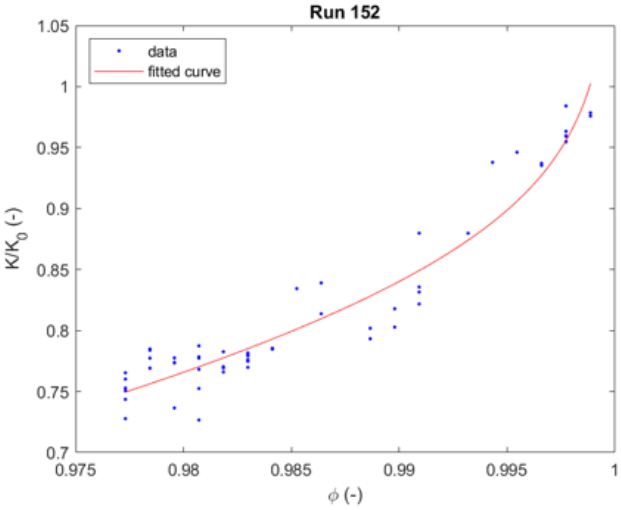
Run 152
data
fitted curve
K/K0 (-)
ϕ (-)

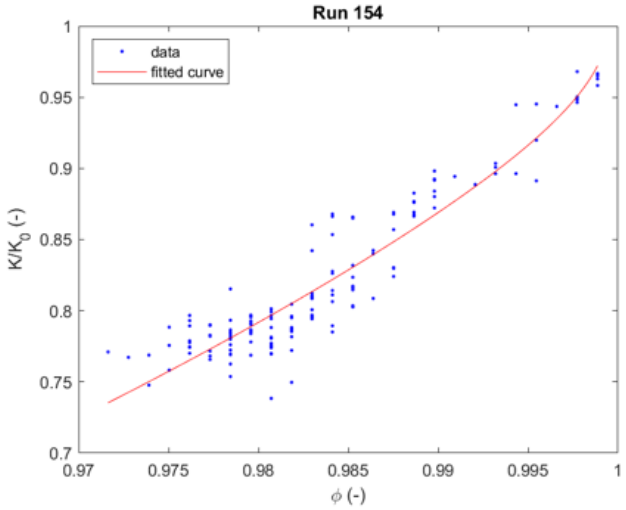
Run 154
data
fitted curve
K/K0 (-)
ϕ (-)

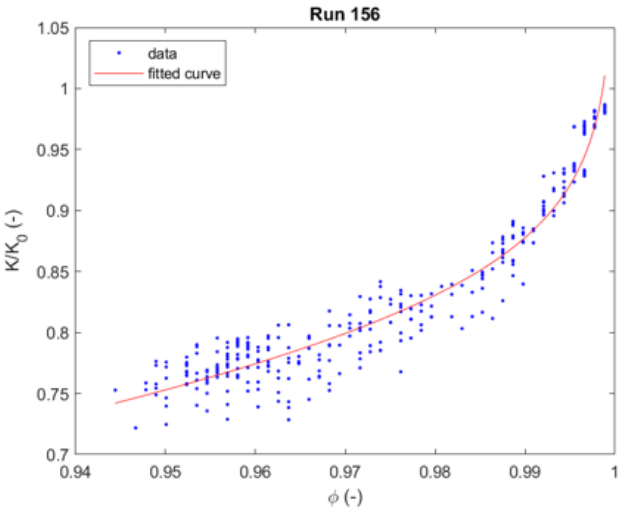
Run 156
data
fitted curve
K/K0 (-)
ϕ (-)

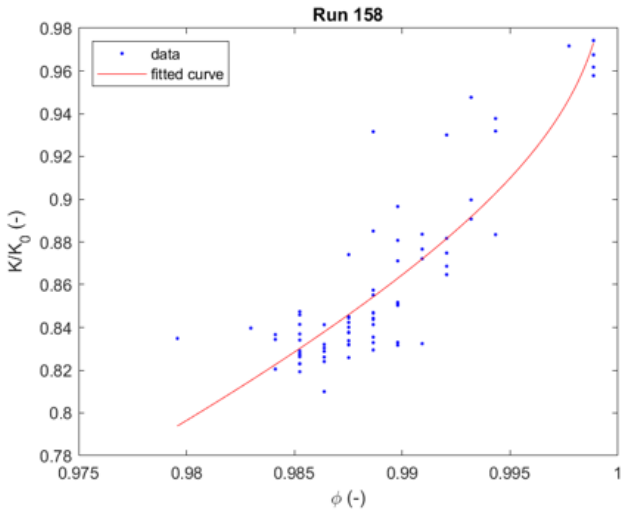
Run 158
data
fitted curve
K/K0 (-)
ϕ (-)

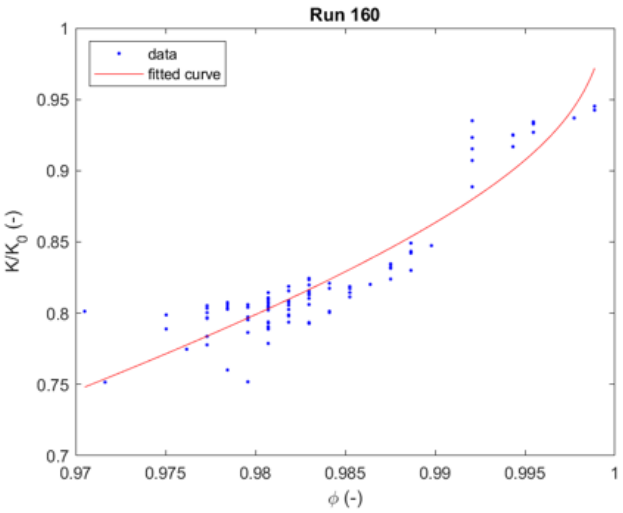
Run 160
data
fitted curve
K/K0 (-)
ϕ (-)

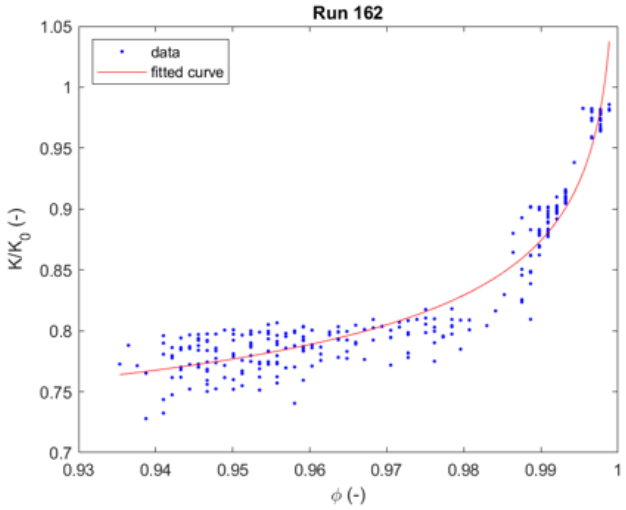
Run 162
data
fitted curve
K/K0 (-)
ϕ (-)

Appendix C

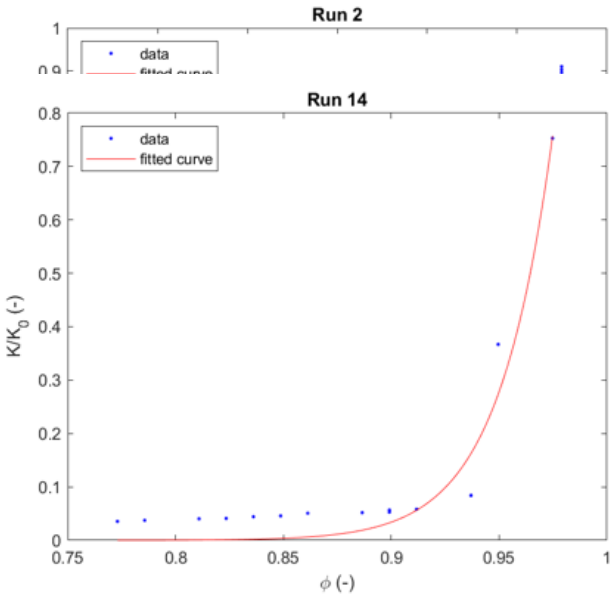
Run 2
data
fitted curve
K/K0 (-)
ϕ (-)

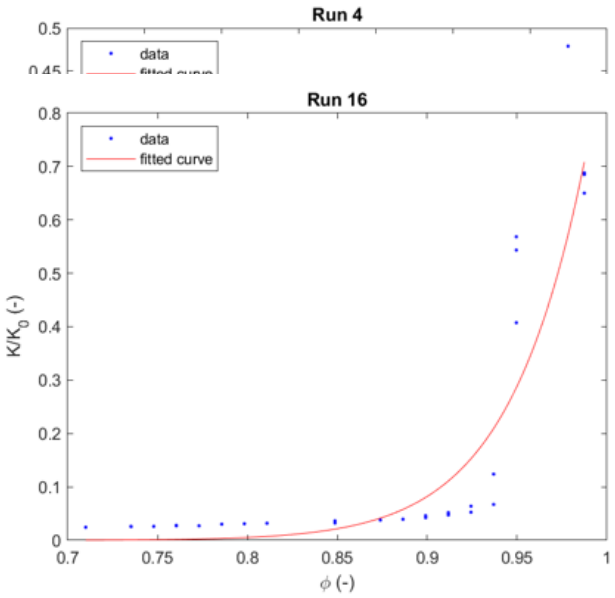
Run 4
data
fitted curve
K/K0 (-)
ϕ (-)

Run 14
data
fitted curve
K/K0 (-)
ϕ (-)

Run 16
data
fitted curve
K/K0 (-)
ϕ (-)

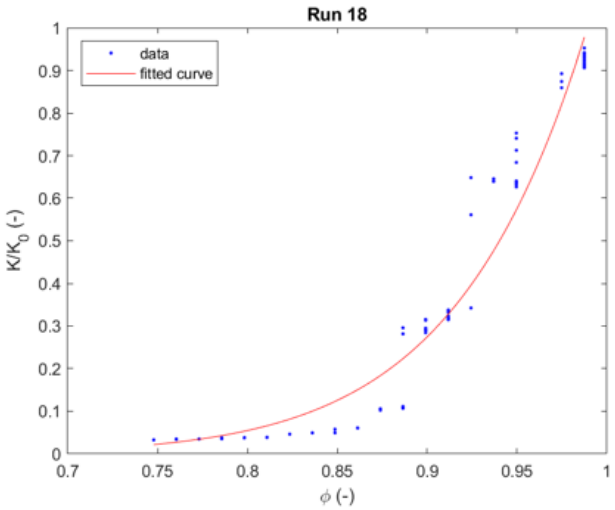
Run 18
data
fitted curve
K/K0 (-)
ϕ (-)

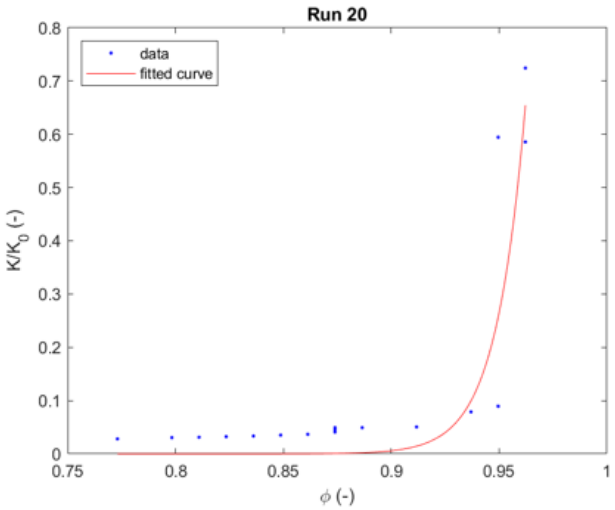
Run 20
data
fitted curve
K/K0 (-)
ϕ (-)

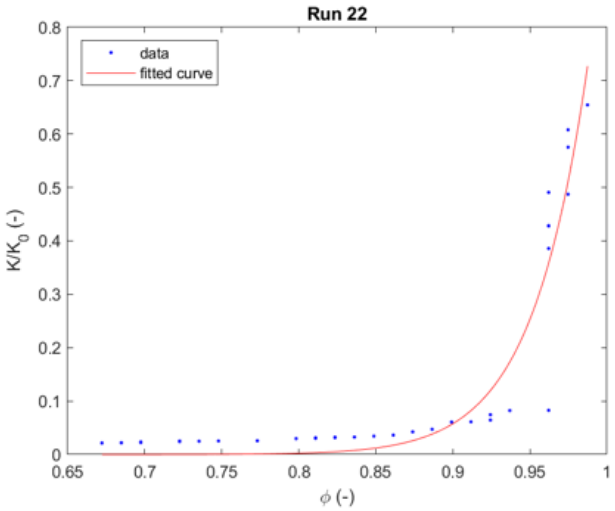
Run 22
data
fitted curve
K/K0 (-)
ϕ (-)

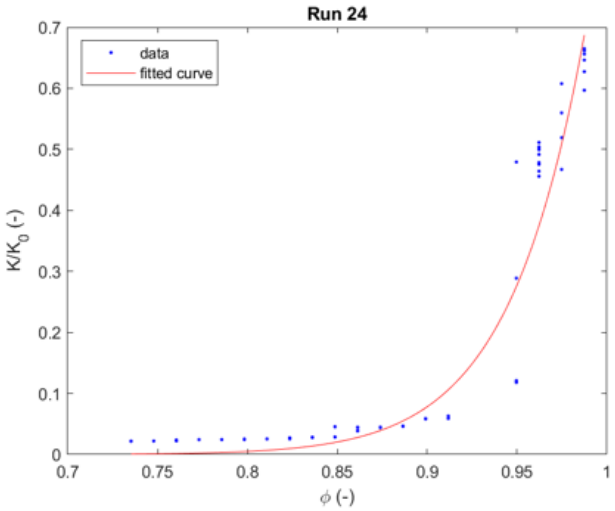
Run 24
data
fitted curve
K/K0 (-)
ϕ (-)

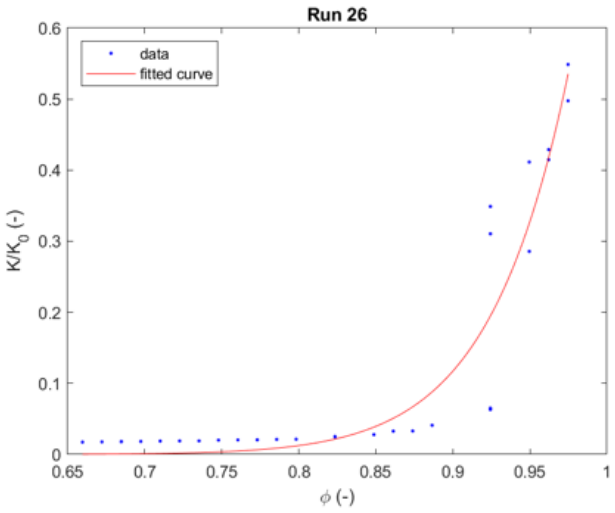
Run 26
data
fitted curve
K/K0 (-)
ϕ (-)

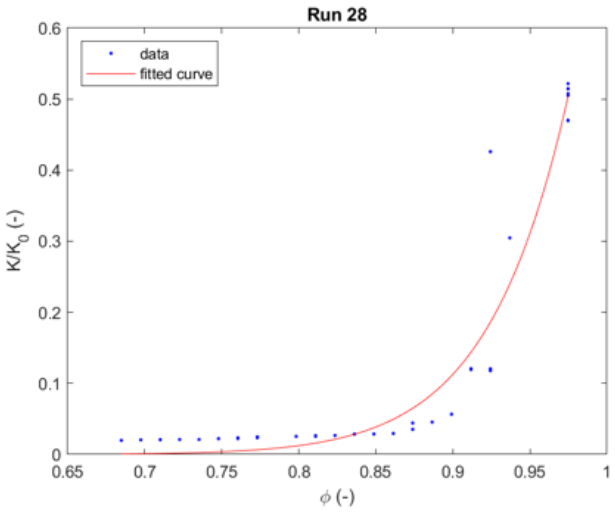
Run 28
data
fitted curve
K/K0 (-)
ϕ (-)

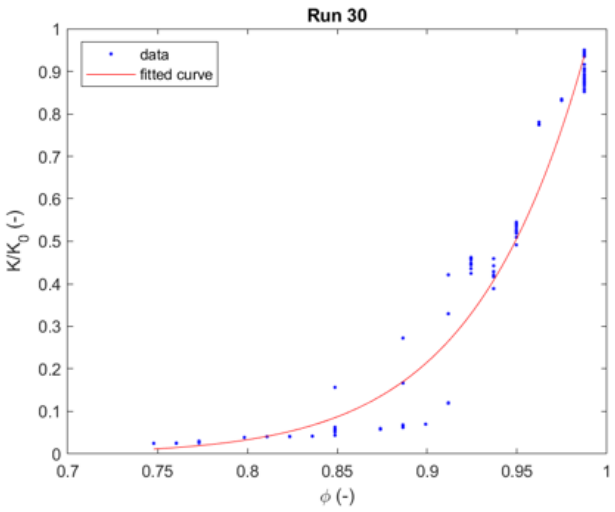
Run 30
data
fitted curve
K/K0 (-)
ϕ (-)

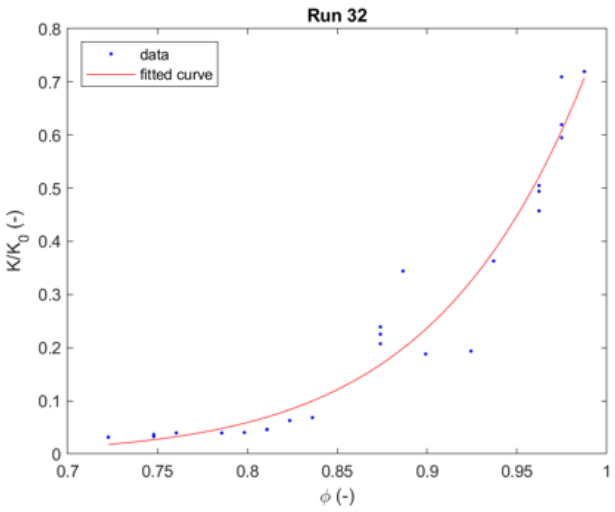
Run 32
data
fitted curve
K/K0 (-)
ϕ (-)

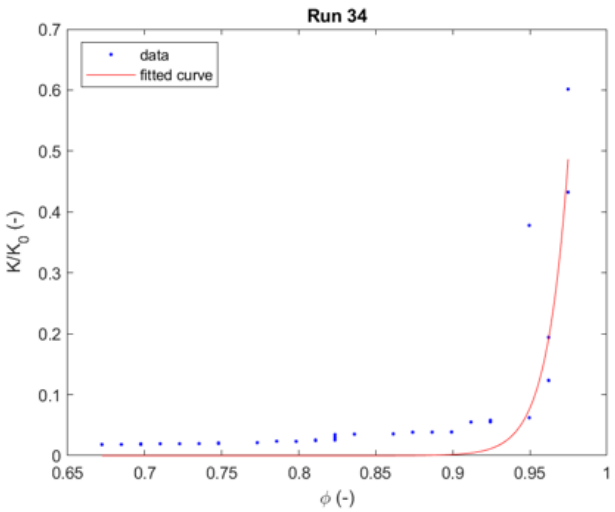
Run 34
data
fitted curve
K/K0 (-)
ϕ (-)

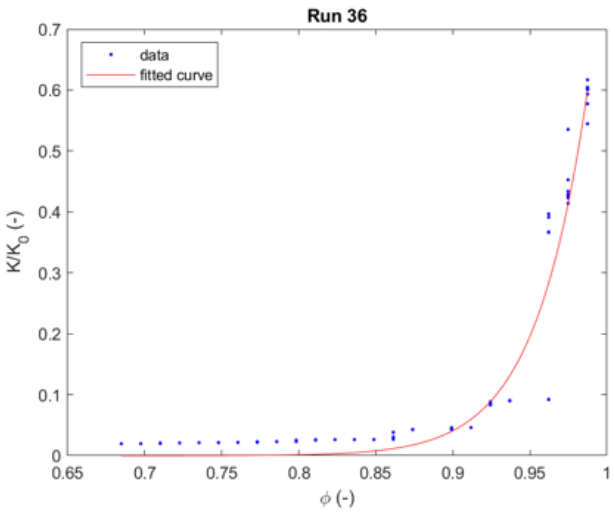
Run 36
data
fitted curve
K/K0 (-)
ϕ (-)

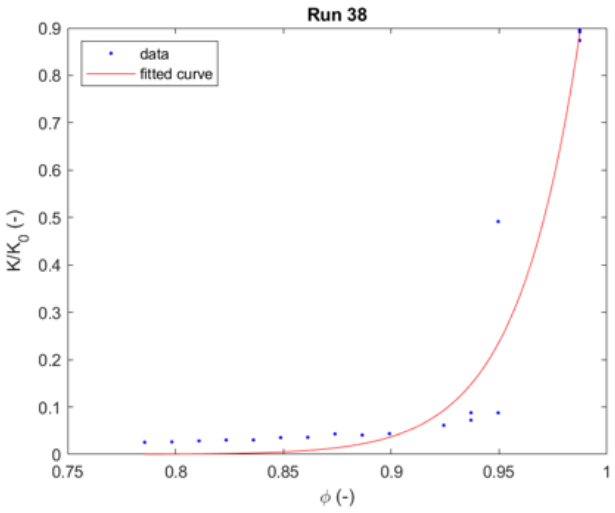
Run 38
data
fitted curve
K/K0 (-)
ϕ (-)

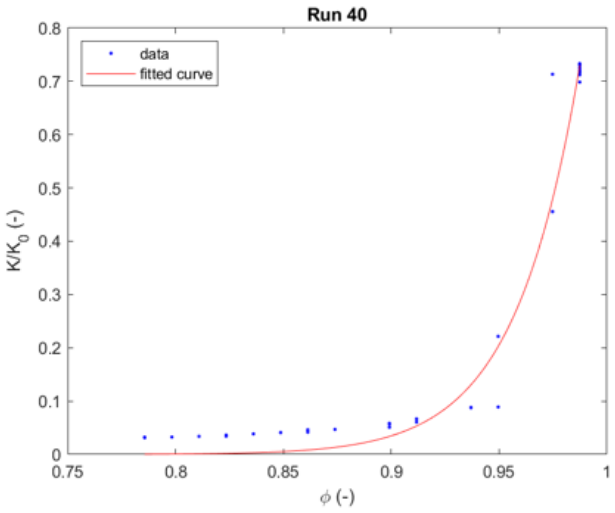
Run 40
data
fitted curve
K/K0 (-)
ϕ (-)

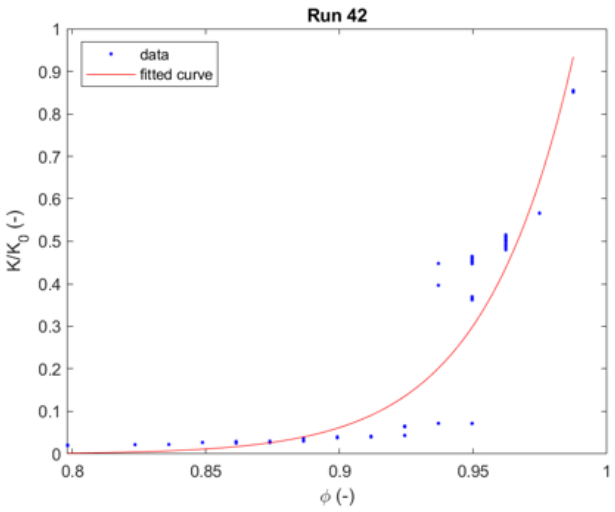
Run 42
data
fitted curve
K/K0 (-)
ϕ (-)

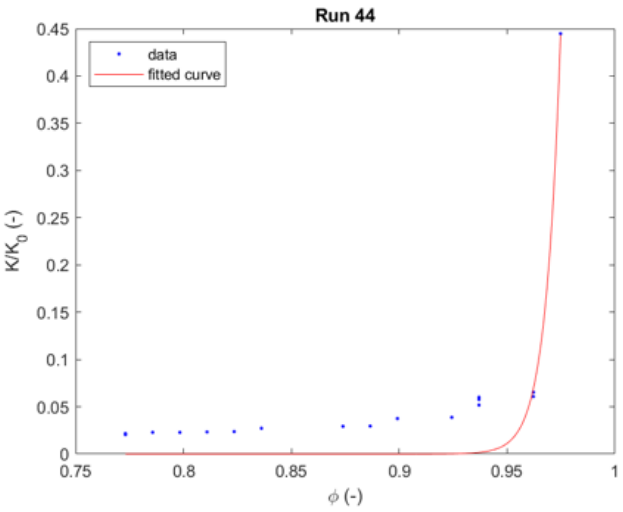
Run 44
data
fitted curve
K/K0 (-)
ϕ (-)

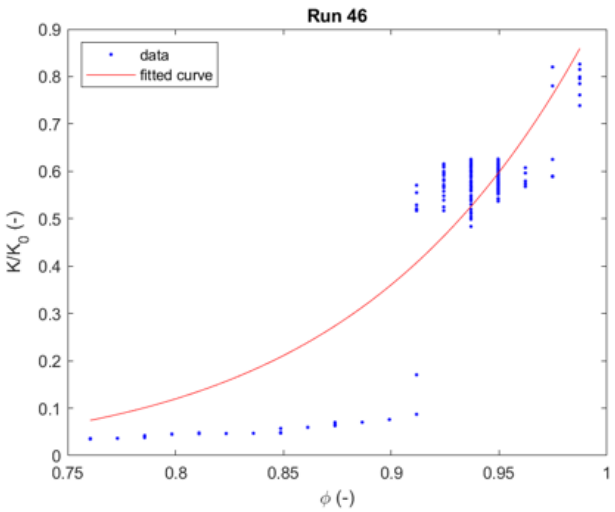
Run 46
data
fitted curve
K/K0 (-)
ϕ (-)

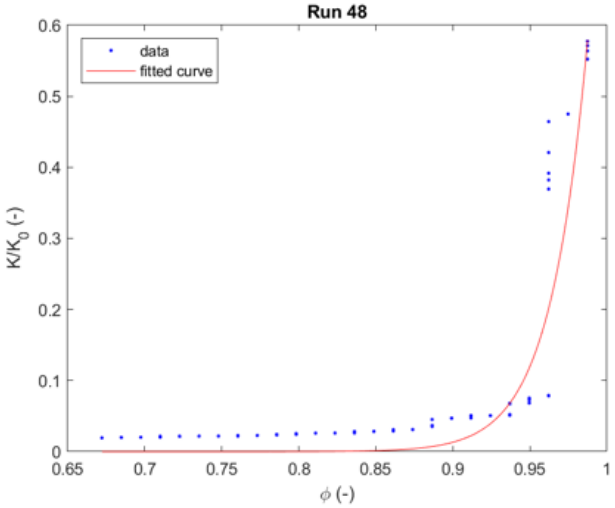
Run 48
data
fitted curve
K/K0 (-)
ϕ (-)

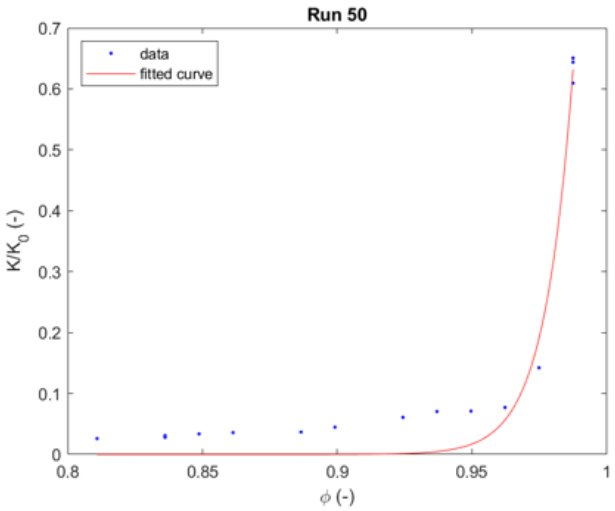
Run 50
data
fitted curve
K/K0 (-)
ϕ (-)

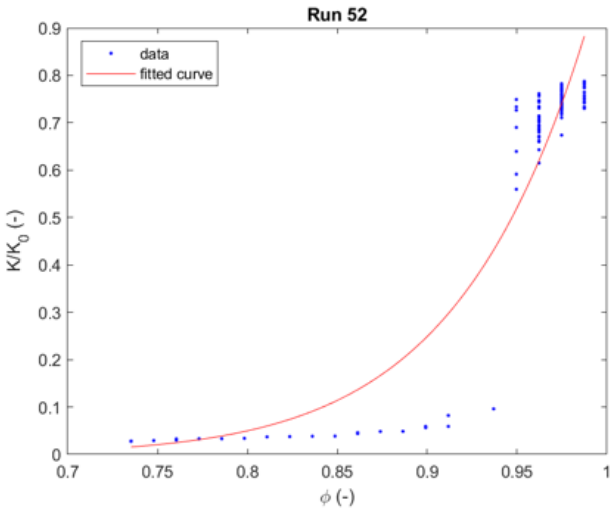
Run 52
data
fitted curve
K/K0 (-)
ϕ (-)

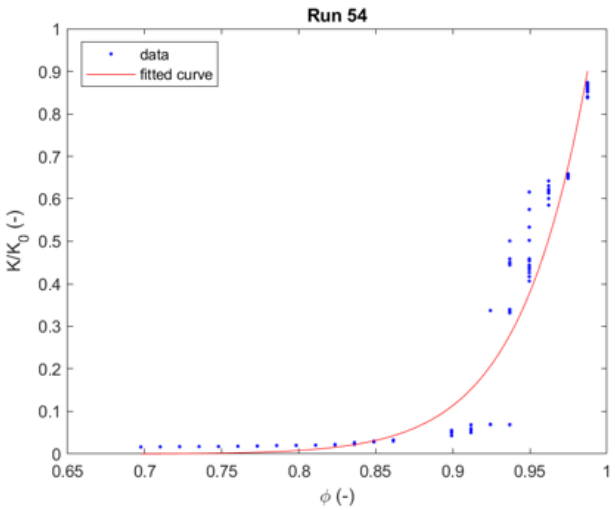
Run 54
data
fitted curve
K/K0 (-)
ϕ (-)

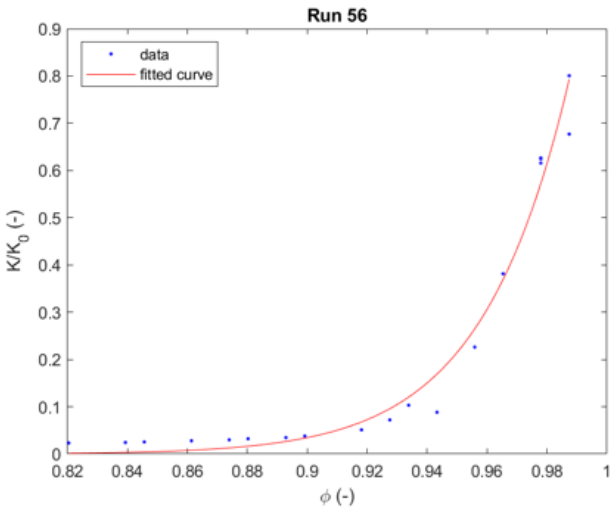
Run 56
data
fitted curve
K/K0 (-)
ϕ (-)

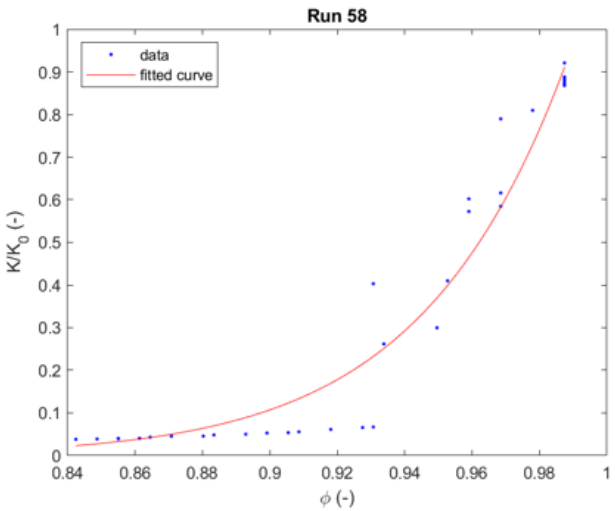
Run 58
data
fitted curve
K/K0 (-)
ϕ (-)

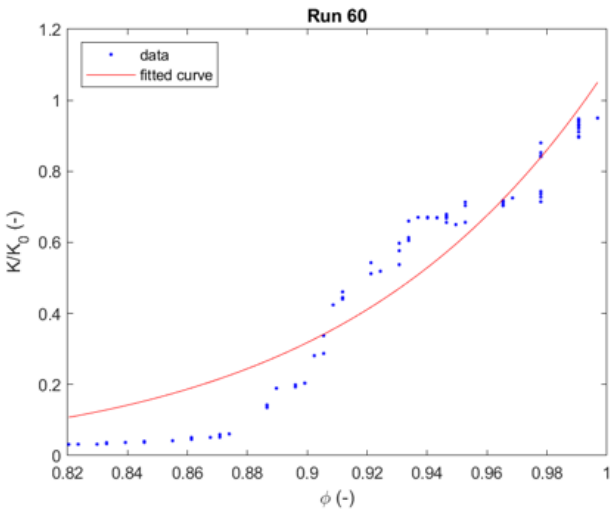
Run 60
data
fitted curve
K/K0 (-)
ϕ (-)

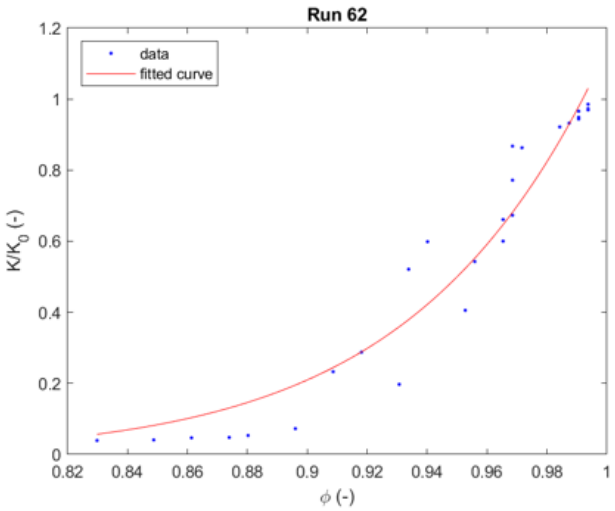
Run 62
data
fitted curve
K/K0 (-)
ϕ (-)

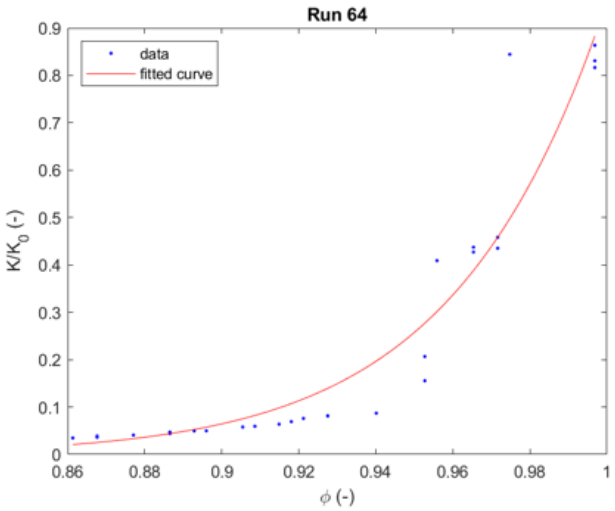
Run 64
data
fitted curve
K/K0 (-)
ϕ (-)

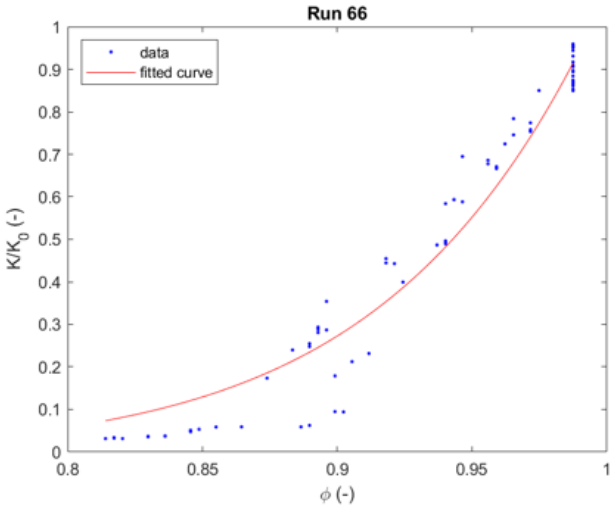
Run 66
data
fitted curve
K/K0 (-)
ϕ (-)

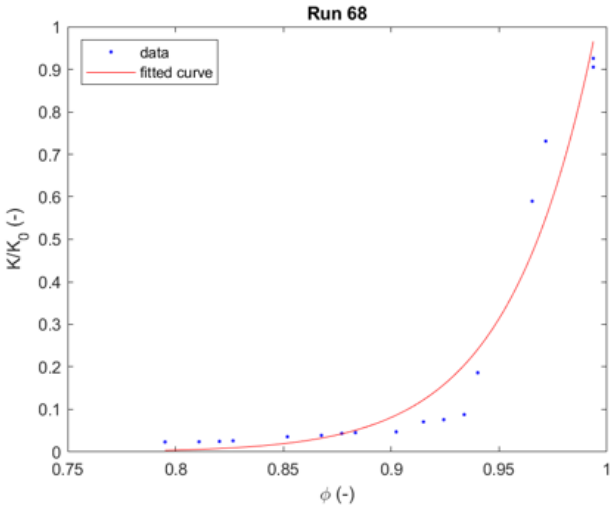
Run 68
data
fitted curve
K/K0 (-)
ϕ (-)

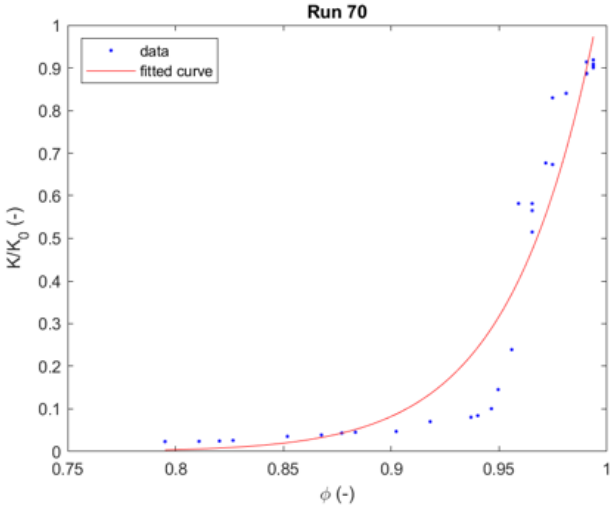
Run 70
data
fitted curve
K/K0 (-)
ϕ (-)

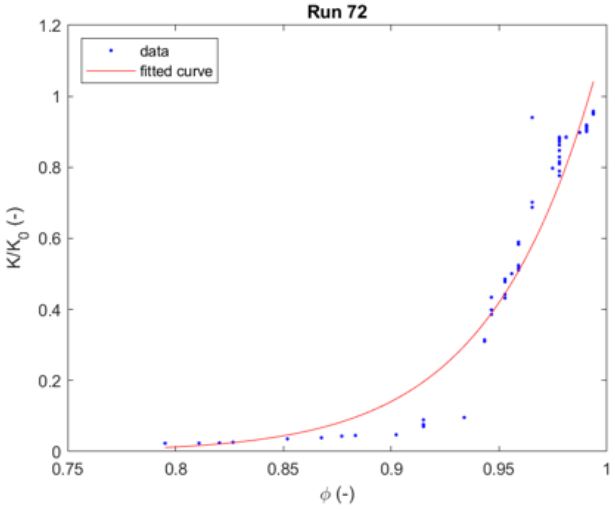
Run 72
data
fitted curve
K/K0 (-)
ϕ (-)

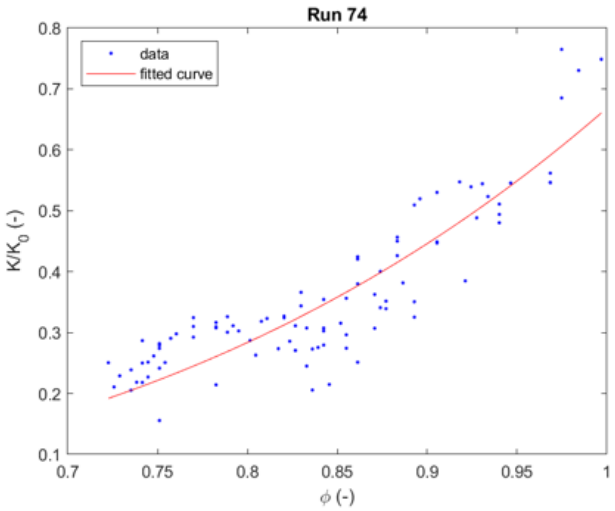
Run 74
data
fitted curve
K/K0 (-)
ϕ (-)

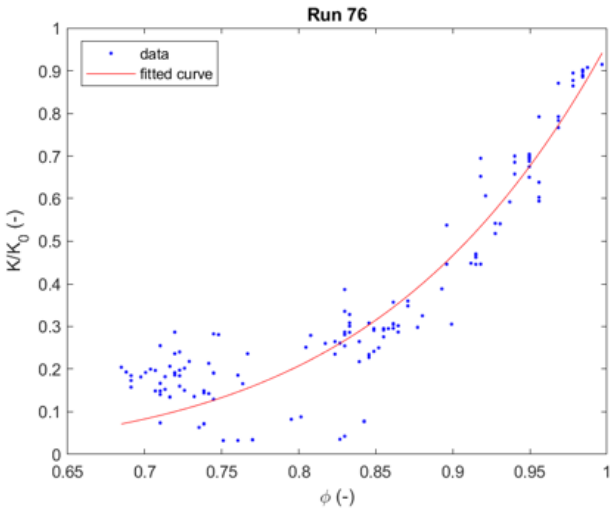
Run 76
data
fitted curve
K/K0 (-)
ϕ (-)

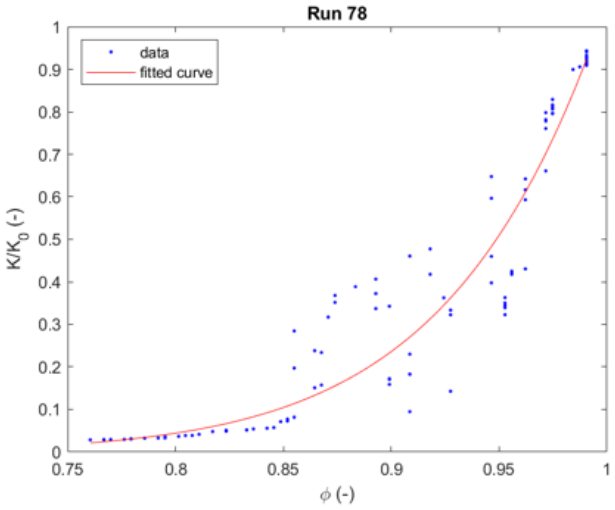
Run 78
data
fitted curve
K/K0 (-)
ϕ (-)

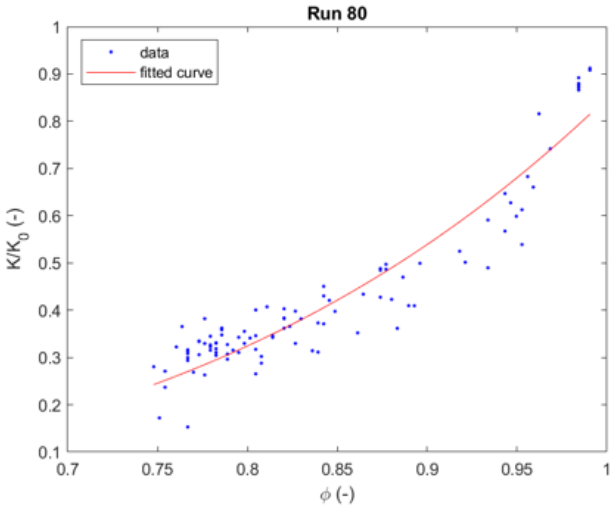
Run 80
data
fitted curve
K/K0 (-)
ϕ (-)

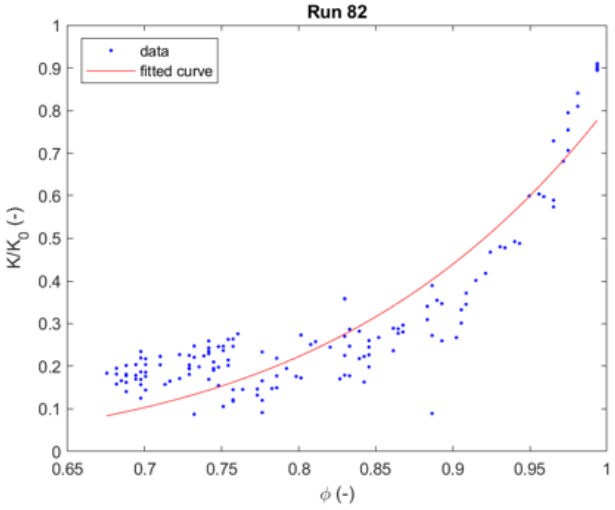
Run 82
data
fitted curve
K/K0 (-)
ϕ (-)

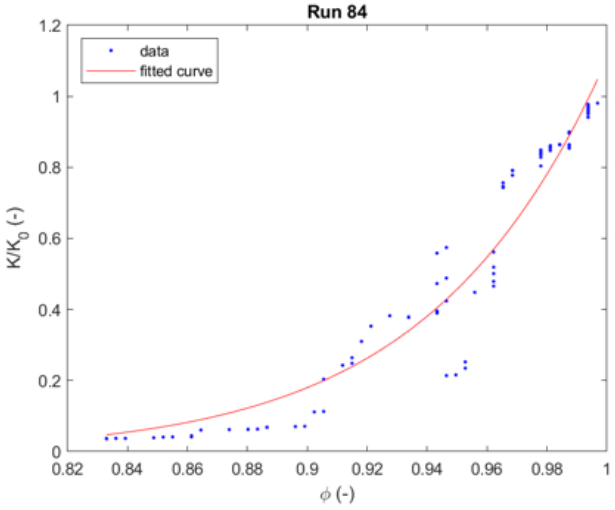
Run 84
data
fitted curve
K/K0 (-)
ϕ (-)

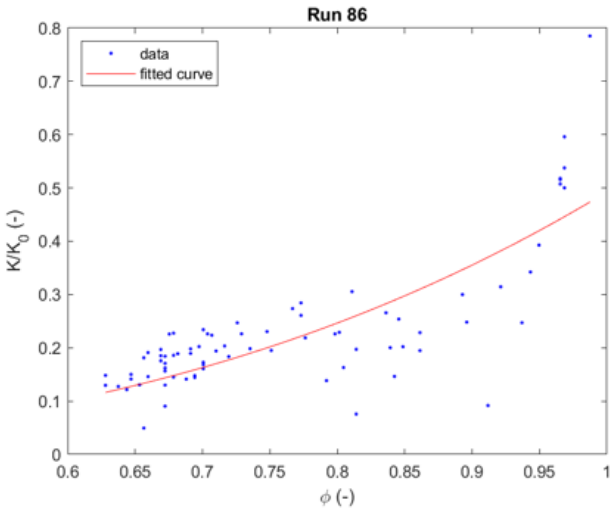
Run 86
data
fitted curve
K/K0 (-)
ϕ (-)

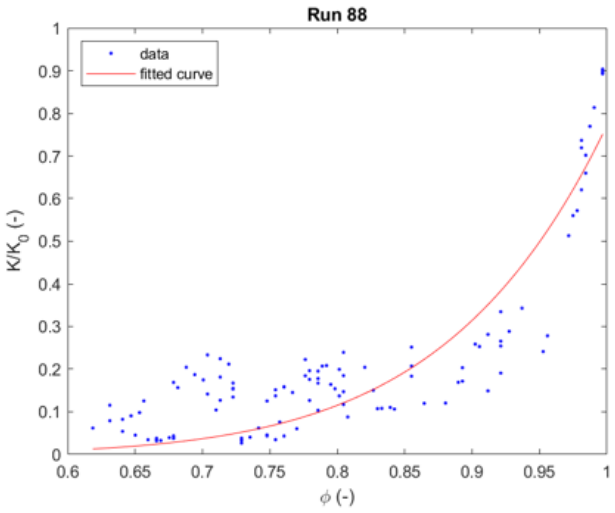
Run 88
data
fitted curve
K/K0 (-)
ϕ (-)

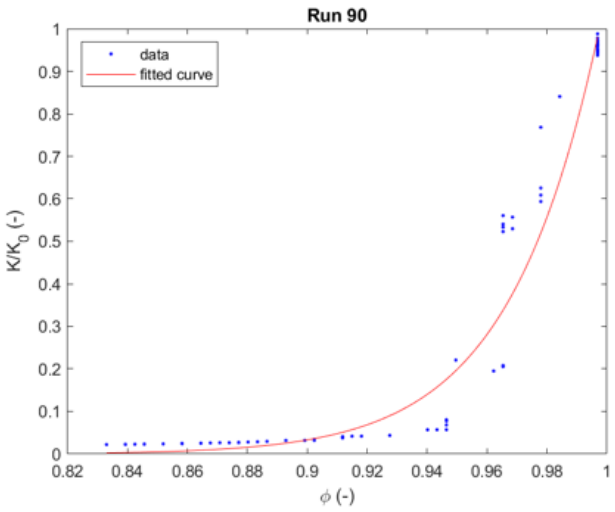
Run 90
data
fitted curve
K/K0 (-)
ϕ (-)

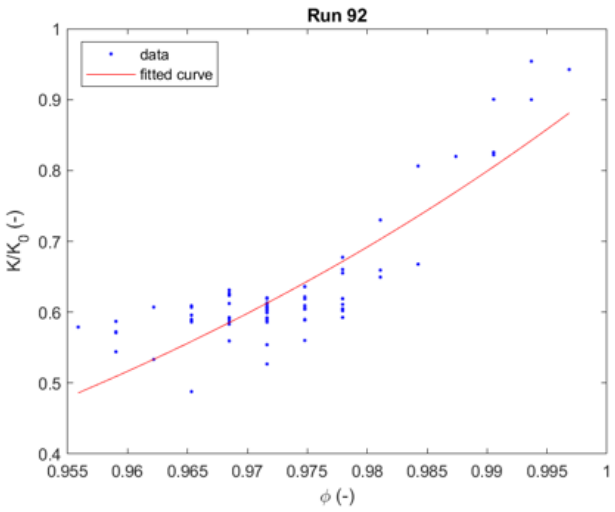
Run 92
data
fitted curve
K/K0 (-)
ϕ (-)

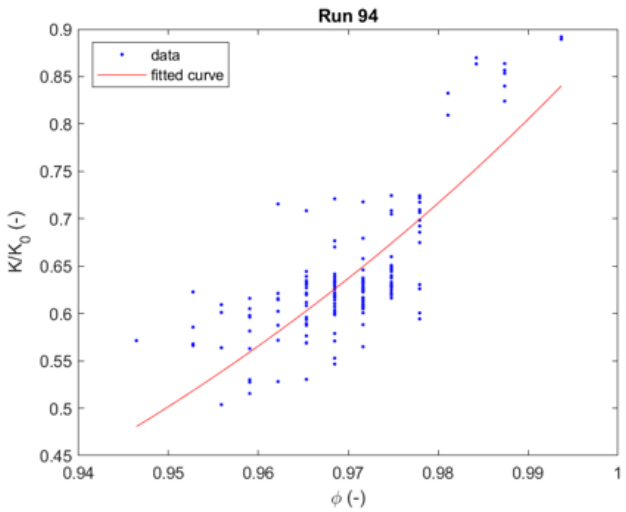
Run 94
data
fitted curve
K/K0 (-)
ϕ (-)

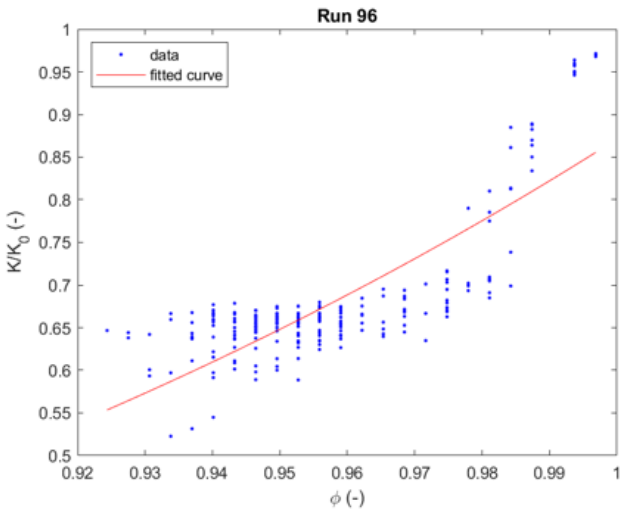
Run 96
data
fitted curve
K/K0 (-)
ϕ (-)

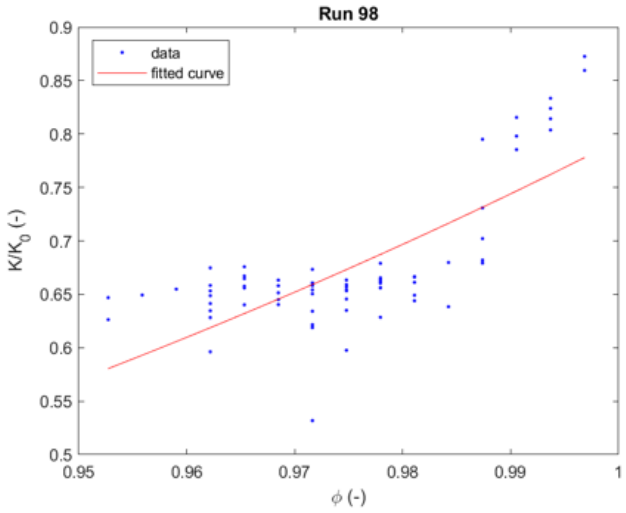
Run 98
data
fitted curve
K/K0 (-)
ϕ (-)

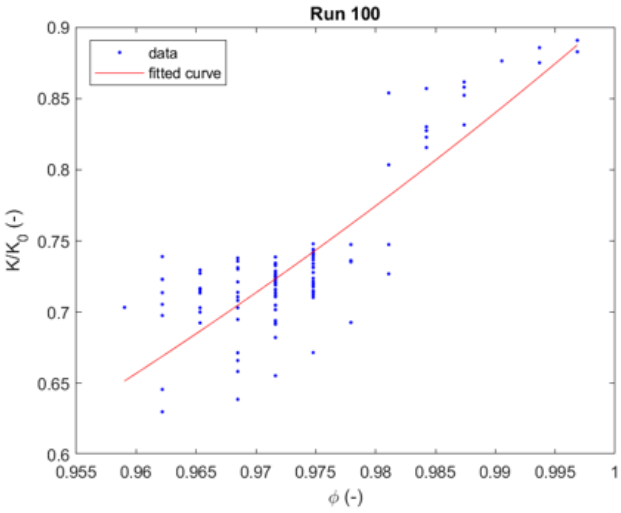
Run 100
data
fitted curve
K/K0 (-)
ϕ (-)

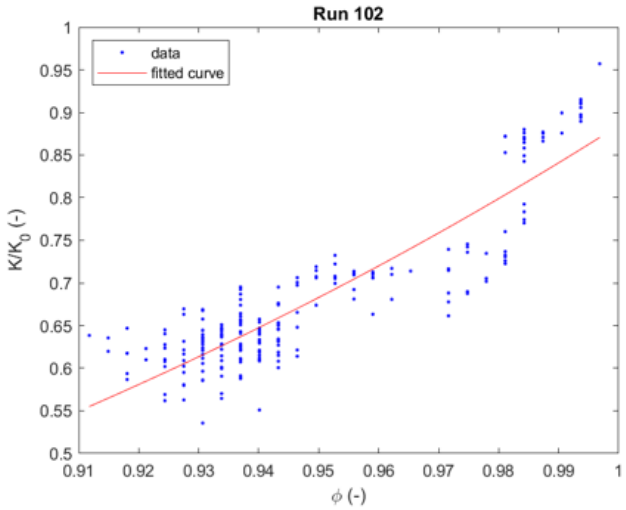
Run 102
data
fitted curve
K/K0 (-)
ϕ (-)

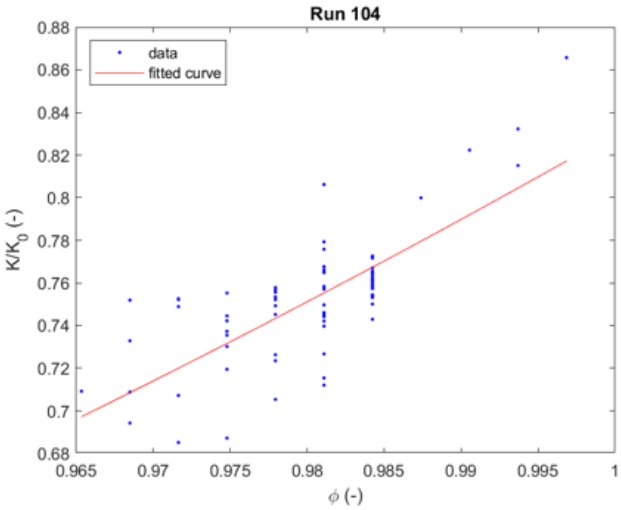
Run 104
data
fitted curve
K/K0 (-)
ϕ (-)

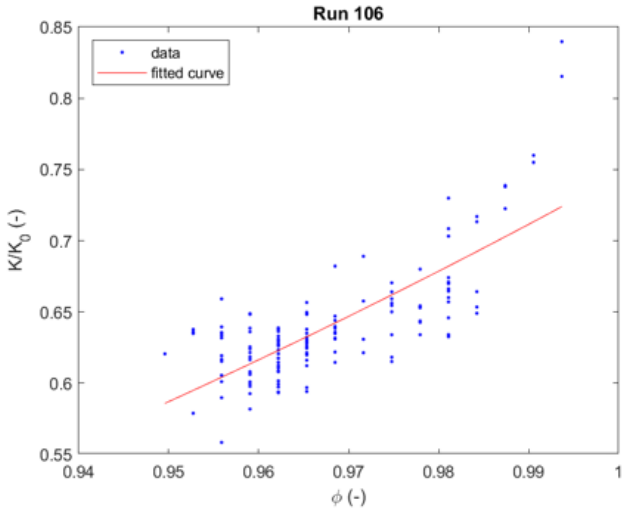
Run 106
data
fitted curve
K/K0 (-)
ϕ (-)

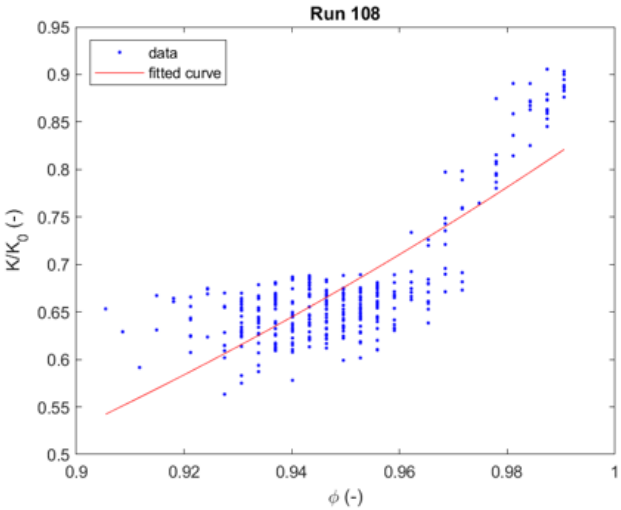
Run 108
data
fitted curve
K/K0 (-)
ϕ (-)

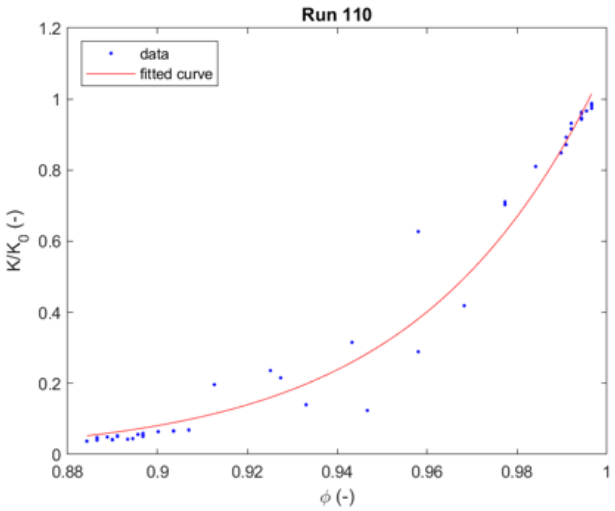
Run 110
data
fitted curve
K/K0 (-)
ϕ (-)

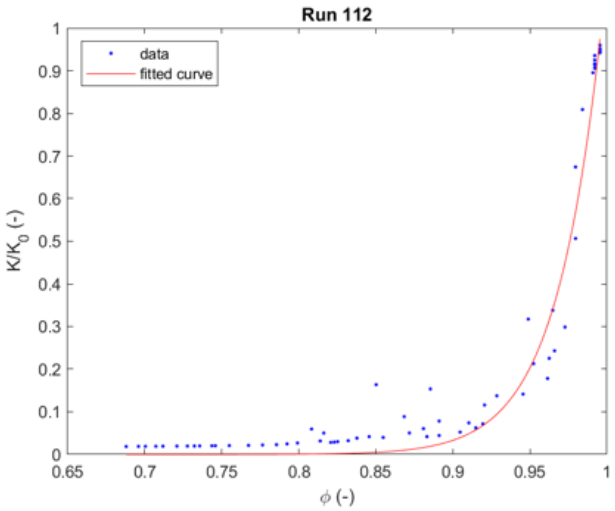
Run 112
data
fitted curve
K/K0 (-)
ϕ (-)

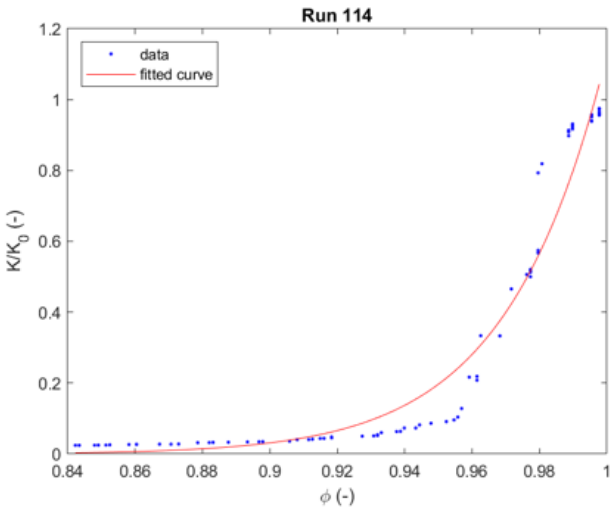
Run 114
data
fitted curve
K/K0 (-)
ϕ (-)

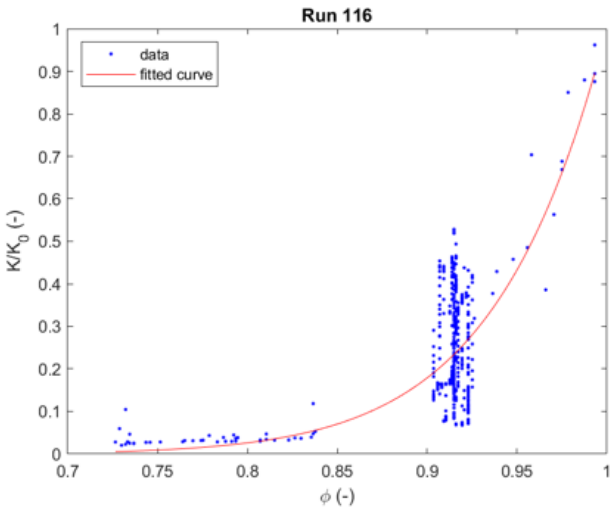
Run 116
data
fitted curve
K/K0 (-)
ϕ (-)

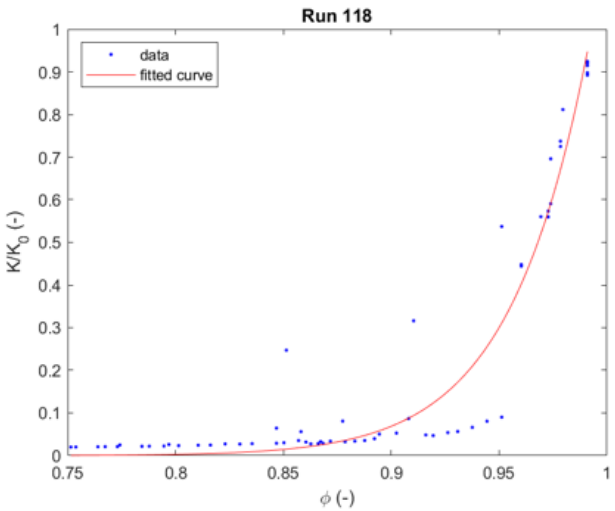
Run 118
data
fitted curve
K/K0 (-)
ϕ (-)

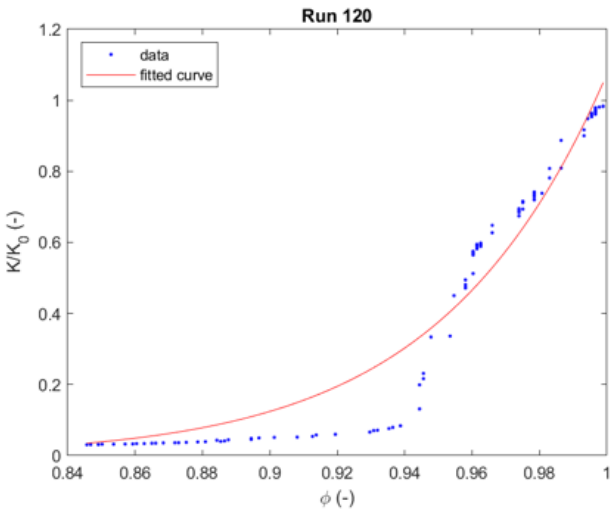
Run 120
data
fitted curve
K/K0 (-)
ϕ (-)

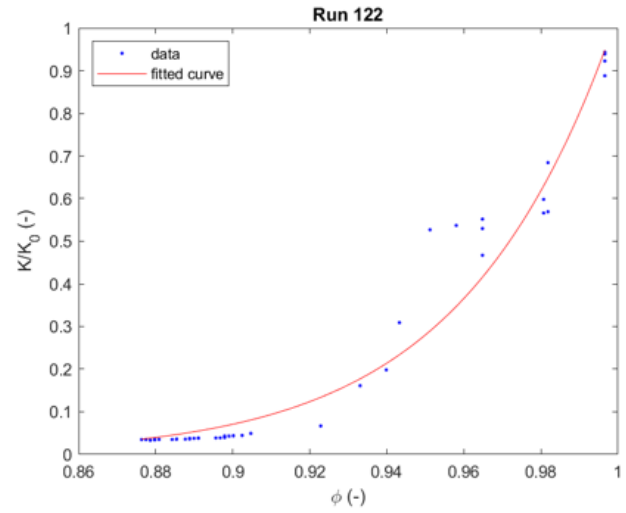
Run 122
data
fitted curve
K/K0 (-)
ϕ (-)

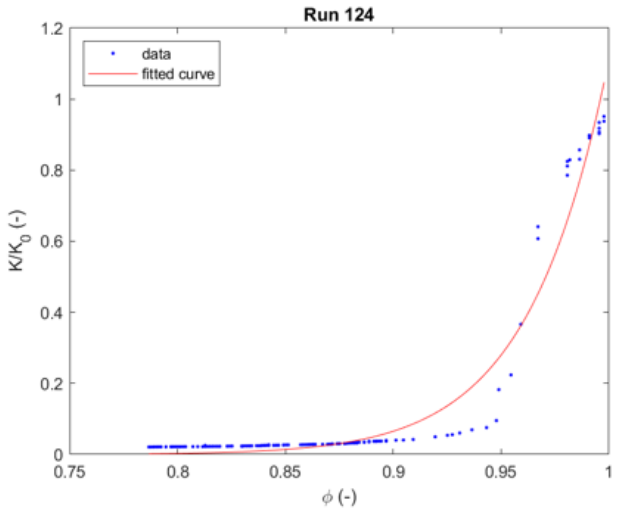
Run 124
data
fitted curve
K/K0 (-)
ϕ (-)

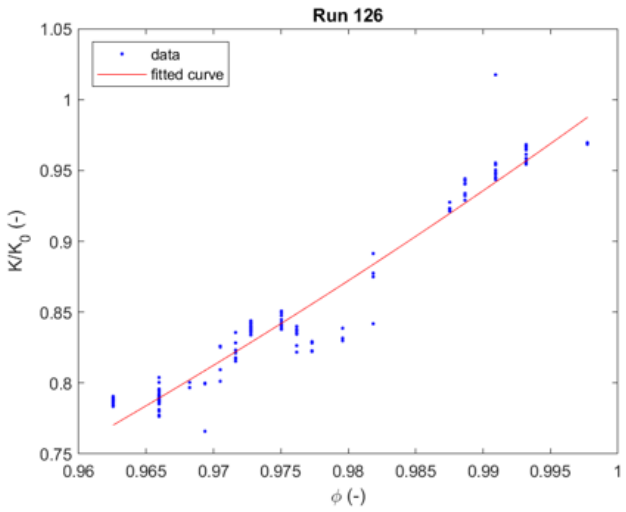
Run 126
data
fitted curve
K/K0 (-)
ϕ (-)

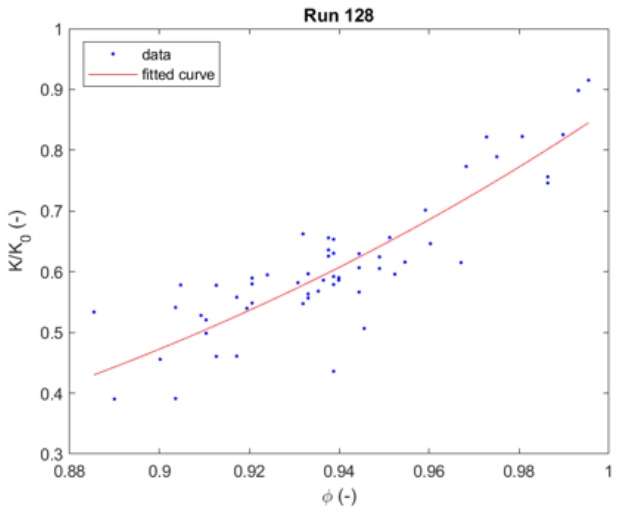
Run 128
data
fitted curve
K/K0 (-)
ϕ (-)

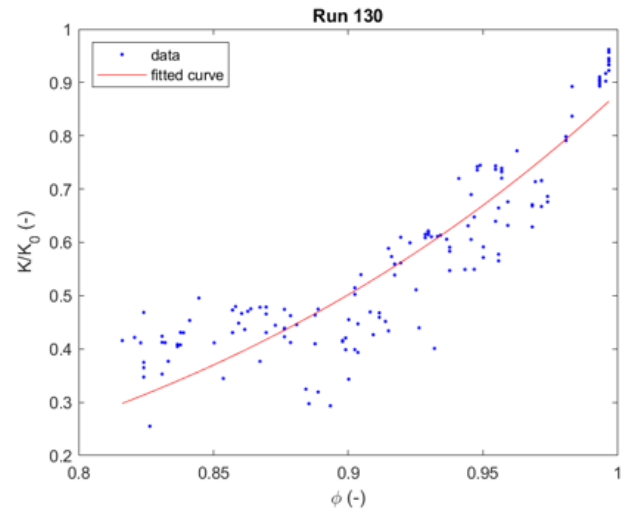
Run 130
data
fitted curve
K/K0 (-)
ϕ (-)

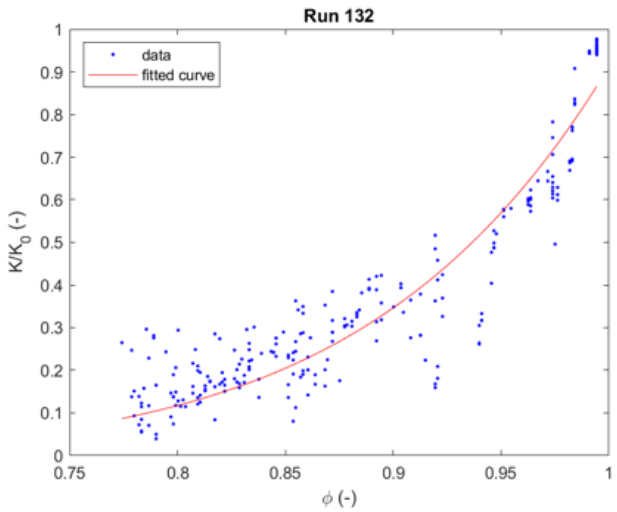
Run 132
data
fitted curve
K/K0 (-)
ϕ (-)

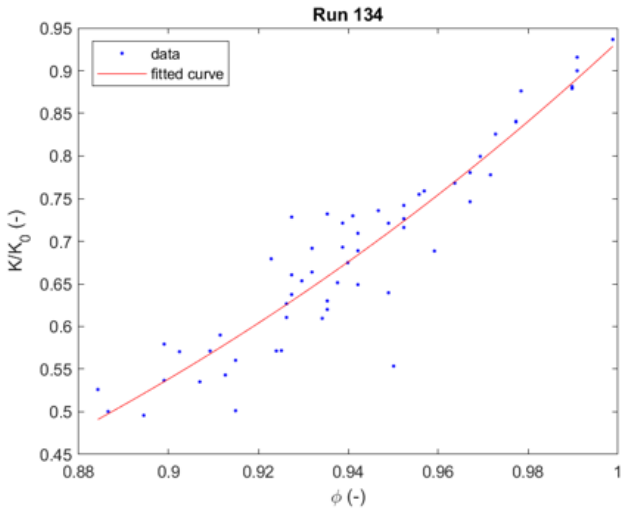
Run 134
data
fitted curve
K/K0 (-)
ϕ (-)

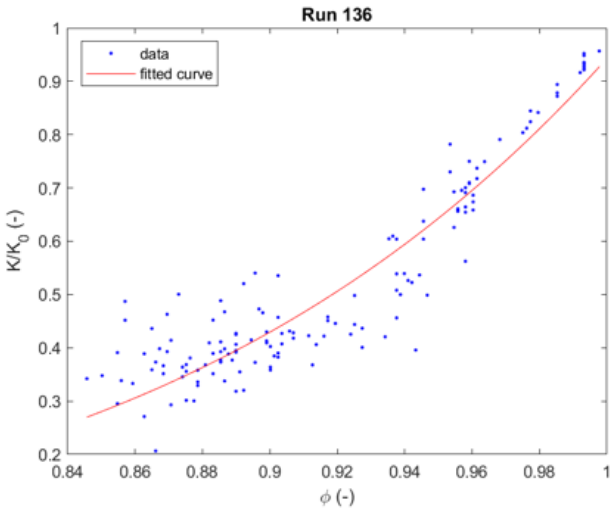
Run 136
data
fitted curve
K/K0 (-)
ϕ (-)

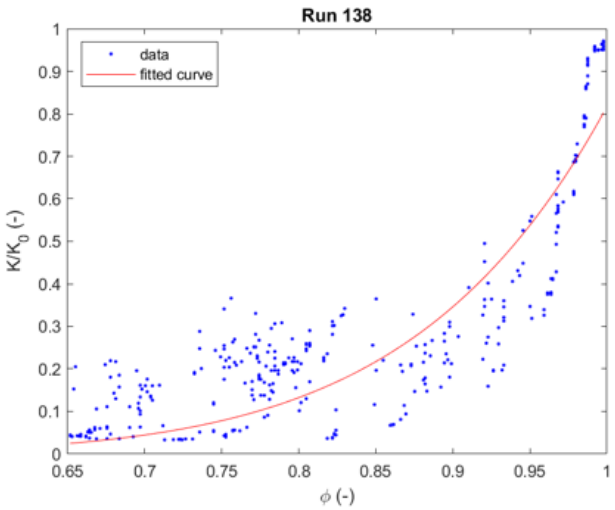
Run 138
data
fitted curve
K/K0 (-)
ϕ (-)

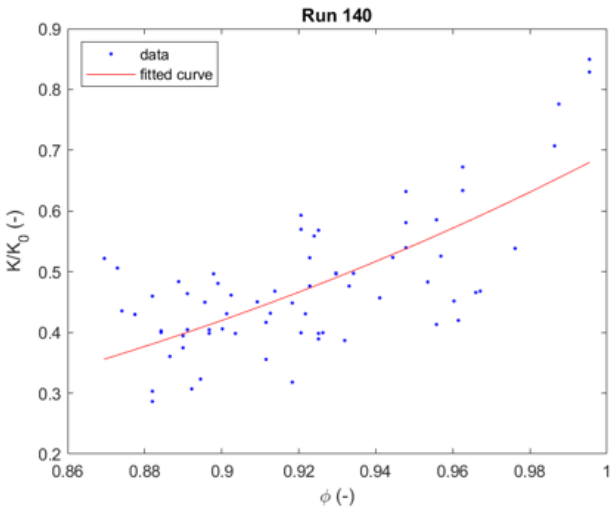
Run 140
data
fitted curve
K/K0 (-)
ϕ (-)

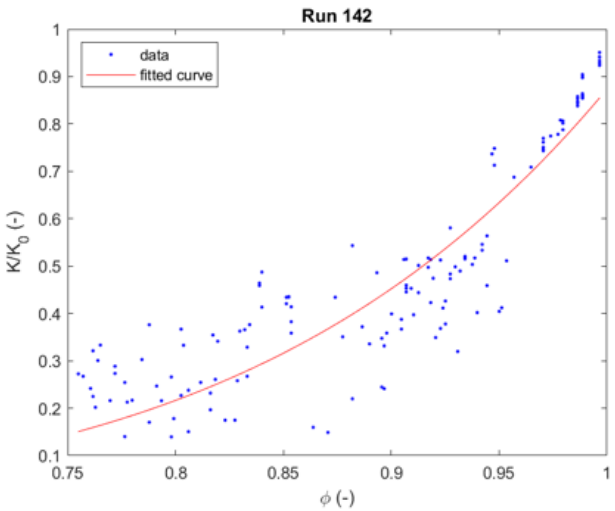
Run 142
data
fitted curve
K/K0 (-)
ϕ (-)

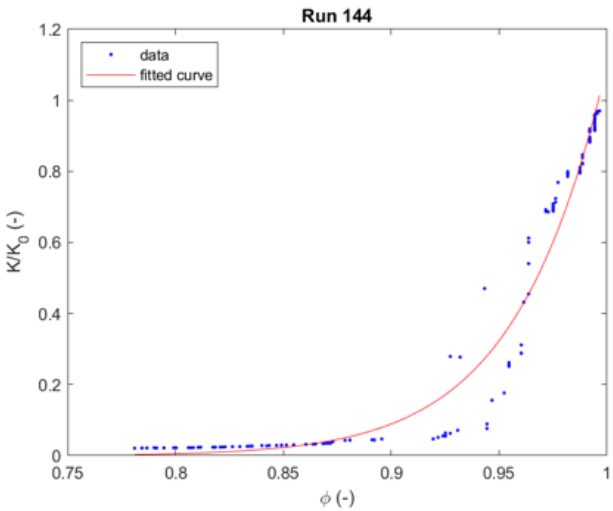
Run 144
data
fitted curve
K/K0 (-)
ϕ (-)

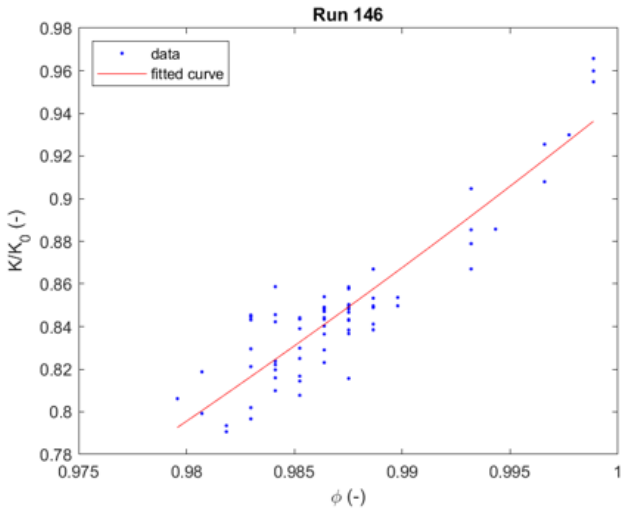
Run 146
data
fitted curve
K/K0 (-)
ϕ (-)

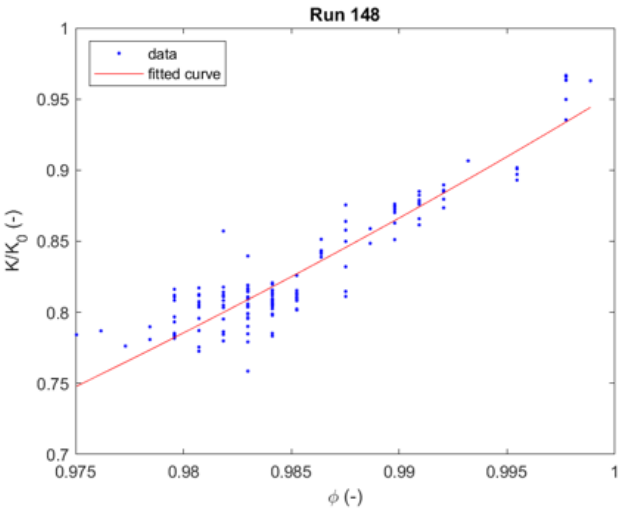
Run 148
data
fitted curve
K/K0 (-)
ϕ (-)

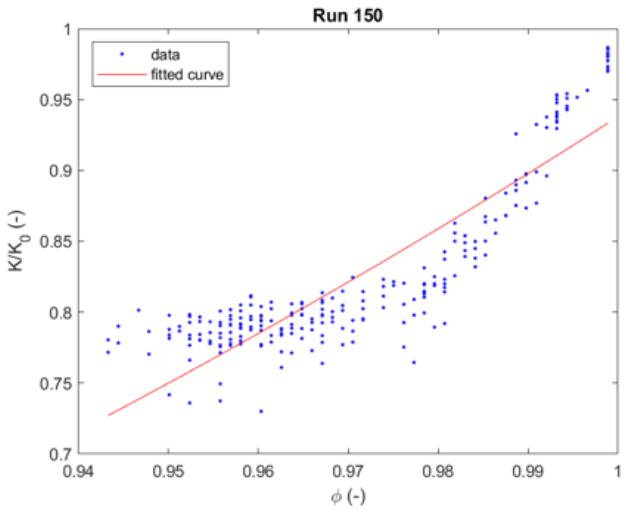
Run 150
data
fitted curve
K/K0 (-)
ϕ (-)

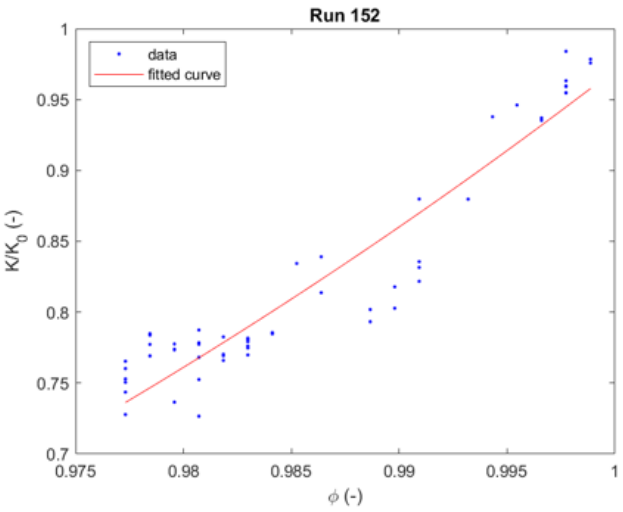
Run 152
data
fitted curve
K/K0 (-)
ϕ (-)

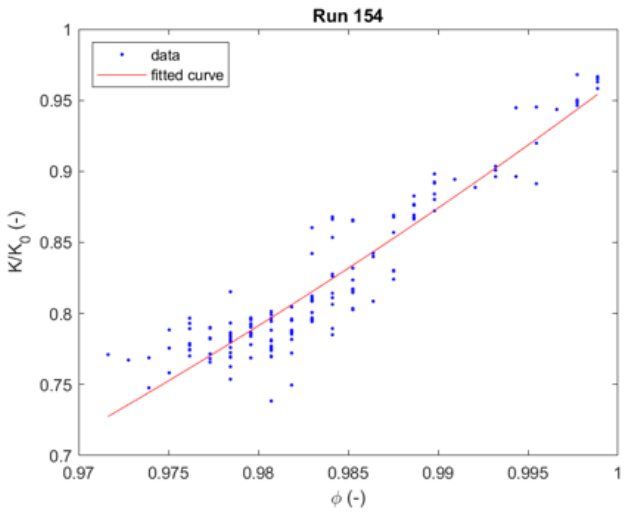
Run 154
data
fitted curve
K/K0 (-)
ϕ (-)

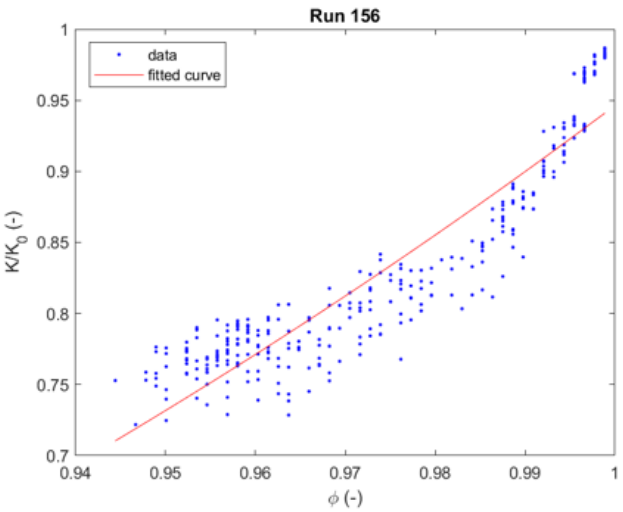
Run 156
data
fitted curve
K/K0 (-)
ϕ (-)

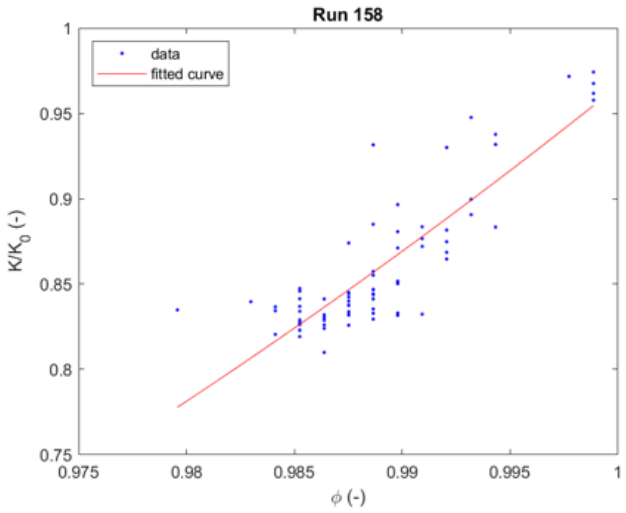
Run 158
data
fitted curve
K/K0 (-)
ϕ (-)

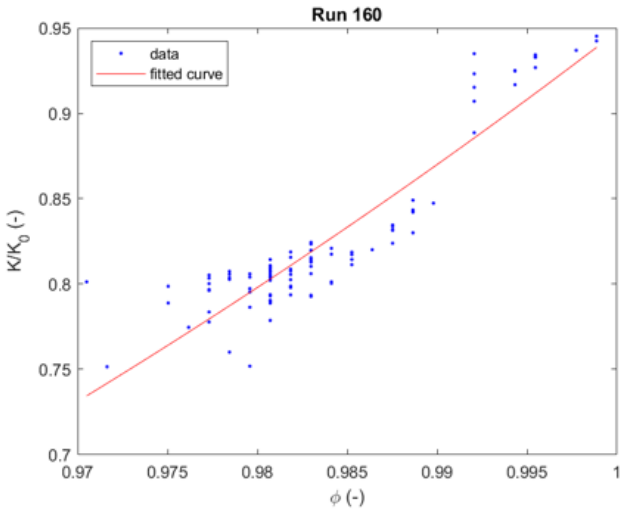
Run 160
data
fitted curve
K/K0 (-)
ϕ (-)

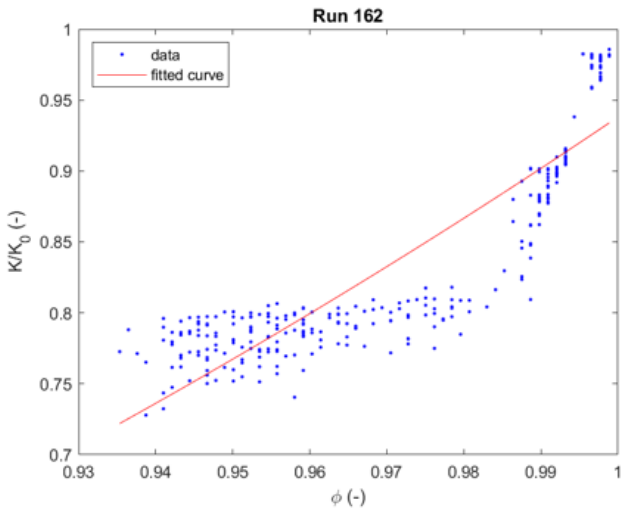
Run 162
data
fitted curve
K/K0 (-)
ϕ (-)

References

[1] Yao, K.-M., Habibian, M. T., & O'Melia, C. R. (1971). Water and Waste Water Filtration: Concepts and Applications. *Environmental Science & Technology*, *5*, 1105–1112.

[2] Tobiason, J. E., & O'Melia, C. R. (1988). Physicochemical Aspects of Particle Removal in Depth Filtration. *American Water Works Association*, *83*, 54–64.

[3] Prevo, B. G., Kuncicky, D. M., & Velev, O. D. (2007). Engineered Deposition of Coatings from Nano- and Micro-Particles: a Brief Review of Convective Assembly at High Volume Fraction. *Colloids and Surfaces*, *311*, 2–10.

[4] Bohnet, M. (1987). Fouling of Heat Transfer Surfaces. *Chemical Engineering & Technology*, *10*, 113–125.

[5] Bradford, S. A., & Torkzaban, S. (2008). Colloid Transport and Retention in Unsaturated Porous Media: A Review of Interface-, Collector-, and Pore-Scale Processes and Models. *Vadose Zone Journal*, *7*(2), 667–681. https://doi.org/10.2136/vzj2007.0092

[6] Hommel, J., Coltman, E., & Class, H. (2018). Porosity–Permeability Relations for Evolving Pore Space: A Review with a Focus on (Bio-)geochemically Altered Porous Media. *Transport in Porous Media*, *124*(2), 589–629. https://doi.org/10.1007/s11242-018-1086-2

[7] Krüger, T., Kusumaatmaja, H., Kuzmin, A., Shardt, O., Silva, G., & Viggen, E. M. (2016). *The Lattice Boltzmann Method: Principles and Practice*. Switzerland: Springer International Publishing.

[8] Mohamad, A. A. (2011). *Lattice Boltzmann Method* (1st ed.). London: Springer London.

[9] Jafari, S., Yamamoto, R., & Rahnama, M. (2011). Lattice-Boltzmann method combined with smoothed-profile method for particulate suspensions. *Physical Review E*, *83*(2). https://doi.org/10.1103/physreve.83.026702

[10] Chen, S., & Doolen, G. D. (1998). LATTICE BOLTZMANN METHOD FOR FLUID FLOWS. *Annual Review of Fluid Mechanics*, *30*(1), 329–364. https://doi.org/10.1146/annurev.fluid.30.1.329

[11] Succi, S. (2001). *The Lattice Boltzmann Equation: For Fluid Dynamics and Beyond*. Oxford: Clarendon Press.

[12] Day, M. A. (1990). The No-Slip Condition of Fluid Dynamics. *Erkenntnis*, *33*, 285–296.

[13] Bouzidi, M., Firdaouss, M., & Lallemand, P. (2001). Momentum transfer of a Boltzmann-lattice fluid with boundaries. *Physics of Fluids*, *13*(11), 3452–3459. https://doi.org/10.1063/1.1399290

[14] Zou, Q., & He, X. (1997). On pressure and velocity boundary conditions for the lattice Boltzmann BGK model. *Physics of Fluids*, *9*(6), 1591–1598. https://doi.org/10.1063/1.869307

[15] Ladd, A. J. C. (1994a). Numerical simulations of particulate suspensions via a discretized Boltzmann equation. Part 1. Theoretical foundation. *Journal of Fluid Mechanics*, *271*, 285–309. https://doi.org/10.1017/s0022112094001771

[16] Ladd, A. J. C. (1994b). Numerical simulations of particulate suspensions via a discretized Boltzmann equation. Part 2. Numerical results. *Journal of Fluid Mechanics*, *271*, 311–339. https://doi.org/10.1017/s0022112094001783

[17] Yu, Z., & Fan, L.-S. (2010). Lattice Boltzmann method for simulating particle–fluid interactions. *Particuology*, *8*(6), 539–543. https://doi.org/10.1016/j.partic.2010.07.012

[18] Nakayama, Y., Kim, K., & Yamamoto, R. (2010). Direct simulation of flowing colloidal dispersions by smoothed profile method. *Advanced Powder Technology*, *21*(2), 206–211. https://doi.org/10.1016/j.apt.2009.11.011

[19] Nakayama, Y., & Yamamoto, R. (2005). Simulation method to resolve hydrodynamic interactions in colloidal dispersions. *Physical Review E*, *71*(3). https://doi.org/10.1103/physreve.71.036707

[20] Raveendran, P., & Amirtharajah, A. (1995). Role of Short-Range Forces in Particle Detachment During Filter Backwashing. *Journal of Environmental Engineering*, *121*(12), 860–868.

[21] Butt, H. J., & Kappl, M. (2018). *Surface and Interfacial Forces*. Germany: Wiley.

[22] Hogg, R., Healy, T. W., & Fuerstenau, D. W. (1966). Mutual coagulation of colloidal dispersions. *Transactions of the Faraday Society*, *62*, 1638–1651. https://doi.org/10.1039/tf9666201638

[23] Abrikosov, A. A., GorKov, L. P., & Dzyaloshinski, I. E. (1975). *Methods of Quantum Field Theory in Statistical Physics*. United States: Dover Publications.

[24] Peng, Z., Doroodchi, E., & Evans, G. (2010). DEM simulation of aggregation of suspended nanoparticles. *Powder Technology*, *204*(1), 91–102. https://doi.org/10.1016/j.powtec.2010.07.023

[25] Chaumeil, F., & Crapper, M. (2014). Using the DEM-CFD method to predict Brownian particle deposition in a constricted tube. *Particuology*, *15*, 94–106. https://doi.org/10.1016/j.partic.2013.05.005

[26] Gregory, J. (1981). Approximate expressions for retarded van der waals interaction. *Journal of Colloid and Interface Science*, *83*(1), 138–145. https://doi.org/10.1016/0021-9797(81)90018-7

[27] Qui, Q., (2015). *Theoretical and computational study of colloid transport and retention in saturated soil porous media* (Doctoral Dissertation). Retrieved from

http://dspace.udel.edu/bitstream/handle/19716/17595/2015_QiuQueming_PhD.pdf?sequence=1&isAllowed=y

[28] Le Gallo, Y., Bildstein, O., & Brosse, E. (1998). Coupled reaction-flow modeling of diagenetic changes in reservoir permeability, porosity and mineral compositions. *Journal of Hydrology*, *209*(1–4), 366–388. https://doi.org/10.1016/s0022-1694(98)00183-8

[29] Rodgers, D. P. (1985). Improvements in multiprocessor system design. *ACM SIGARCH Computer Architecture News*, *13*(3), 225–231. https://doi.org/10.1145/327070.327215

[30] He, X., & Luo, L.-S. (1997). Theory of the lattice Boltzmann method: From Boltzmann equation to the lattice Boltzmann equation. *Physical Review E*, *56*(6), 6811–6817.

[31] Bergendahl, J., & Grasso, D. (1999). Prediction of Colloid Detachment in a Model Porous Media: Thermodynamics. *AIChE Journal*, *45*(3), 475–484.

[32] Bergström, L. (1997). Hamaker constants of inorganic materials. *Advances in Colloid and Interface Science*, *70*, 125–169.

[33] NAGASAKI, S., TANAKA, S., & SUZUKI, A. (1993). Fast Transport of Colloidal Particles through Quartz-Packed Columns. *Journal of Nuclear Science and Technology*, *30*(11), 1136–1144. https://doi.org/10.1080/18811248.1993.9734599

[34] Greenwood, R., & Kendall, K. (1999). Selection of Suitable Dispersants for Aqueous Suspensions of Zirconia and Titania Powders using Acoustophoresis. *Journal of the European Ceramic Society*, *19*(4), 479–488. https://doi.org/10.1016/s0955-2219(98)00208-8